Year : 2019

Three-dimensional thermo-mechanical numerical modelling of fold and thrust nappe stacking with application to the Helvetic nappe system (W Switzerland)

Spitz Richard

Spitz Richard, 2019, Three-dimensional thermo-mechanical numerical modelling of fold and thrust nappe stacking with application to the Helvetic nappe system (W Switzerland)

Originally published at : Thesis, University of Lausanne

Posted at the University of Lausanne Open Archive http://serval.unil.ch
Document URN : urn:nbn:ch:serval-BIB_79EB912CE4921

UNIL | Université de Lausanne
Institut des sciences de la Terre

Faculté des géosciences et de l'environnement

Institut des sciences de la Terre

Three-dimensional thermo-mechanical numerical modelling of fold and thrust nappe stacking with application to the Helvetic nappe system (W Switzerland)

Thèse de doctorat

présentée à la Faculté des géosciences et de l'environnement de l'Université de Lausanne

pour l'obtention du grade de Docteur en sciences de la Terre par

Richard Spitz

Msc, Johannes-Gutenberg University Mainz

Jury

Prof. Dr. Frédéric Herman	Université de Lausanne	Président du jury
Prof. Dr. Stefan M. Schmalholz	Université de Lausanne	Directeur de thèse
Prof. Dr. Yury Y. Podladchikov	Université de Lausanne	Expert interne
Prof. Dr. Jean-Luc Epard	Université de Lausanne	Expert interne
Prof. Dr. Philippe Yamato	Université de Rennes	Expert externe

Lausanne, 2019

UNIL | Université de Lausanne
Faculté des géosciences et de l'environnement
bâtiment Géopolis bureau 4631

IMPRIMATUR

Vu le rapport présenté par le jury d'examen, composé de

Président de la séance publique :	M. le Professeur Frédéric Herman
Président du colloque :	M. le Professeur Frédéric Herman
Directeur de thèse :	M. le Professeur Stefan Schmalholz
Expert interne :	M. le Professeur Yury Podladchikov
Expert interne :	M. le Professeur Jean-Luc Epard
Expert externe :	M. le Professeur Philippe Yamato

Le Doyen de la Faculté des géosciences et de l'environnement autorise l'impression de la thèse de

Monsieur Richard SPITZ

Titulaire d'un
Master en sciences de la Terre
De l'Université Johannes Gutenberg

intitulée

Three-dimensional thermo-mechanical numerical modelling of fold and thrust nappe stacking with application to the Helvetic nappe system (W Switzerland)

Lausanne, le 3 décembre 2019

Pour le Doyen de la Faculté des géosciences et de l'environnement

Professeur Frédéric Herman

Contents

Abstract

Fold and thrust belts are a common structural feature of orogens that form in response to compressional tectonics. They have been studied by geologists for at least a century with the aim to understand the structural style, tectonic evolution, dynamics and the control factors that govern their formation. Classically, we consider two distinctive large scale tectonic styles for a fold and thrust belt, namely thick-skinned and thin-skinned tectonic style. These styles are derived from the degree of basement-cover interaction during the fold and thrust belt formation. The former implies that the crystalline basement and overlying sedimentary cover-sequences accommodate an equal amount of deformation during crustal shortening. In contrast a thin-skinned style implies that most of the bulk shortening is accommodated in the deformation of sedimentary cover-sequences above the basement along a weak basal shear or detachment zone. Therefore, the basement remains mostly undeformed while the cover-sequences exhibit significant internal deformation and/or horizontal displacement. The structural style of fold and thrust belts is closely linked to inherited crustal structures, such as basins or variations in the lithostratigraphy. Hence, large amount of data on fold and thrust belts indicates that the structural style can be highly variable for the same belt. For example, studies report changes in style from the exterior of the belt to the interior or from one end to the other along-strike. Consequently, it is suggestible that the three-dimensional geometry of inherited pre-orogenic structures presents a prevailing control factor on the structural style of fold and thrust belts.

In this thesis we focus on one of the preeminent fold and thrust belts belonging to the Western Swiss Alps, namely the Helvetic nappe system. The Helvetic nappe system has a long standing history in Alpine geology and was one of the major testing grounds for the evolution of the so-called nappe theory. In general, a tectonic nappe is defined as a coherent allochthonous rock unit/sheet that has been displaced away from its original position along a basal thrust or shear zone. Furthermore we distinguish between two end-member types, namely fold nappes and thrust nappes. Fold nappes are large recumbent folds with an amplitude of several kilometers contributing to a stratigraphic inversion of the same magnitude. In contrast thrust nappes are emplaced as coherent rock sheets along a basal thrust resulting in the superposition of stratigraphic older units on top of younger units. The Helvetic nappe system exhibits transition between these two the different nappe styles along-strike. The style changes form the famous Morcles fold nappe in the Southwest, to the Doldenhorn fold nappe in the center and the prominent Glarus thrust nappe in the Northeast. Morever, both the Morcles and Doldenhorn nappe are overlain by series of smaller thrusts sheets that are analogues to the Glarus nappe. Interestingly, the Doldenhorn fold nappe shows a less pronunced recumbent limb and internal

folding than the Morcles nappe, whereas the Doldenhorn nappe shows greater shearing. Both of these nappes are derived from sediments that were once situated in a graben system that was inverted during the Alpine orogeny. Contrary reconstructions of the Glarus nappe do not point to a pronounced graben system. Hence it is suggested that lateral variations in the basement structure had a major influence on the evolution of the Helvetic nappe systems.

The aim of this thesis is to gain additional insights in the lateral transition between folding and thrusting and the evolution and emplacement of fold and thrust nappe stacking in three-dimensional space. To this aim we employ three-dimensional (3D) thermo-mechanical numerical models that we apply to the Helvetic nappe system. In our first study (Chapter 2) we implement a numerical algorithm to calculate and trace 3D finite strain in order to quantify the deformation. We further use a simple 3D viscous model consisting of a laterally changing mechanical stratigraphy (lithostratigraphy) to simulate the transition between thrusting and folding. Our results essentially show that the spatial distribution and gradient of mechanical stratigraphy is directly expressed in a change of the finite strain gradient along the hinge of the fold to the thrust sheet. In our second study (Chapter 3) we employ a 3D numerical model of a simplified passive margin with an inherited graben structure to simulate the formation of a fold nappe that is over-thrusted by a thrust sheet. Furthermore, the model parameters and configuration are adapted to mimic the initial conditions of the Helvetic nappe systems. We are able to reproduce several first order key features such as the nappe structure, temperature distribution, geologic timing and finite strain pattern. Continuing, we show that a relative simple graben systems can explain changes in fold nappe structure along-strike. Additionally our model results imply that large thrust sheets may propagate in horizontal direction without disturbance by underlying fold nappe formation. Finally our models also indicate that thrust and fold nappe formation in the Helvetic nappe systems likely occurred under a semi-brittle-ductile deformation regime.

Résumé

Les chaînes de montagnes constituées de plis et de chevauchement sont une caractéristique structurale commune des orogènes qui se forment en réponse à la tectonique de compression. Elles ont été étudiés par des géologues pendant au moins un siècle dans le but de comprendre leur style structural, leur évolution tectonique, leur dynamique et les facteurs de contrôle qui régissent leur formation. Classiquement, nous considérons deux styles tectoniques distincts à grande échelle, pour une courroie pliante et une courroie de poussée, à savoir le style tectonique à thick skinned et à thin skinned. Ces styles sont dérivés du degré d'interaction substratum au socle - couverture pendant la formation de la chaîne de montagne. La première implique que le socle cristallin et les séquences de couverture sédimentaire sus-jacentes permettent une quantité égale de déformation pendant le raccourcissement de la croûte terrestre. Par contre, un style à thin skinned implique que la plus grande partie du raccourcissement est accommodée dans la déformation des séquences de couverture sédimentaires au-dessus du socle le long d'une zone faible de cisaillement ou de décollement de la base. Par conséquent, le socle demeure en grande partie non déformé, tandis que les séquences de couverture présentent des déformations internes et/ou des déplacements horizontaux importants. Le style structural de plis et de chevauchement est étroitement lié aux structures crustales héritées du passé, telles que les bassins ou les variations de la mechanical stratigraphy. Par conséquent, une grande quantité de données sur les plis et de chevauchement indique que le style tectonique mais aussi le style interne peuvent être très variables pour une même chaîne. Par exemple, des études font état de changements de style de l'extérieur de la ceinture à l'intérieur ou d'un bout à l'autre de la ceinture. Par conséquent, il est permis de penser que la géométrie tridimensionnelle des structures pré-orogéniques héritées présente un facteur de contrôle dominant sur le style structural des chaînes de montagnes.

Dans cette thèse, nous nous concentrons sur l'une des principales chaînes de montagnes des Alpes romandes, à savoir le système de nappe helvétique. Le système de nappe helvétique a une longue histoire en géologie alpine et a été l'un des principaux terrains d'essai pour l'évolution de la théorie dite des nappes. En général, une nappe tectonique est définie comme une unité de roche allochtone cohérente qui s'est éloignée de sa position initiale le long d'une zone de chevauchement ou de cisaillement. En outre, nous distinguons deux types de cas extrême, à savoir les nappes plissés et les nappes chevauchements. Les nappes plissées sont de grands plis couchés d'une amplitude de plusieurs kilomètres contribuant à une inversion stratigraphique de même amplitude. En revanche, les nappes chevauchements sont placées sous forme de nappes rocheuses cohérentes le long d'un chevauchement basal, ce qui entraîne la superposition d'unités stratigraphiques plus anciennes sur

des unités plus jeunes. Le système de nappe helvétique présente une transition entre ces deux styles de nappe différents. Les changements de style forment la fameuse nappe de plis de Morcles au sud-ouest, la nappe de plis du Doldenhorn au centre et la nappe de poussée de Glaris au nord-est. De plus, la nappe de Morcles et la nappe du Doldenhorn sont recouvertes d'une série d'unites de poussée plus petites qui sont analogues à la nappe de Glaris. Il est intéressant de noter que la nappe du Doldenhorn présente un plissement interne et un plissement des membres couchés moins prononcés que la nappe des Morcles, tandis que la nappe du Doldenhorn présente un cisaillement plus important. Ces deux nappes sont dérivées de sédiments qui étaient autrefois situés dans un système de graben inversé pendant l'orogenèse alpine. Contrairement aux reconstitutions de la nappe de Glaris, il n'y a pas de système de graben prononcé. Il est donc suggéré que les variations latérales de la structure du socle e ont eu une influence majeure sur l'évolution des systèmes de nappe helvétique.

Le but de cette thèse est d'acquérir des connaissances supplémentaires sur la transition latérale entre la plissement et la chevauchement et sur l'évolution et l'emplacement de l'empilement des nappes dans un espace tridimensionnel. Pour ce faire, nous utilisons des modèles numériques tridimensionnels (3D) thermo-mécaniques que nous appliquons au système de nappe helvétique. Dans notre première étude (chapitre 2), nous mettons en œvre un algorithme numérique pour calculer et tracer les déformations 3D finies afin d'en quantifier la déformation. Nous utilisons en outre un modèle visqueux 3D simple constitué d'une mechanical stratigraphy à changement latéral pour simuler la transition entre la plissement et chevauchment. Nos résultats montrent essentiellement que la distribution spatiale et le gradient de la stratigraphie s'expriment directement par un changement du gradient de déformation fini le long de la charnière du pli. Dans notre deuxième étude (chapitre 3), nous utilisons un modèle numérique 3D d'une marge passive simplifiée avec une structure de graben hérité pour simuler la formation d'une nappe de plis qui est surchargée par une nappe de chevauchment. De plus, les paramètres et la configuration du modèle sont adaptés pour imiter les conditions initiales des systèmes de nappe helvétique. Nous sommes en mesure de reproduire plusieurs caractéristiques clés de premier ordre telles que la structure de la nappe, la distribution de la température, la chronologie des événements et le profil de déformation fini. À partir de là, nous montrons qu'un système de graben relativement simple peut expliquer les changements dans la structure de la nappe plissée tout au long de chaîne. De plus, nos modèles déduisent que les grandes nappes de chevauchement peuvent avancer presque sans être perturbées horizontalement. Enfin, nos modèles indiquent également que la formation de nappes de poussée et de plis dans les systèmes de nappes helvétiques s'est probablement produite sous un régime de déformation semi-fragile-ductile.

Résumé grand public

Dans cette thèse, nous nous concentrons sur l'une des principales ceintures de nappes de plis et de chevauchement des Alpes de Suisse romande, à savoir le système des nappes helvétiques. Le système des nappes helvétiques a une longue histoire dans la géologie alpine et a été l'un des principaux terrains d'essai pour l'évolution de la théorie des nappes. En général, une nappe tectonique est définie comme une unité de roche allochtone cohérente qui s'est éloignée de sa position initiale le long d'un chevauchement basal ou d'une zone de cisaillement. De plus, nous distinguons deux types de nappes, à savoir les nappes de plis et les nappes de charriage. Les nappes de plis sont des grands plis couchés d'une amplitude de plusieurs kilomètres contribuant à une inversion stratigraphique de même amplitude. En revanche, les nappes de chevauchment sont mises en place le long d'un chevauchement basal sous forme de nappes cohérentes, ce qui entraîne la superposition d'unités stratigraphiques plus anciennes sur des unités plus jeunes. Le système des nappes helvétiques présente une transition entre ces deux styles de formation de nappes. Les changements de style forment la fameuse nappe plissée de Morcles au sud-ouest, la nappe plissée du Doldenhorn au centre et la nappe de chevauchment de Glaris au nord-est. De plus, la nappe de Morcles et la nappe du Doldenhorn sont recouvertes d'une série de nappes chevauchantes plus petites qui sont analogues à la nappe de Glaris. Il est intéressant de noter que la nappe du Doldenhorn présente un flanc couché moins prononcés que la nappe de Morcles. Les reconstitutions montrent que ce changement est probablement dû aux variations de la structure initiale du graben qui contenait autrefois les unités rocheuses des deux nappes. Contrairement aux reconstitutions de la nappe de Glaris, il n'y a pas de système de graben prononcé. Il est donc suggéré que les variations latérales de la structure du socle ont eu une influence majeure sur l'évolution du système des nappes helvétiques.

Le but de cette thèse est d'acquérir des connaissances supplémentaires sur la transition latérale entre le plissement et le chevaugement et sur l'évolution et l'emplacement de l'empilement des nappes de plissement et de charriage dans un espace tridimensionnel. Pour ce faire, nous utilisons des modèles numériques thermo-mécaniques en trois dimensions (3D) que nous appliquons au système des nappes helvétiques. Dans notre première étude, nous mettons en œuvre un algorithme numérique pour calculer et tracer les déformations finies en 3D afin d'en quantifier la déformation. Nous utilisons en plus un modèle visqueux 3D simple constitué d'une stratigraphie qui varie latéralement pour simuler la transition entre un chevauchement et un plissement. Nos résultats montrent essentiellement que la distribution spatiale et le gradient de la mechanical stratigraphy s'expriment directement par un changement du gradient de déformation finie le long de la charnière du pli vers la nappe chevauchment. Dans notre deuxième étude, nous utilisons un modèle numérique 3D d'une marge passive

simplifiée avec une structure de graben hérité pour simuler la formation d'une nappe de plis qui est surmontée par une nappe de charriage. De plus, les paramètres et la configuration du modèle sont adaptés pour imiter les conditions initiales du système des nappes helvétiques. Nous sommes en mesure de reproduire plusieurs caractéristiques clés de premier ordre telles que la structure de la nappe, la distribution de la température, la chronologie des événements et le profil de déformation finie. À partir de là, nous montrons qu'un système de graben relativement simple peut expliquer les changements dans la structure de la nappe plissée tout au long du profil. Enfin, nous acquérons également des connaissances supplémentaires sur le régime de déformation lors de la formation du système des nappes helvétiques.

CHAPTER 1

Introduction

The body of this thesis consists of four main parts. The first part provides a general overview of fold and thrust belts, followed by an overview of tectonic nappes and the Helvetic nappe system to which we apply our numerical algorithm. Further, we describe our continuum mechanics and numerical code used to solve our numerical problems. This introduction is followed by two three-dimensional (3D) numerical studies that investigate (i) 3D finite strain computation with application to the transition between viscous overthrusting and folding, and (ii) the impact of 3D inherited half-graben architecture on nappe stacke formation with application to the Helvetic nappe system. Next, Chapter 4 will provide a short summary of our results with a concluding outlook. Finally, Chapter 5 (Appendix) includes two Matlab scripts exemplifying finite strain calculation and a performance benchmark of our algorithm.

Definitions

Detachment horizon Here interchangeable with the term décollement (plane), meaning a surface along which overlying rocks have moved in the course of deformation.

Mechanical stratigraphy In the context of the thesis the mechanical stratigraphy refers to, as for example defined by Pfiffner (1993), to the thickness contrast between different stratigraphic units of different mechanical strength. In general this term also includes the effect of mechanical discontinuities, such as, for example, generated by normal faults on the deformational behavior of rock strata.

Nappe From the French word nappe, meaning 'cover', a thrusted coherent rock mass or folded body of up to several km length and thickness that has been displaced from its original substratum.

1.1 Fold and thrust belts

1.1.1 Overview

Fold and thrust belts are an universal structural feature of orogens on Earth which can be observed throughout most geological eras (Figure 1.1; worldwide orogenies through time taken form Liou et al., 2009). Unsurprisingly, they are therefore an active area for geological studies, also largely due to hydrocarbon exploration (e.g. Dunn et al., 1995; Cooper, 2007; Lacombe et al., 2007). Typically, fold and thrust belts are located in the foreland of an orogen and are commonly comprised of deformed sedimentary sequences. In some cases, however, they also show the involvement of crystalline basement rocks. They are formed during compressional tectonics and hence occur in various geological settings such as continental plate collisions, subduction zones (Figure 1.2), intraplate locations or also along oblique plate

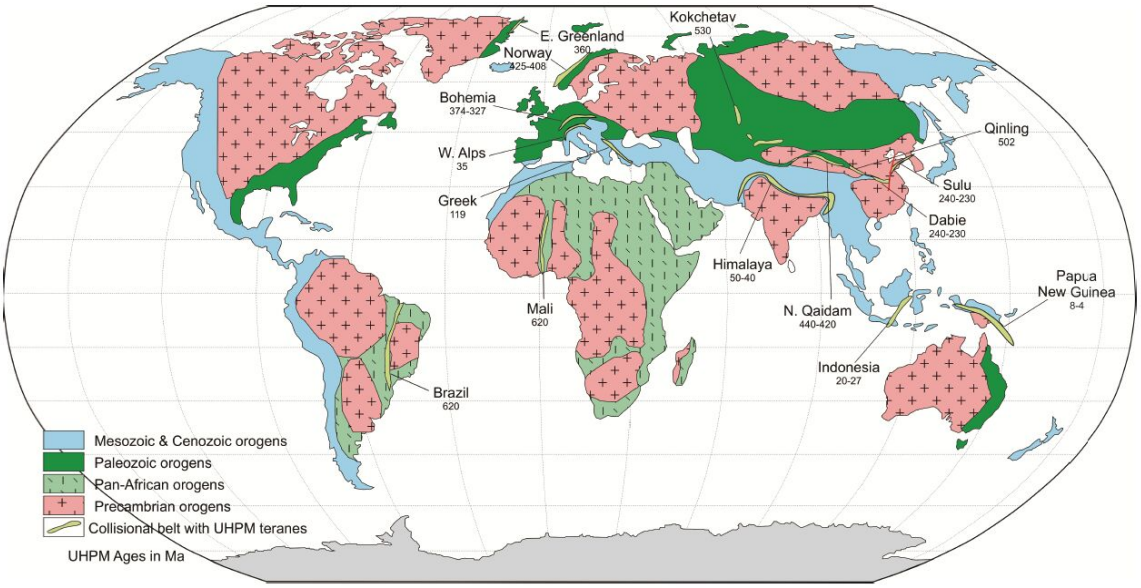

Figure 1.1: World map displaying the distribution of orogens by geological era (taken from Liou et al., 2009).

boundaries that involve transpression (e.g. Poblet and Lisle, 2011). They are structurally complex and can exhibit an array of different structures, such as forward and back thrusts, folds, nappes or duplexes (e.g. Price and McClay, 1981). For centuries, geologists have spent considerable efforts to understand their origin, geometry, structural and geodynamic evolution, as well as the control parameters that govern their formation. These parameters include, to name a few, inherited structures, mechanical stratigraphy, geodynamic setting or the thermal structure of the lithosphere. The vast interest in fold and thrust belts is reflected in a large body of monographs starting from the 1970s (e.g. Price and McClay, 1981; McClay, 1992; Macqueen and Leckie, 1992; Mitra and Fisher, 1992; Nemcok et al., 2009). Indeed, the early 1970s marked a breakthrough in the understanding of fold and thrust belts culminating in fundamental geological knowledge. There are numerous factors that contributed to this jump in knowledge. From the viewpoint of structural geology the three most notable milestones in this decade were, the application of classical methods of rock deformation analysis to fold and thrust belts (e.g. Ramsay, 1967; Durney et al., 1973; Fry, 1979). Here, detailed strain analysis brought a greater understanding of the small scale processes and mechanisms that contribute to the development of folds and thrust faults. Secondly, the technique of cross-sectional balancing that aided in the restoration of fold and thrust belts cross-sections to its original state as described in Dahlstrom's seminal paper on the Alberta Foothills of the Canadian Rocky Mountains (Dahlstrom, 1969). Here, the further development of additional techniques (e.g. Suppe, 1983; Suppe, 1985; Hossack, 1979; Mitra and Namson, 1989) aided in the quantification of the relationship between thrusts and folds. Altogether these innovations provided a framework of common structural geometries that could be used to reconstruct the

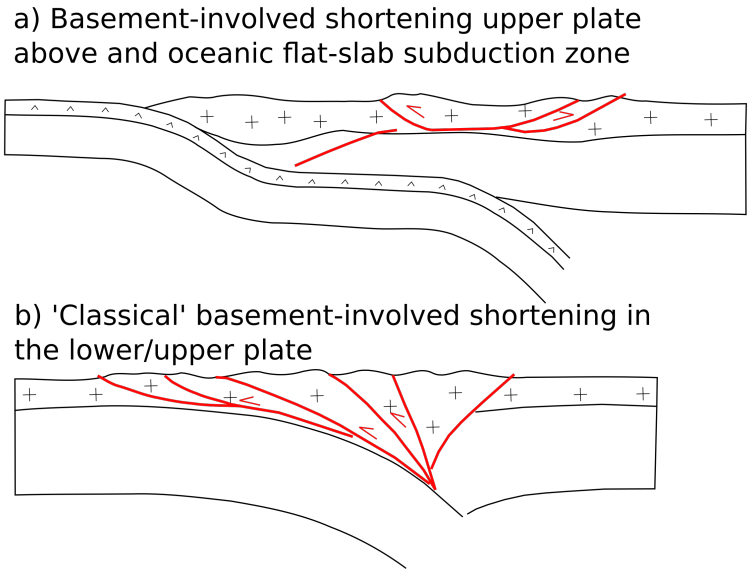

Figure 1.2: Sketch of two common subduction regimes resulting in orogeny and fold and thrust belt formation (modified after Lacombe and Bellahsen, 2016).

evolution of fold and thrust belts. Hence, the application of these techniques ranges from single geological units to entire fold and thrust belts. Consequently, the technique of kinematic and geometrical restoration is still widely in utilized and remains a fundamental method which is, for example, also used in the interpretation of seismic cross-sections. Finally, the last big milestone was the introduction of the Coloumb wedge theory (Davis et al., 1983; Dahlen et al., 1984) which was the result of extensive mechanical studies of accretionary wedges. This theory combined for the first time the interaction of gravity-force and surface-force driven motions to explain the mechanical and structural evolution of accretionary wedges. Extension of the theory to fold and thrust belts, that usually also exhibit a wedge-like shape in cross-sectional view (Figure 1.4a), marked a major step in the understanding of the large scale kinematics and dynamics of fold and thrust belts. According to this model the formation of a accretionary wedge can be understood akin to a bulldozer pushing a pile of snow (Figure 1.4b). The wedge thereby deforms until it reaches its so-called critical taper value form whereon it will slide along a basal detachment horizon (e.g. Davis et al., 1983; Dahlen et al., 1984; Buiter, 2012). If further material is added to the wedge, it will continue to deform until it reaches its new critical taper value and then repeat the process of sliding. In general, the theory is useful to describe the average state of a fold and thrust belt. However, it is limited by several assumptions like, for example, use of homogeneous brittle material, a cohesionless basal horizon and constant material properties through time (e.g. Davis et al., 1983).

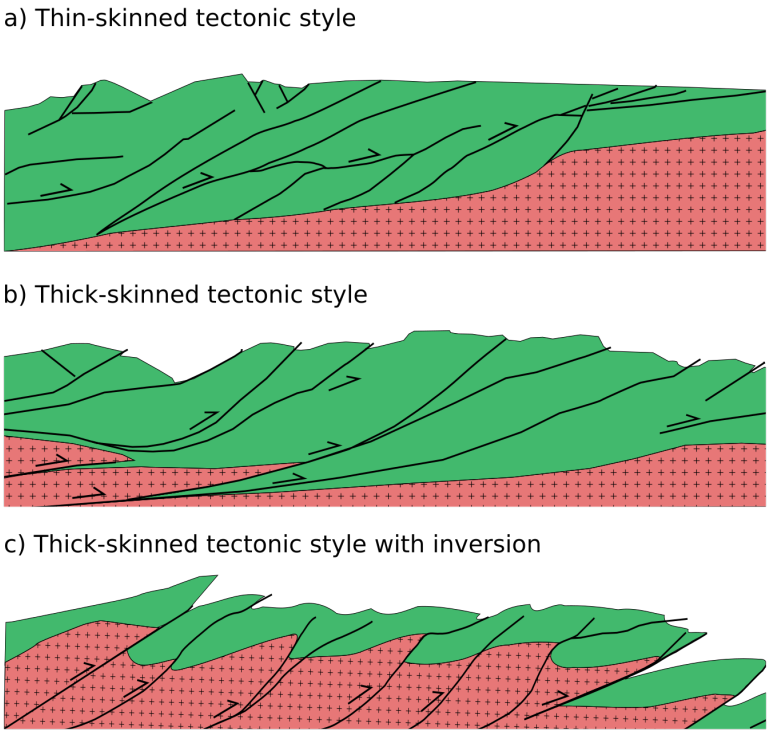

Figure 1.3: Schematic cross-sections showing the basic structural styles of fold and thrust belts: a) thin-skinned tectonic style (simplified after Mazzotti et al., 2000), b) thick-skinned tectonic style (simplified after Mirabella et al., 2008) and c) thick-skinned tectonic style with inversion (simplified after Tavarnelli et al., 2004).

1.1.2 Structural style: Thin skinned vs thick skinned

Even though fold and thrust belts usually display a wedge like geometry it is difficult to define universal features that can be attributed to all such belts (e.g. Fitz Diaz et al., 2011). The main reason therefore lies in the great multitude of parameters that influence the formation of fold and thrust belts. In consequence, they show a wide range of unique structural styles. Here, important factors that exert a strong control on the evolution are, for example, the plate tectonic setting, the interaction between sedimentary cover sequences and the underlying basement, the mechanical stratigraphy, the rheology of different rock types and the thermal structure. In addition, these control factors may have a complex interplay with each other or may vary spatially inside the same fold and thrust belt. Hence, no single cross-sectional view can provide a complete picture of a singular fold and thrust belt, even less so when looking at the entirety of fold and thrust belts (e.g. Watts et al., 1995; Allmendinger et al., 1997; Mouthereau et al., 2002; Hamilton, 1988; Nemčok et al., 2013). Nevertheless, geologists distinguish two main tectonic styles of fold and thrust belts. The two styles are derived from the interaction between the crystalline basement and the overlying cover sequences (e.g. Coward, 1983; Pfiffner, 2006; Molinaro et al., 2005) and were first described by Rodgers

(1949). The first style is called thin-skinned style and implies that the bulk deformation is constrained to the upper crustal part which comprises sedimentary cover sequences. In this case, the cover is decoupled from the underlying basement by a sole basal detachment or thrust. Consequently, internal thrusts and faults of the sedimentary cover can propagate to the

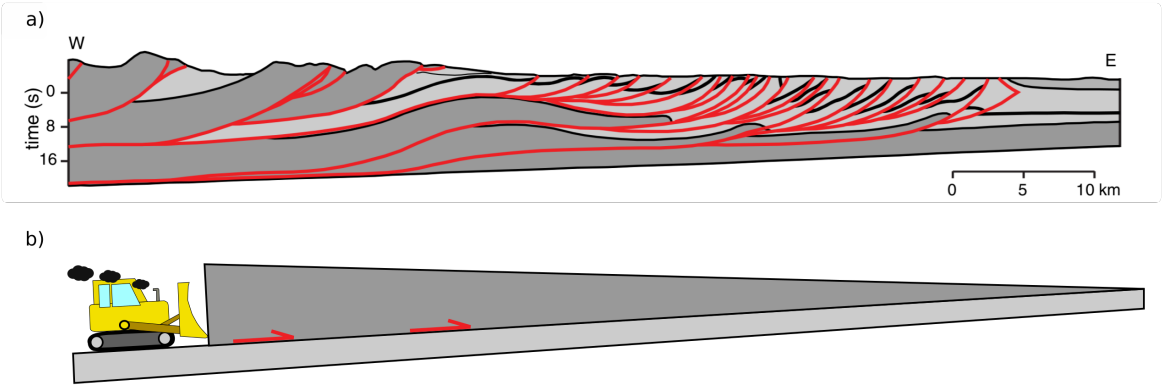

Figure 1.4: a) Cross-section through the Canadian Rocky Mountains, example of a classical thin-skinned fold and thrust belt, taken from Buiter, 2012, after Bally et al., 1966 ;b) illustration of a bulldozer pushing a wedge as analogy to the Coloumb wedge theory.

surface, but are at depth confined by this major basal detachment or thrust. Henceforth, most of the bulk shortening induced by the compressional tectonics is accommodated in sedimentary cover sequences (Figure 1.3a). Such thin-skinned behavior is, for example, observed in the Canadian Rocky Mountains (e.g. Price and McClay, 1981) or the Jura Mountains of the Swiss Alps (e.g. Burkhard and Sommaruga, 1998). Often a thin-skinned style is succeeded by a so-called thick-skinned style the closer we trace the fold and thrust belt to the core of the orogen. The term thick-skinned indicates that the crust at large, including the crystalline basement, is involved in the deformation. That is to say, parts of the basement can be incorporated into thrusts sheets (Figure 1.3b), for example, by deep rooted normal faults or the inversion of inherited basement structures such as basins and grabens (Figure 1.3c). In consequence, the structural style of thick skinned belts is subject to the degree of reactivation of pre-existing faults. Here, normal fault reactivation is mainly controlled by their angle and orientation in relation to the compressional direction (e.g. Butler, 1989; Tricart and Lemoine, 1986; Coward et al., 1991; Bellahsen et al., 2012). Moreover, the analysis of many Alpine style thick-skinned fold and thrust belts indicates that inherited structures of rifted passive margins exert a strong control on the overall deformation behavior and structure (e.g. Jackson, 1980; Lacombe and Mouthereau, 2002; Butler et al., 2006; Coward et al., 1991; Boutoux et al., 2014). However, given the fact that the tectonic style can vary inside the same fold and thrust belt, it is often difficult to apply these puristic definitions. Therefore, several authors have tried to refine the description of the tectonic styles by introducing new definitions. Pfiffner (2006), for example, proposed to apply the term thick-skinned tectonics only to belts where the complete crust is

involved in the deformation, whereas Poblet and Lisle (2011), suggest that fold and thrust belt are by definition thin-skinned. Consequently, they employ the term basement-involved belts with a thick skinned structural style as an alternative to the term thick-skinned. Furthermore, Lacombe and Bellahsen (2016) state in a recent review that progressively more evidence points to basement involved deformation inside belts that were once believed to be purely of thin-skinned style. In consequence, they refer to all belts as thick-skinned.

1.1.3 Important parameters in the Alps

Given the wide range of parameters contributing to the structural evolution of fold and thrust belts around the world, an extensive compilation is outside the scope of this thesis. For a thorough review I would therefore like to point the interested reader to a recent review of Cenozoic orogens by Lacombe and Bellahsen (2016). Nevertheless, there are some important factors that can be mentioned to provide some additional background information for the studies presented in Chapter 2 and Chapter 3. Both numerical studies were conducted with the aim to apply their results to observations made in the Helvetic nappe system of the Western Swiss Alps. On the large scale the underlying control factors that culminated in these observations are best explained looking at the Alps as a whole.

The Alps were formed in consequence of the subduction and collision of the European and Adriatic rifted continental margins. This final collision was preceded by a series of subductions of different geological domains. The first subduction comprises the closure of the Piemonte-Liguria oceanic domain onward from the Early to Middle Eocence (e.g. Lagabrielle and Cannat, 1990; Rebay et al., 2012). Closure of this domain was followed by the subduction of the Briançonnais micro-continent in the Late Eocene (e.g. Bucher et al., 2004). Proceeding, the subduction continued with the Valais domain, which constitutes a ull-apart basin (e.g. Steinmann and Stille, 1999; Masson et al., 2008). Finally, subduction and collision of the rifted European continental margin was initiated in the Early Oligocene resulting in the formation of the present day Alps (e.g. Manzotti et al., 2014). The above described paleogeographic domains were reworked into different large scale structures that encompass distinct, so-called, tectonic nappes in the Alps (e.g. Trümpy et al., 1980). The Helvetic nappe system, which is of particular interest for our studies, corresponds to the former European continental passive margin. Here a large body of literature agrees that the initial geometry of the rifted margin is reflected in the structures we observe today (e.g. Lemoine et al., 1986; Gillcrist et al., 1987). The next two paragraphs will therefore provide a short overview of this so-called structural inheritance.

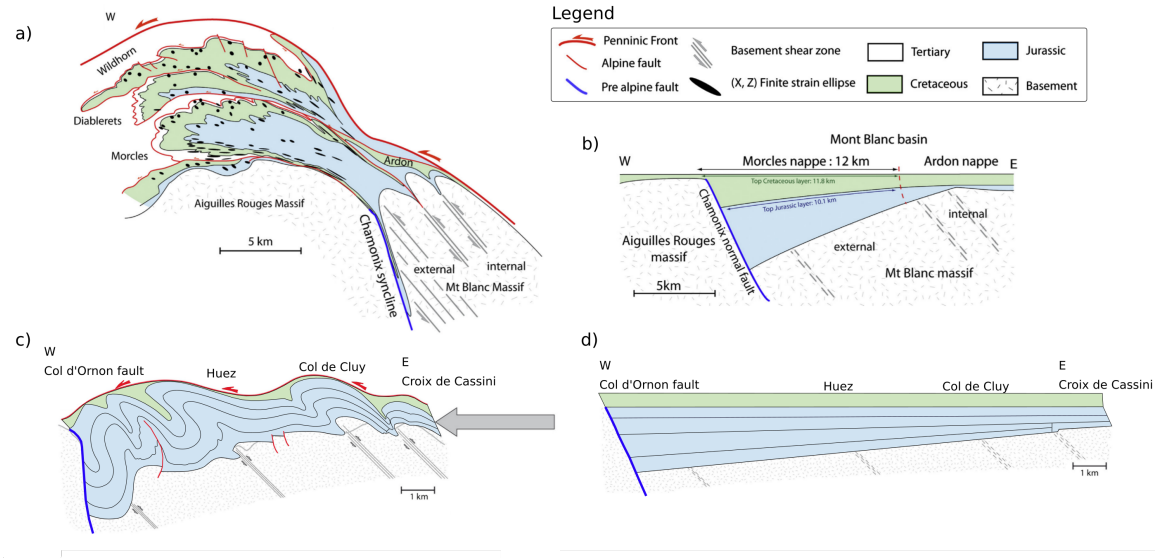

Figure 1.5: Graph displaying a) basin compression resulting in the Morcles nappe (taken from Boutoux et al., 2014, finite strain ellipses after Ramsay and Huber, 1987, cross-sections after Escher et al., 1993) b)reconstruction of the Morcles basin c) simplified cross-section of the Bourg d'Oisons basin displaying buttressing, (modified after Boutoux et al., 2014,) d) simplified paleogeographic reconstruction of the Bourg d'Oisons basin (modified after Boutoux et al., 2014).

1.1.4 Structural inheritance

In general, structural inheritance is widely acknowledged to be one of the most critical components in the evolution of orogens. In the Alps studies as early as 1916 (Argand, 1916) show that many of the structural features such as tectonic nappes were derived from Mesozoic sedimentary basin and half-graben infills (e.g. Helwig, 1976; Butler, 1986; Lemoine et al., 1986). The studies show that these basins were bound by normal faults which played a crucial role during compressional tectonics. In theory such pre-existing normal faults may be reactivated to form basement thrusts (Jackson, 1980). However, complete fault reactivation is commonly not observed in fold and thrust belts (e.g. Buchanan and Buchanan, 1995). Particularly in the Western Alps fault orientation disfavors complete fault reactivation as thrusts (Coward et al., 1994). Nevertheless in the Alps, basement faults acted as important mechanical discontinuities between basement rocks and sedimentary units (e.g. Gillcrist et al., 1987; Coward et al., 1994). Consequently, they had a major influence on the structural evolution. Without reactivation these offsets can result in buckling and folding of the sedimentary sequences during contraction, such as, for example, observed in the Western French Alps (e.g. Boutoux et al., 2014). After Gillcrist et al. (1987) this process is also called buttressing, as displayed in Figure 1.5. Furthermore, basin and graben structures may undergo complete closer during compression, such as, for example, observed at the Morcles nappe (Figure 1.5a,b). In addition,

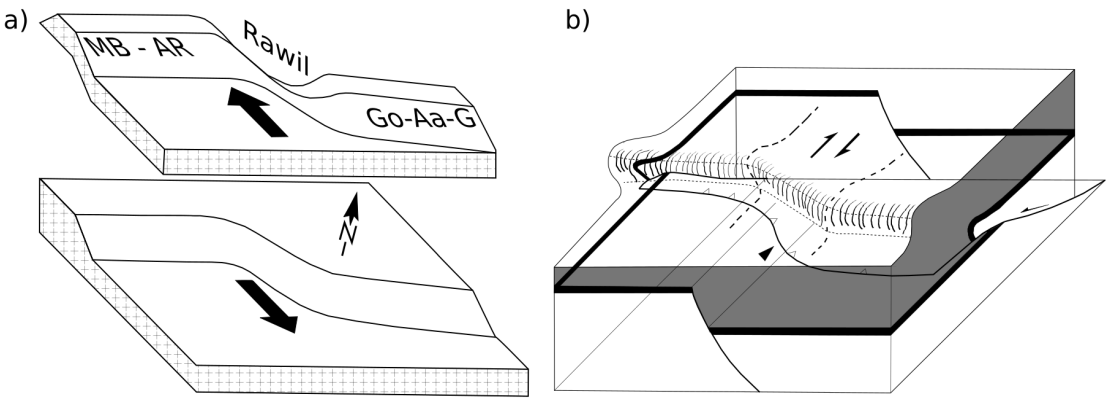

Figure 1.6: a) Model for the formation of the so-called Rawil between the Morcles and Doldenhorn nappe by an oblique basement ramp (modified after Burkhard, 1988),b) Undulations of fold axis and thrust plane caused by a inherited normal fault. Compression parallel to the pre-existing normal fault resulting in the formation of a lateral ramp forms along the inherited anisotropy (redrawn after Doglioni, 1992).

faults can localize thrust ramps (e.g. Coward et al., 1994; Butler, 1986) that influence the developing structure depending on their orientation. Here, several studies in the Alps indicate that oblique or lateral ramps can explain offsets between geological units and structures in the field (e.g. Pfiffner, 1981; Burkhard, 1988; Doglioni, 1992; Zerlauth et al., 2014). For example, Burkhard (1988) explains the lateral offset between the Aiguilles-Rouges and Aar basement massif due to the existence of a lateral basement ramp (Figure 1.6a). Moreover, on a smaller scale, such ramps may also cause the formation of "en échelons" folds (Figure 1.6b).

1.1.5 Mechanical Stratigraphy

Structural inheritance encompasses not only the basement structures, but also structural differences in the overlying sedimentary cover sequences. Here, the inherited mechanical stratigraphy (e.g. Welbon and Butler, 1992; Pfiffner, 1993; Erickson, 1996) has an important impact on the deformational behavior. The term mechanical stratigraphy comprises the mechanical properties, thicknesses and interface boundaries of different rock strata (Laubach et al., 2009). For a rough classification layers are commonly divided into mechanically weak/incompetent and strong/competent layers. These classifications refer to their ability to resist deformation. In general, incompetent units can accommodate larger deformations than competent materials before undergoing plastic failure. They are also more prone to deform in a ductile manner, showing a lower viscosity than competent layers (e.g. Wiltschko and Chapple, 1977; Ferrill et al., 1998; Ferrill et al., 2017). Furthermore, weak layers often act as detachment horizons (e.g. Lacombe and Mouthereau, 2002; Costa and Vendeville, 2002). A typical example for such detachment transport is the Jura fold and thrust belt of the Western Swiss Alps. Here,

Triassic evaporates act as major detachment horizon for the more competent units, such as limestones, above (e.g. Burkhard and Sommaruga, 1998. In addition, faults can have a major impact on the expression of the mechanical stratigraphy. For example, offset and vertical displacement of detachment horizons can lead to the localization of thrust ramps or the initiation of buckle folds (e.g. Butler et al., 2006). Moreover, the mechanical stratigraphy is closely linked to the original depositional environment, as basin and graben structures are often asymmetric exhibiting internal unconformities (e.g. Lister et al., 1986; Froitzheim and Eberli, 1990; Ranero and Pérez Gussinyé, 2010). Consequently, the mechanical stratigraphy can show significant thickness variations in 3D space. In context of the Swiss Alps, one important study investigating such variations of mechanical stratigraphy was conducted by Pfiffner, 1993 in the Helvetic nappe system. Here, Pfiffner (1993) analyzed several stratigraphic cross-sections together with the corresponding large scale structures along strike of the system. On this ground he showed that the thickness ratio between incompetent and competent layers has a decisive impact on the structural style. The study suggests that thickness ratios $n < 0.5$ between incompetent and competent layers favor harmonic folding and/or imbricate thrusting as observed in Northeast and central part of the nappe system. In contrast ratios $n > 0.5$ indicate a mode of disharmonic folding and formation of detachment folds which is encountered to a greater degree in the Southwest of the Helvetic nappes. In this perspective, Jaquet et al. (2014) also performed 2D numerical simulations employing a relatively simple two layer stratigraphy of different n ratios for a series of systemic simulations. In short, their results supports Pfiffners hypothesis. Continuing in Chapter 2 we investigate the impact of such lateral variations of n ratios on the transition between imbricate thrusting and detachment folding using a 3D numerical model.

1.2 The Helvetic nappe system

1.2.1 Nappe tectonics

Tectonics nappes are a widespread structural feature of orogenic belts (e.g. Price and McClay, 1981). Although the definition of nappe may vary (Price and McClay, 1981), most authors agree that a nappe is a coherent rock unit/sheet that has moved away from its autochthonous substratum and thus has become an allochthonous unit (e.g. Termier, 1922; Price and McClay, 1981). Commonly, there exist two end-member types of nappes, namely thrust nappes and fold nappes (e.g. Termier, 1906; Price and McClay, 1981; Epard and Escher, 1996). Thrust nappes are allochthonous tectonic sheets that have been displaced along a prominent basal shear zone or thrust fault. In contrast, a fold nappe is a large-scale recumbent fold that consequently exhibits large-scale stratigraphic inversion with amplitudes exceeding several kilometers (Figure 1.7). The general mechanisms that can drive nappe formation during

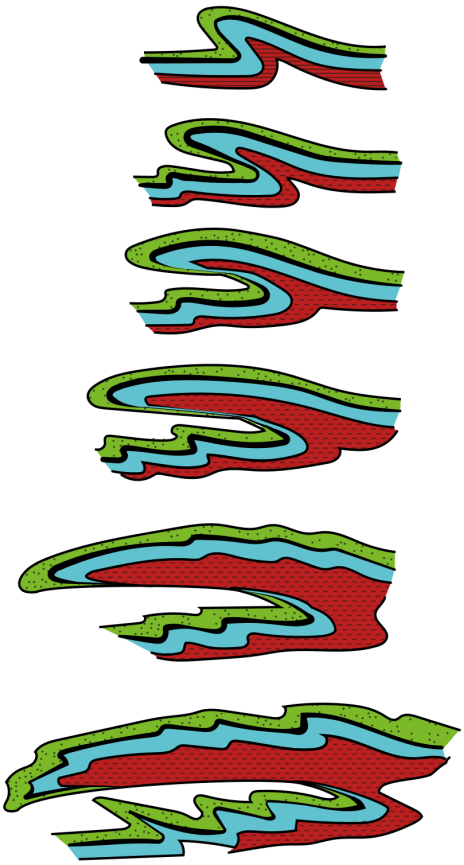

Figure 1.7: Evolution of a fold nappe with an overturned limb with the progressive shearing of the lower limb. (modified after Heim, 1922).

orogeny are well understood. Here, the two major driving forces are either external surface forces (e.g. Ramsay et al., 1983; Epard and Escher, 1996; Boutoux et al., 2014), due to compressional tectonics, or internal body forces (e.g. Durney et al., 1973; Merle, 1998) due to gravity. However, the physical mechanisms of nappe initiation, as well as the transport and stacking are still incompletely understood. Hence, there exist a large body of studies employing theoretical and analogue models to investigate the formation of fold-and-thrust belts and of nappes (e.g. Rubey and King Hubbert, 1959; Merle, 1989; Wissing and Pfiffner, 2003; Bauville et al., 2013; Poulet et al., 2014; Jaquet et al., 2014; Ruh et al., 2014; Bauville and Schmalholz, 2017). For example, the dominant emplacement mechanism of fold nappes is still controversial. Here, many authors favor dominantly ductile deformation mechanisms, such as dislocation or grain-size sensitive diffusion creep under distributed shearing (e.g. Ramsay et al., 1983; Gillcrist et al., 1987; Ebert et al., 2008; Bauville et al., 2013). In contrast, several other investigators argue for localized thrusting under dominantly britte-plastic deformation mechanisms, such as fluid pressure induced fracturing (e.g. Boyer and Elliott, 1982; Granado

and Ruh, 2019). For thrust nappes the proposed emplacement mechanisms show an even larger variety (Merle, 1989). Initial attempts to describe the movement of large thrust sheets by frictional sliding culminated in the so-called overthrust paradox. In short, the paradox states, that the required stresses to transport long sheets over a frictional surface exceed the internal strength of the rock sheet. Hence, the displacement of large rock sheets would result in the fragmentation of the sheet (e.g. Smoluchowski, 1909; King Hubbert and Rubey, 1959; Price, 1988). Consequently, several authors suggested different solutions to the apparent paradox. Famously King Hubbert and Rubey (1959), for example, proposed the reduction of the effective friction angle at the thrust base by elevated pore fluid pressure causing a reduction in the required effective stresses to move the sheet. Other authors favored a dominantly ductile deformation mechanism (e.g. Smoluchowski, 1909) combined with thermally-, chemically- or mechanically-activated softening mechanisms (e.g. Poirier, 1980; Ebert et al., 2008; Poulet et al., 2014). However, an additional problem of purely brittle-frictional emplacement models is that thrusts sheets often show a displacement of several tens of kilometers on a sub-horizontal thrust plane. This model is therefore in conflict with Anderson's theory of faulting. After Anderson's theory thrust planes of friction angles of 30° should also dip with 30° in respect to the horizontal, if the principal stress σ_1 is approximately horizontal. Furthermore, smaller friction angles would increase the dip angle. It is therefore likely that prominent low-angle thrust planes are controlled by mechanical heterogeneities, such as the basement highs or the spatial distribution of mechanical stratigraphy, as has been suggested for the Helvetic nappe system (e.g. Pfiffner, 1993; Steck, 1999; Bauville and Schmalholz, 2017).

1.2.2 The Helvetic nappe system: A short geological overview

The Helvetic nappe system of the Western Swiss Alps represents a classical fold and thrust belt. It has been studied extensively since the beginning of the 20th century (e.g. Argand, 1916, Heim, 1922) and as such had a major impact on the evolution of the nappe theory. The Helvetic nappe system can be subdivided into three major units that are from top to bottom: The Ultrahelvetics, The Helvetic nappes proper, and the Infrahelvetic complex. The Helvetic nappes are mainly composed of Mesozoic and Triassic sediments that have been detached and translated away from its original pre-Triassic crystalline basement. Here, paleogeographic reconstructions show that the units were derived from the former European continental passive margin (e.g. Ramsay, 1981, Pfiffner, 1993, Schmid et al., 2004). The predominant sedimentary units are limestones, marls and shales. Altogether the stratigraphy shows significant thickness variations in N-S direction of the system. These thickness changes are reflected in the structural variations along-strike. Furthermore, the the Helvetic nappes were displaced along major basal detachment horizons that originated in the weaker sediments units, such as Triassic evaporites, or Lower and Middle Jurassic shales (e.g. Pfiffner, 2015). Upon thrusting the Helvetic nappes were placed on the Infrahelvetic complex which is com-

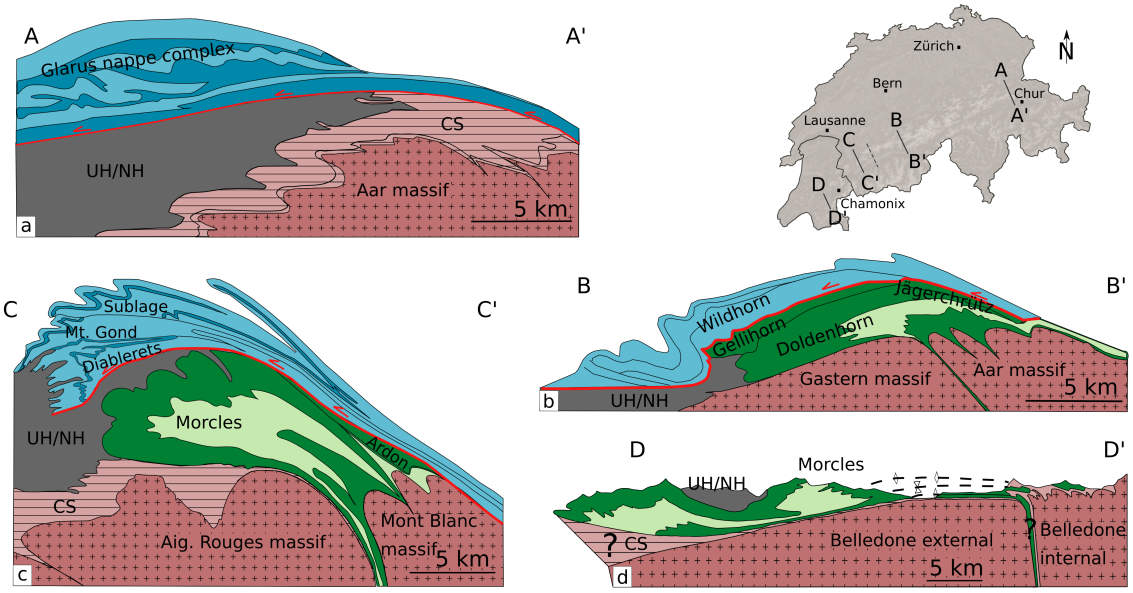

Figure 1.8: Simplified geological cross-sections along strike of the Helvetic nappe system. a) Glarus nappe complex (modified after Pfiffner, 2015; b) Doldenhorn nappe (modified after Kirschner et al., 1999)c) Morcles nappe (modified after Escher et al., 1993); d) Morcles nappe at the Belledonne massif (modified after Epard, 1990) CS = cover sediments, UH/NH = Ultrahelvetics/ North Helvetics.

prised of autochthonous Mesozoic and Tertiary cover-sediments that remained in contact with the underlying autochthonous crystalline basement massifs. These basement massifs have also been deformed significantly during the Alpine orogeny showing an elongated dome-like shape (Ramsay, 1981). In detail, from SW to NE there are two major pairs of basement massifs that are separated by a steep cuspate syncline. They are namely, the Aiguilles-Rouges and Mont Blanc, and the Gastern and the Aar massif.

As mentioned above, the structural variations of the Helvetic nappes are significant along-strike (Figure 1.8). Beginning in the SW of Switzerland we find a vertical succession of nappes that have been displaced on top of each other, forming a so-called nappe stack. From bottom to top, the crystalline Aiguilles-Rouges basement massif with its authochthonous Mesozoic cover sediments is overlain by a large recumbent fold, namely the Morcles nappe (Figure 1.8c). The Morcles fold nappe is the result of the closure and inversion of an inherited half-graben that was once situated in the former continental passive margin. At the bottom, the overturned limb of the Morcles nappe can be traced back to the steep Chamonix-Martigny syncline that divides Aiguilles-Rouges from the Mont Blanc massif. Here, an increase of ductile strain together with a thinning the limb is observed in direction of the root zone (e.g. Dietrich and Casey, 1989). In addition, finite strain analysis indicates a combination of layer parallel compression and top to the NW shearing for the Morcles nappe (Ramsay, 1981; Ramsay et al., 1983; Escher et al., 1993). Moreover, the competence contrast between the strong limestones units and weak shales

and marls resulted in the buckling and folding of the former during graben closure, leading to parasitic folds inside the nappe. Hence, field evidences suggests a ductile deformation regime during nappe emplacement. The Morlces nappe itself is overlain by a narrow thrust sheet which is called the Ardon nappe (Masson et al., 1980) and another major thrust nappe namely, the Wildhorn super nappe. The Wildhorn super nappe itself can be subdivided into three smaller units called the Mont Gond, the Sublage nappe and the Diablerets nappe. Above and in between the Helvetic nappes lie the Ultrahelvetic nappes (UH/NH). They exhibit a recumbent synform between the Morcles and Diablerets nappes which suggests that the Ultrahelvetics where initially located on top of the undeveloped Helvetic Nappes. Afterwards the Ultrahelvetics were reworked and refolded during the shortening stage that resulted in the emplacement of the Helvetic nappes (Ramsay et al., 1983). Furthermore, the Morcles nappe can be traced across the Swiss border in the SW to the Western French Alps. Here, the Morcles nappe (Figure 1.8d) can be subdivided into two highly thinned out recumbent anticlines, namely the Sangle and Mont Joly Unit (not shown in the simplified cross-section). These units also represent the infill of a former half-graben which has been squeezed out and displaced on top of adjacent external Belledonne crystalline massif (Epard, 1990).

Continuing eastwards from the Swiss-part of the Morcles nappe to the central part of the Helvetic nappe system three major nappes emerge on top of the Aar massif (Figure 1.8b). Similarly to the Southwestern part we find several nappes stacked on top of the autochthonous basement massifs. From bottom to top, the stack consists of the Doldenhorn fold nappe, the Gellihorn and the Wildhorn nappe. These nappes are homologues to the Morcles and the Wildhorn super nappe. In contrast to the Morcles nappe, the Doldenhorn nappe shows a less prominent recumbent fold limb as well as an elongated shape with greater localized shearing at its base (Steck, 1999). This slight change in style is likely related to changes in the mechanical stratigraphy and half-graben geometry. In this context Pfiffner et al. (2011) suggests that here the weak basal units are relatively thinner compared to the equivalent units at the Morcles nappe.

Proceeding to the Eastern end of Switzerland the autochthonous cover sediments of the Gastern and Aar massif is overlain by Infrahelvetic slices of Tertiary flysch and Mesozoic sediments that were subsequently overthrusted by Helvetic nappes (Figure 1.8a). In contrast to the Southwestern and Central Helvetic zone there is no record of a recumbent fold nappe such as the Morcles or Doldenhorn nappe. Here the Helvetic nappes manifest themselves in the prominent Glarus nappe complex (Figure 1.8a) that shows up to 50 km greater displacement than the Helvetic nappes to the West (e.g Schmid, 1975; Groshong Jr et al., 1984). The complex comprises three different major thrust sheets, namely, from bottom to top the Glarus nappe, the Muertschen nappe and the Saentis nappe (not shown in the simplified cross-section). The Glarus nappe consists of a thick unit of Permian Verrucano that is overlain by folded Mesozoic and Tertiary sediments. Furthermore, the contact at the basal thrust of the

Glarus nappe is extremely sharp and displays a strongly deformed calc-mylonite that reaches a maximum thickness of a few meters (e.g. Schmid, 1975; Milnes and Pfiffner, 1977).

The emplacement of the Helvetic nappes took place from the Oligocene to Miocene times and lasted approximately 10 to 15 Ma (e.g. Masson et al., 1980; Kirschner et al., 1996; Stampfli et al., 2002; Herwegh and Pfiffner, 2005). In addition, the temperature conditions during emplacement are well constrained by thermochronological studies which show metamorphic peak temperatures ranging from around $200°C$ to $400°C$ at the basal contacts of the nappes. Here, further constrains are given by metamorphic peak temperatures for the Mont Blanc massif indicating temperatures of approximately $400°C$ (Leloup et al., 2005). Hence, the temperature data supports the field evidences which suggests that the nappes were largely formed in a ductile flow regime.

1.3 Approach

In computational geodynamics it is common practice to utilize 2D and 3D numerical models to simulate and investigate a variety of processes occurring on and in planet Earth. These processes are of numerous different scales, ranging from mantle convection, subducting plates, lithospheric folding, shear zone formation and porosity wave evolution. Particularly, large scale deformations in the mantle or lithosphere can be approximated by the so called Stokes equations. These Stokes equations are based on the classic theory of continuum mechanics. Usually the Stokes equations are used to model the flow of incompressible fluids. Coincidentally, rocks behave in similar manner to an incompressible fluid over million year long time scales. Hence, the herein presented models of viscous folding and tectonic nappe stack emplacement are likewise based on the same principles. Following section will present the reader with a brief overview of the continuum mechanics and numerical approach utilized in this work.

1.3.1 Continuum Mechanics

The theory of continuum mechanics describes a collection of fundamental physical laws that are used to predict material behavior during the application of mechanical forces. The term 'continuum' implies that any material is modeled as perfect continuous body without any discontinuities. Hence, to predict the material behavior in a closed physical system there are four fundamental physical conservations laws that need to be respected. These laws are the conservation of mass, the conservation momentum and angular momentum and the conservation of energy. In this context conservation means that all three quantities, mass, momentum and energy are constant and thus are not allowed to change over time in a closed system. The conservation laws provide a set of equations that have to be solved in order to

understand and quantify the mechanical behavior of a given system (e.g. Gurtin, 1982; Mase, 1970; Ferziger and Perić, 2002).

Conservation principles

A general way to derive conservation laws is to consider a certain control mass (CM) or system and its extensive properties. That is, physical properties that depend on the system size, such as mass, momentum, or energy. In short, a conservation laws accounts for the rate of change the amount of an extensive property inside a specified control mass or system in relation to external effects. However, in a fluid dynamics approach, like the Stokes flow, it is more convenient to deal with the fluid flow through a specifically defined control volume instead of a continuum body. By employing the control volume approach the focus is shifted away from the extensive properties to the intensive properties (e.g. ρ, v). For example, any given extensive property Φ can be related to corresponding intensive property ϕ in the following way (e.g. $\phi = 1$ for mass conservation):

$$\Phi = \int\limits_{\Omega_{\mathrm{CM}}} \rho\phi \mathrm{d}\Omega \tag{1.1}$$

Where Ω_{CM} refers to the Volume occupied by the control mass (CM) and ρ to the density. Continuing, the general conservation law can be defined by applying the Reynold's transport theorem:

$$\frac{\mathrm{d}}{\mathrm{d}t} \int\limits_{\Omega_{CM}} \rho\phi d\Omega = \frac{\mathrm{d}}{\mathrm{d}t} \int\limits_{\Omega_{CV}} \rho\phi \mathrm{d}\Omega + \oint\limits_{CV} \rho\phi(\boldsymbol{v} - \boldsymbol{v}_{\mathrm{b}})\boldsymbol{n}\mathrm{d}S \tag{1.2}$$

Where the first term Ω_{CV} on the right side refers to the control volume and the second term to the surface of the control volume CV, with $\boldsymbol{v}$ being the fluid velocity, $\boldsymbol{v}_{\mathrm{b}}$ the velocity of the the surface and $\boldsymbol{n}$ the unit vector orthogonal to the surface. In most cases we consider a fixed CV, leading to $\boldsymbol{v}_{\mathrm{b}} = 0$, transforming the first derivative on the right side to a partial derivative.

Conservation of mass

If we consider a fixed control volume using equation (1.2) we can find the law of mass conservation by setting $\phi = 1$, under the assumption that mass is neither created nor destroyed in our system:

$$\frac{\partial}{\partial t} \int\limits_{\Omega_{\mathrm{CV}}} \rho d\Omega + \oint\limits_{CV} \rho \boldsymbol{v}\boldsymbol{n} \mathrm{d}S = 0. \tag{1.3}$$

$$\frac{\partial \rho}{\partial t} + \nabla(\rho v) \tag{1.4}$$

In our approach we treat the long-term deformational behavior of rocks as analogue to that of an incompressible flow. This assumptions implies that the density is constant inside a control volume. In addition, the statement of incompressibility demands the divergence of the flow velocity to be zero. Equation (1.3) can therefore be simplified to

$$\frac{\partial v_i}{\partial x_i} = 0 \tag{1.5}$$

Where x_i(i = 1,2,3) refers to Cartesian coordinates in the three spatial directions, v_i are the components of the velocity vector,

Conservation of momentum

The conservation of momentum for the incompressible Stokes flow can be derived in similar way employing the above Reynold's transport theorem (e.g. Müller and Müller, 2009). Thus the law is given by:

$$-\frac{\partial P}{\partial x_i} + \frac{\partial \tau_{ij}}{\partial x_j} = \rho g_i \tag{1.6}$$

$$\tag{1.7}$$

Here, P is the pressure, $\tau_{ij} = \sigma_{ij} + P\delta_{ij}$ are components of the deviatoric Cauchy stress tensor, ρ is the density and g_i the gravity acceleration vector.

Conservation of energy

Proceeding, the conservation of energy is given by following statement:

$$\rho C_{\mathrm{p}} \frac{\partial T}{\partial t} = \frac{\partial}{\partial x_i} \left(\lambda \frac{\partial T}{\partial x_i} \right) + H_{\mathrm{R}} + H_{\mathrm{S}} \tag{1.8}$$

Here, C_p stands for the specific capacity, T for temperature and λ for the thermal conductivity. The source term H_R refers to the radiogenic heat production and H_S for shear heating that are defined as follows:

$$H_\mathrm{S} = \tau_\mathrm{ij}\dot{\epsilon}_\mathrm{ij} \tag{1.9}$$

Where τ_ij is the deviatoric Cauchy stress tensor and $\dot{\epsilon}_{ij}$ the deviatoric strain rate tensor.

Constitutive equations

The deformational behavior of rocks depends on their material properties (e.g. chemical composition, grain size), external conditions (e.g. temperature, stress) and varies across different timescales (e.g. Ranalli, 1995, Karato, 2012). For example, on the time scale of seconds to minutes rocks behave in a elastic manner. Whereas, they generally act in a brittle-ductile manner in the timescale of million years. The transition between brittle behavior, which implies fracturing, and ductile behavior, inferring ductile flow, depends largely on the confining pressure, temperature and strain rate. The complete mathematical framework of rheology of rocks is provided by the visco-elasto-plastic constitutive equations that relate stress to strain rates. However, in the perspective of the herein presented studies we explicitly utilize a sole viscous rheology (Chapter 2) and visco-plastic rheology (Chapter 3). Hence, we refrain from the description of elastic rheology.

The components of the deviatoric strain rate tensor $\dot{\epsilon}_{ij}$ are defined by the visco-plastic constitutive equations: where $\dot{\epsilon}^{vs}_{ij}$ is the viscous strain rate tensor, $\dot{\epsilon}^{pl}_{ij}$ is the plastic strain rate tensor, η_{eff} is the effective viscosity, τ_{ij} are components of the deviatoric stress tensor and $\tau_{II} = (\frac{1}{2}\tau_{ij}\tau_{ij})^{\frac{1}{2}}$ is the square root of the second invariant of the deviatoric stress tensor.

$$\dot{\epsilon}_{ij} = \dot{\epsilon}^{vs}_{ij} + \dot{\epsilon}^{pl}_{ij} = \frac{\tau_{ij}}{2\eta_{eff}} + \dot{\epsilon}^{pl}_{II}\frac{\tau_{ij}}{\tau_{II}} \tag{1.10}$$

Viscous creep The viscous deformation of crustal rocks is mainly governed by the so-called dislocation creep (e.g. Ranalli, 1995, Karato, 2012). Dislocation creep is the result of the displacement of crystallographic defects, known as dislocations, inside a crystal lattice. Movement of such dislocations permanently deforms the crystal lattice and can, for example, culminate in crystal preferred orientations (CPO). Commonly, dislocation creep flow laws of rocks are measured under laboratory conditions and then extrapolated to geological conditions (stress, strain rate, temperature). A standard formulation for the effective temperature dependent viscosity η_eff for a dislocation creep-mechanism is given by:

$$\eta_\mathrm{eff} = \frac{1}{2}\left(B_n\right)^{-\frac{1}{n}}\left(\dot{\epsilon}_{II}\right)^{\frac{1}{n}-1} exp\left(\frac{E_n}{nRT}\right) \tag{1.11}$$

Where n is the power-law stress exponent, $\dot{\epsilon}_{\mathrm{II}} = (\frac{1}{2}\dot{\epsilon}_{ij}\dot{\epsilon}_{ij})^{\frac{1}{2}}$ the square root of the second invariant of the strain rate tensor, B_n the creep constant, E_n the activation energy, R the universal gas constant and T the temperature.

Plasticity Rocks undergo plastic failure when they are subjected to their maximum amount of sustainable shear stress. This relationship is well understood by the so-called Byerlee's law (Byerlee, 1978). To facilitate plastic failure in our model we enforce the pressure-dependent Drucker-Prager yield criterion (Drucker and Prager, 1952) given by:

$$\tau_{II} \leq \tau_Y = \sin(\phi)P + \cos(\phi)C \tag{1.12}$$

Here, $\tau_{\mathrm{II}} = (\frac{1}{2}\tau_{ij}\tau_{ij})^{\frac{1}{2}}$ is the square root of the second invariant of the deviatoric stress tensor, τ_Y is the yield stress, ϕ the friction angle, P the pressure, and C the cohesion.

1.3.2 Numerical framework

The three dimensional (3D) numerical simulations presented in this thesis were conducted with the 3D parallel FDSTAG LaMEM Lithosphere and Mantel Evolution Model code (`https://bitbucket.org/bkaus/lamem`). The LaMEM code is based on the finite difference method, which means that the conservation equations above are discretized using a finite difference approach. That is, a low-order, stable discretization in space using a staggered grid (FDSTAG) approach. The LaMEM code is built upon the Portable Extensible Toolkit for Scientific Computation library (PETSc, Balay et al., 2019) which i.a. provides the framework for the computational parallelization of the code. That is, PETSc is provides the user with the necessary MPI algorithms to simplify the utilization of parallel computing. Furthermore, LaMEM accesses the PETSc library which provides distributed arrays (DMDA), a suite of pre-conditioners, linear and non-linear iterative solvers or Galerking multi-grid solver. Hence, PETSc provides a stable computational base to focus on the programming of numerical algorithms to solve physical problems (see Kaus et al., 2016 for a more detailed review of the solvers).

Furthermore, a free surface boundary condition and dynamic evolution of topography is implemented via the so-called sticky air approach. The approach utilizes a low viscosity air phase in combination with a stabilization algorithm (Kaus et al., 2010, Duretz et al., 2011) to account for numerical instabilities ('drunken sailer' instability). In particular, such numerical instabilities may arise in consequence of rather large numerical timesteps that are required to compute geological problems in a sufficient amount of real time. Further, the topography of the free surface is explicitly tracked on a 2D grid.

The advection and deformation of material is modeled by employing a maker and cell (MAC) method (e.g. Harlow and Welch, 1965; Gerya and Yuen, 2003. Thus material properties are

stored and traced on numerous markers that are advected through the grid cells. Spurious clustering of the markers is prevented by a combination of a 4th order Runge-Kutta advection with a conservative velocity interpolation scheme.

The simulations presented herein were primarily computed on the local 'octopus' super computing cluster at the University of Lausanne. However, some high resolution results were achieved by utilizing the Piz Daint cluster at the CSCS in Lugano (Chapter 5). In this context, we also performed benchmarks in order to gain access to the cluster. In order to our results we generally used the ParaView software suite which allowed for additional self-made python scripts to automatize the visualization and data extraction. Additionally we created our own Python based visualization schemes to create a detailed 2D cross-sectional analysis (Chapter 3).

1.3.3 Finite strain computation

This section comprises a short overview of the algorithm that was implemented in LaMEM to compute the evolution of 3D finite strain. In geology finite strain analysis is one of the major methods to obtain information on the deformation and mechanical properties of natural rocks. Additional information on the application and importance of finite strain can be found in Chapter 2. In general, the undeformed state of an 3D object can be represented by a unit sphere. Deformation of this unit sphere results in the development of an ellipsoid, also called the finite strain ellipsoid. The finite strain ellipsoid is characterized by the orientation and magnitude of its three principal strain axes. In order to obtain the principal strain axes we calculate the finite strain tensor. In our numerical approach we compute the finite strain tensor from the finite deformation gradient tensor $\boldsymbol{F}$ following a standard continuum mechanics approach. (e.g. Bower, 2009; Ragan, 2009). In order to trace the evolution of finite strain we accumulate and store $\boldsymbol{F}$ on our numerical markers. To obtain $\boldsymbol{F}$ we first compute the incremental deformation gradient tensor $\boldsymbol{\Delta F}$ for every time step from the velocity field:

$$\boldsymbol{\Delta F} = \boldsymbol{I} + \frac{\partial \boldsymbol{v}}{\partial \boldsymbol{x}} \Delta t, \tag{1.13}$$

where $\boldsymbol{I}$ is the second order identity tensor, $\boldsymbol{v}$ the velocity vector, $\boldsymbol{x}$ the spatial coordinate vector, and Δt the time step. The second term of equation (1.13) is also called the displacement gradient tensor and is an approximation derived from a Taylor series expansion, where the higher order terms are dropped. We continue with the successive update of the deformation gradient tensor $\boldsymbol{F}$ which is analogues cumulative coordinate mapping. That is, we consider a coordinate map $\boldsymbol{x} = \boldsymbol{x}(\boldsymbol{X}, t)$, where the current coordinates $\boldsymbol{x}$ are a function of the original coordinates $\boldsymbol{X}$ and time, we can use the chain rule on a time step:

$$\frac{\partial \boldsymbol{x}_{n+1}}{\partial \boldsymbol{X}} = \frac{\partial \boldsymbol{x}_{n+1}}{\partial \boldsymbol{x}_n} \frac{\partial \boldsymbol{x}_n}{\partial \boldsymbol{X}} \tag{1.14}$$

Table 1.1: Relation between Lode's ratio ν, ellipsoid shape and deformation regime.

ν	ellipsoid shape	deformation regime
< 0	oblate	constrictional
0	oblate-prolate	plain strain
> 0	prolate	flattening

After equation (1.14), the deformation gradient tensor $\boldsymbol{F}$ is updated from the previous time step in a multiplicative manner:

$$\boldsymbol{F}_{n+1} = \boldsymbol{\Delta F}\, \boldsymbol{F}_n, \tag{1.15}$$

where $\boldsymbol{F}_n$ and $\boldsymbol{F}_{n+1}$ are the deformation gradients in the beginning and in the end of a time step, respectively. We proceed with the polar decomposition of the deformation gradient:

$$\boldsymbol{F} = \boldsymbol{V}\, \boldsymbol{R}, \tag{1.16}$$

where $\boldsymbol{R}$ is a proper orthogonal tensor representing rigid body rotation, and $\boldsymbol{V}$ is a symmetric positive definite tensor representing finite strain in the current configuration, which is called the left stretch tensor. The polar decomposition can be performed by computing the spectral representation of the left Cauchy-Green deformation tensor $\boldsymbol{B}$ as follows:

$$\boldsymbol{B} = \boldsymbol{F}\boldsymbol{F}^T = \boldsymbol{V}^2 = \sum_{i=1}^{3} \lambda_i^2\, \boldsymbol{n}_i \otimes \boldsymbol{n}_i \tag{1.17}$$

Here λ_i and $\boldsymbol{n}_i$, respectively, are the eigenvalues and the eigenvectors of the left stretch tensor $\boldsymbol{V}$. The eigenvalues represent principal strains, and the eigenvectors represent the directions of the principal strain axes. Both quantities are required to visualize the finite strain ellipsoid.

In order to quantify and visualize the finite strain tensor we compute and plot the strain magnitude and the strain symmetry. Both values are obtained from the finite strain tensor. The strain magnitude or strain intensity can be expressed by the octahedral shear strain ε_s (Nádai and Hodge, 1963), also called Nádai strain. It provides a non-dimensional measure on the amount of strain that was applied during a homogeneous deformation. The second parameter is the Lode's ratio ν (Lode, 1926) and describes the strain symmetry, the shape of the ellipsoid. Moreover, the Lode's ratio ν is restricted to values between -1.0 and 1.0, which indicate the strain ellipsoid shape that can be related to the deformation regime (cp. Table 1.1).

In Chapter 2 we will show how to calculate the Nádai strain and how to relate both values together in a so-called Hsu diagram (Hsu, 1966; Hossack, 1968). Furthermore supplement two matlab codes in the Appendix to demonstrate the computation of 2D and 3D finite strain.

1.3.4 Aim and structure of this thesis

Aim of this thesis is to gain additional insights in the formation and evolution of fold and thrust nappe emplacement using three-dimensional (3D) thermo-mechanical numerical modelling. We first focus on the 3D computation and quantification of 3D finite strain during simultaneous thrusting and folding, based an previous 2D work by Jaquet et al. (2014). Here, finite strain computation allows us to identify and characterize the transition between 3D folding and thrusting in regards to the strain magnitude, deformation regime and orientation of the finite strain principal axis. Further attention is focused on the three-dimensional modelling of fold and thrust nappe stacking as observed in the Helvetic nappe system. In this context, we are particularly interested in the effect of laterally variable half-graben structures on 3D nappe formation and structure. Moreover, we compare our model results to geological datasets of the Helvetic nappe system. In summary, we are able to reproduce first order key features of the Helvetic nappe systems, as for example, the structural and kinematic evolution, as well the thermal structure during emplacement of the nappes.

In particular we provide new answers or show new aspects for following questions:

- How can we compute and visualize 3D finite strain?
- How does a laterally variable mechanical stratigraphy effect the simultaneous processes of viscous folding and over-thrusting?
- What characterizes the transition between over-thrusting and folding in 3D space?
- Does the internal formation of folds and thrusts induce strike-slip movements under a bulk pure shear compression?
- How is a three-dimensional nappe stack formed?
- What is the effect of lateral variable half-graben geometry on nappe emplacement and nappe structure?
- In what degree does underlying fold nappe formation effect the superposition of thrust sheets during nappe stacking?

In Chapter 2 we present the results of a 3D mechanical numerical model employing a laterally variable mechanical stratigraphy based on field observations by Pfiffner, 1993 in the Helvetic nappe system. Moreover, our model configuration is based on previous 2D numerical results (Jaquet et al., 2014) which allows us to focus on effect of different 3D geometries during folding and thrusting. Furthermore, we present 3D strain analysis of several simulations with different initial distribution of mechanical stratigraphy. Here, the deformation regime and finite strain gradient reflect the initial model geometry. Proceeding, in Chapter 3 we present results of 3D thermo-mechanical numerical simulations with a visco-plastic rheology modelling fold and thrust nappe stacking. Nappe stacking is induced by simulating the compression of a passive margin during orogenic wedge formation, mimicking the conditions during Alpine orogeny. Here, we show for the first time, how fold and thrust nappe stacking takes places in

three-dimensional space. In conclusion, our model results are in first order agreement with the structural, kinematic and thermal datasets of the Helvetic nappe systems of the Swiss Alps. Chapter 4 consists of a short summarizing discussion and conclusion together with an outlook for future work. The final chapter (Chapter 5) is the Appendix and includes two Matlab scripts demonstrating 2D and 3D finite strain calculation, and a performance benchmark of the LaMEM code.

Bibliography

Allmendinger, R.W., Jordan, T.E., Kay, S.M., Isacks, B.L., 1997. The evolution of the Altiplano-Puna plateau of the Central Andes. Annual review of earth and planetary sciences 25, 139–174.

Argand, E., 1916. Sur l'arc des Alpes occidentales. G. Bridel.

Balay, S., Abhyankar, S., Adams, M., Brown, J., Brune, P., Buschelman, K., Dalcin, L., Dener, A., Eijkhout, V., Gropp, W., et al., 2019. PETSc users manual .

Bally, A.W., Gordy, P., Stewart, G.A., 1966. Structure, seismic data, and orogenic evolution of southern Canadian Rocky Mountains. Bulletin of Canadian Petroleum Geology 14, 337–381.

Bauville, A., Epard, J.L., Schmalholz, S.M., 2013. A simple thermo-mechanical shear model applied to the Morcles fold nappe (Western Alps). Tectonophysics 583, 76–87.

Bauville, A., Schmalholz, S.M., 2017. Tectonic inheritance and kinematic strain localization as trigger for the formation of the Helvetic nappes, Switzerland. Swiss Journal of Geosciences 110, 523–534.

Bellahsen, N., Jolivet, L., Lacombe, O., Bellanger, M., Boutoux, A., Garcia, S., Mouthereau, F., Le Pourhiet, L., Gumiaux, C., 2012. Mechanisms of margin inversion in the external Western Alps: Implications for crustal rheology. Tectonophysics 560, 62–83.

Boutoux, A., Bellahsen, N., Lacombe, O., Verlaguet, A., Mouthereau, F., 2014. Inversion of pre-orogenic extensional basins in the external Western Alps: structure, microstructures and restoration. Journal of Structural Geology 60, 13–29.

Bower, A.F., 2009. Applied mechanics of solids. CRC press.

Boyer, S.E., Elliott, D., 1982. Thrust systems. Aapg Bulletin 66, 1196–1230.

Buchanan, J.G., Buchanan, P.G., 1995. Basin inversion. volume 88. Geological Society London.

Bucher, S., Ulardic, C., Bousquet, R., Ceriani, S., Fügenschuh, B., Gouffon, Y., Schmid, S.M., 2004. Tectonic evolution of the Briançonnais units along a transect (ECORS-CROP) through the Italian-French Western Alps. Eclogae Geologicae Helvetiae 97, 321–345.

Buiter, S.J., 2012. A review of brittle compressional wedge models. Tectonophysics 530, 1–17.

Burkhard, M., 1988. L'Helvétique de la bordure occidentale du massif de l'Aar (évolution tectonique et métamorphique). Eclogae Geologicae Helvetiae 81, 63–114.

Burkhard, M., Sommaruga, A., 1998. Evolution of the western Swiss Molasse basin: structural relations with the Alps and the Jura belt. Geological Society, London, Special Publications 134, 279–298.

Butler, R., 1986. Thrust tectonics, deep structure and crustal subduction in the Alps and Himalayas. Journal of the Geological Society 143, 857–873.

Butler, R., 1989. The influence of pre-existing basin structure on thrust system evolution in the Western Alps. Geological Society, London, Special Publications 44, 105–122.

Butler, R.W., Tavarnelli, E., Grasso, M., 2006. Structural inheritance in mountain belts: an Alpine–Apennine perspective. Journal of structural geology 28, 1893–1908.

Byerlee, J., 1978. Friction of rocks, in: Rock friction and earthquake prediction. Springer, pp. 615–626.

Cooper, M., 2007. Structural style and hydrocarbon prospectivity in fold and thrust belts: a global review. Special Publication-Geological Society of London 272, 447.

Costa, E., Vendeville, B., 2002. Experimental insights on the geometry and kinematics of fold-and-thrust belts above weak, viscous evaporitic décollement. Journal of Structural Geology 24, 1729–1739.

Coward, M., 1983. Thrust tectonics, thin skinned or thick skinned, and the continuation of thrusts to deep in the crust. Journal of Structural Geology 5, 113–123.

Coward, M., Enfield, M., Fischer, M., 1994. Inversion tectonics. Continental deformation , 289–304.

Coward, M., Gillcrist, R., Trudgill, B., 1991. Extensional structures and their tectonic inversion in the Western Alps. Geological Society, London, Special Publications 56, 93–112.

Dahlen, F., Suppe, J., Davis, D., 1984. Mechanics of fold-and-thrust belts and accretionary wedges: Cohesive Coulomb theory. Journal of Geophysical Research: Solid Earth 89, 10087–10101.

Dahlstrom, C., 1969. Balanced cross sections. Canadian Journal of Earth Sciences 6, 743–757.

Davis, D., Suppe, J., Dahlen, F., 1983. Mechanics of fold-and-thrust belts and accretionary wedges. Journal of Geophysical Research: Solid Earth 88, 1153–1172.

Fitz Diaz, E., Hudleston, P., Tolson, G., 2011. Comparison of tectonic styles in the Mexican and Canadian Rocky Mountain fold-thrust belt. Geological Society, London, Special Publications 349, 149–167.

Dietrich, D., Casey, M., 1989. A new tectonic model for the Helvetic nappes. Geological Society, London, Special Publications 45, 47–63.

Doglioni, C., 1992. Relationships between Mesozoic extensional tectonics, stratigraphy and Alpine inversion in the Southern Alps. Birkhäuser.

Drucker, D.C., Prager, W., 1952. Soil mechanics and plastic analysis or limit design. Quarterly of applied mathematics 10, 157–165.

Dunn, J.F., Hartshorn, K.G., Hartshorn, P.W., 1995. Structural styles and hydrocarbon potential of the sub-Andean thrust belt of southern Bolivia .

Duretz, T., May, D.A., Gerya, T., Tackley, P., 2011. Discretization errors and free surface stabilization in the finite difference and marker-in-cell method for applied geodynamics: A numerical study. Geochemistry, Geophysics, Geosystems 12.

Durney, D., Ramsay, J., DeJong, K., Scholten, R., 1973. Gravity and tectonics .

Ebert, A., Herwegh, M., Berger, A., Pfiffner, A., 2008. Grain coarsening maps for polymineralic carbonate mylonites: a calibration based on data from different Helvetic nappes (Switzerland). Tectonophysics 457, 128–142.

Epard, J.L., 1990. La nappe de Morcles au sud-ouest du Mont-Blanc. Ph.D. thesis.

Epard, J.L., Escher, A., 1996. Transition from basement to cover: a geometric model. Journal of Structural Geology 18, 533–548.

Erickson, S.G., 1996. Influence of mechanical stratigraphy on folding vs faulting. Journal of Structural Geology 18, 443–450.

Escher, A., Masson, H., Steck, A., 1993. Nappe geometry in the western Swiss Alps. Journal of structural Geology 15, 501–509.

Ferrill, D.A., Morris, A.P., Jones, S.M., Stamatakos, J.A., 1998. Extensional layer-parallel shear and normal faulting. Journal of Structural Geology 20, 355–362.

Ferrill, D.A., Morris, A.P., McGinnis, R.N., Smart, K.J., Wigginton, S.S., Hill, N.J., 2017. Mechanical stratigraphy and normal faulting. Journal of Structural Geology 94, 275–302.

Ferziger, J.H., Perić, M., 2002. Computational methods for fluid dynamics. volume 3. Springer.

Froitzheim, N., Eberli, G.P., 1990. Extensional detachment faulting in the evolution of a Tethys passive continental margin, Eastern Alps, Switzerland. Geological society of America bulletin 102, 1297–1308.

Fry, N., 1979. Random point distributions and strain measurement in rocks. Tectonophysics 60, 89–105.

Gerya, T.V., Yuen, D.A., 2003. Characteristics-based marker-in-cell method with conservative finite-differences schemes for modeling geological flows with strongly variable transport properties. Physics of the Earth and Planetary Interiors 140, 293–318.

Gillcrist, R., Coward, M., Mugnier, J.L., 1987. Structural inversion and its controls: examples from the Alpine foreland and the French Alps. Geodinamica acta 1, 5–34.

Granado, P., Ruh, J.B., 2019. Numerical modelling of inversion tectonics in fold-and-thrust belts. Tectonophysics 763, 14–29.

Gurtin, M.E., 1982. An introduction to continuum mechanics. volume 158. Academic press.

Hamilton, W.B., 1988. Laramide crustal shortening. Interaction of the Rocky Mountain foreland and the Cordilleran thrust belt: Geological Society of America Memoir 171, 27–39.

Harlow, F.H., Welch, J.E., 1965. Numerical calculation of time-dependent viscous incompressible flow of fluid with free surface. The physics of fluids 8, 2182–2189.

Heim, A., 1922. Geologie der Schweiz. volume 2. CH Tauchnitz.

Helwig, J., 1976. Shortening of continental crust in orogenic belts and plate tectonics. Nature 260, 768.

Herwegh, M., Pfiffner, O.A., 2005. Tectono-metamorphic evolution of a nappe stack: A case study of the Swiss Alps. Tectonophysics 404, 55–76.

Hossack, J.R., 1968. Pebble deformation and thrusting in the Bygdin area (southern Norway). Tectonophysics 5, 315–339.

Hossack, J.R., 1979. The use of balanced cross-sections in the calculation of orogenic contraction: A review. Journal of the Geological Society 136, 705–711.

Hsu, T., 1966. The characteristics of coaxial and non-coaxial strain paths. Journal of Strain Analysis 1, 216–222.

King Hubbert, M., Rubey, W.W., 1959. Role of fluid pressure in mechanics of overthrust faulting: I. Mechanics of fluid-filled porous solids and its application to overthrust faulting. Geological Society of America Bulletin 70, 115–166.

Jackson, J., 1980. Reactivation of basement faults and crustal shortening in orogenic belts. Nature 283, 343.

Jaquet, Y., Bauville, A., Schmalholz, S.M., 2014. Viscous overthrusting versus folding: 2-D quantitative modeling and its application to the Helvetic and Jura fold and thrust belts. Journal of Structural Geology 62, 25–37.

Groshong Jr, R.H., Pfiffner, O.A., Pringle, L.R., 1984. Strain partitioning in the Helvetic thrust belt of eastern Switzerland from the leading edge to the internal zone. Journal of Structural Geology 6, 5–18.

Karato, S.i., 2012. Deformation of earth materials: an introduction to the rheology of solid earth. Cambridge University Press.

Kaus, B., Popov, A.A., Baumann, T., Pusok, A., Bauville, A., Fernandez, N., Collignon, M., 2016. Forward and inverse modelling of lithospheric deformation on geological timescales, in: Proceedings of NIC Symposium.

Kaus, B.J., Mühlhaus, H., May, D.A., 2010. A stabilization algorithm for geodynamic numerical simulations with a free surface. Physics of the Earth and Planetary Interiors 181, 12–20.

Kirschner, D., Masson, H., Sharp, Z., 1999. Fluid migration through thrust faults in the Helvetic nappes (Western Swiss Alps). Contributions to Mineralogy and Petrology 136, 169–183.

Kirschner, D.L., Cosca, M.A., Masson, H., Hunziker, J.C., 1996. Staircase 40/Ar39Ar spectra of fine-grained white mica: Timing and duration of deformation and empirical constraints on argon diffusion. Geology 24, 747–750.

Lacombe, O., Bellahsen, N., 2016. Thick-skinned tectonics and basement-involved fold–thrust belts: insights from selected Cenozoic orogens. Geological Magazine 153, 763–810.

Lacombe, O., Lavé, J., Roure, F.M., Vergés, J., 2007. Thrust belts and foreland basins: From fold kinematics to hydrocarbon systems. Springer Science & Business Media.

Lacombe, O., Mouthereau, F., 2002. Basement-involved shortening and deep detachment tectonics in forelands of orogens: Insights from recent collision belts (Taiwan, Western Alps, Pyrenees). Tectonics 21, 12–1.

Lagabrielle, Y., Cannat, M., 1990. Alpine Jurassic ophiolites resemble the modern central Atlantic basement. Geology 18, 319–322.

Laubach, S.E., Olson, J.E., Gross, M.R., 2009. Mechanical and fracture stratigraphy. AAPG bulletin 93, 1413–1426.

Leloup, P.H., Arnaud, N., Sobel, E.R., Lacassin, R., 2005. Alpine thermal and structural evolution of the highest external crystalline massif: The Mont Blanc. Tectonics 24.

Lemoine, M., Bas, T., Arnaud Vanneau, A., Arnaud, H., Dumont, T., Gidon, M., Bourbon, M., de Graciansky, P.C., Rudkiewicz, J.L., Megard Galli, J., et al., 1986. The continental margin of the Mesozoic Tethys in the Western Alps. Marine and petroleum geology 3, 179–199.

Liou, J., Ernst, W., Zhang, R., Tsujimori, T., Jahn, B., 2009. Ultrahigh-pressure minerals and metamorphic terranes–the view from China. Journal of Asian Earth Sciences 35, 199–231.

Lister, G., Etheridge, M., Symonds, P., 1986. Detachment faulting and the evolution of passive continental margins. Geology 14, 246–250.

Lode, W., 1926. Versuche über den Einfluß der mittleren Hauptspannung auf das Fließen der Metalle Eisen, Kupfer und Nickel. Zeitschrift für Physik 36, 913–939.

Macqueen, R.W., Leckie, D.A., 1992. Foreland basins and fold belts .

Manzotti, P., Ballevre, M., Zucali, M., Robyr, M., Engi, M., 2014. The tectonometamorphic evolution of the Sesia–Dent Blanche nappes (internal Western Alps): review and synthesis. Swiss Journal of Geosciences 107, 309–336.

Mase, G.E., 1970. Continuum mechanics. volume 970. McGraw-Hill New York.

Masson, H., Baud, A., Escher, A., Gabus, J., Marthaler, M., 1980. Paléokarsts crétacés et tertiaires dans la nappe de Morcles. Compte rendu de lâĂŹexcursion de la Société géologique Suisse du 1, 331–349.

Masson, H., Bussy, F., Eichenberger, M., Giroud, N., Meilhac, C., Presniakov, S., 2008. Early Carboniferous age of the Versoyen ophiolites and consequences: non-existence of a 'Valais ocean'(Lower Penninic, western Alps). Bulletin de la Société géologique de France 179, 337–355.

Mazzotti, A.P., Stucchi, E., Fradelizio, G.L., Zanzi, L., Scandone, P., 2000. Seismic exploration in complex terrains: a processing experience in the Southern Apennines. Geophysics 65, 1402–1417.

McClay, K., 1992. Glossary of thrust tectonics terms. Thrust tectonics , 419–433.

Merle, O., 1989. Strain models within spreading nappes. Tectonophysics 165, 57–71.

Merle, O., 1998. Emplacement mechanisms of nappes and thrust sheets. volume 9. Springer Science & Business Media.

Milnes, A.G., Pfiffner, O.A., 1977. Structural development of the Infrahelvetic complex, eastern Switzerland. Eclogae Geologicae Helvetiae 70, 83–95.

Mirabella, F., Barchi, M.R., Lupattelli, A., 2008. Seismic reflection data in the Umbria Marche Region: limits and capabilities to unravel the subsurface structure in a seismically active area. Annals of Geophysics 51.

Mitra, S., Fisher, G.W., 1992. Structural geology of fold and thrust belts. Johns Hopkins University Press.

Mitra, S., Namson, J.S., 1989. Equal-area balancing. American Journal of Science 289, 563–599.

Molinaro, M., Leturmy, P., Guezou, J.C., Frizon de Lamotte, D., Eshraghi, S., 2005. The structure and kinematics of the southeastern Zagros fold-thrust belt, Iran: From thin-skinned to thick-skinned tectonics. Tectonics 24.

Mouthereau, F., Deffontaines, B., Lacombe, O., Angelier, J., Byrne, T., Liu, C., 2002. Variations along the strike of the Taiwan thrust belt: Basement control on structural style, wedge geometry, and kinematics. Sspecial Papers-Geological Society of Aamerica , 31–54.

Müller, I., Müller, W.H., 2009. Fundamentals of thermodynamics and applications: with historical annotations and many citations from Avogadro to Zermelo. Springer Science & Business Media.

Nádai, A., Hodge, P., 1963. Theory of Flow and Fracture of Solids, vol. II. Journal of Applied Mechanics 30, 640.

Nemčok, M., Mora, A., Cosgrove, J., 2013. Thick-skin-dominated orogens; from initial inversion to full accretion: an introduction. Geological Society, London, Special Publications 377, 1–17.

Nemcok, M., Schamel, S., Gayer, R., 2009. Thrustbelts: Structural architecture, thermal regimes and petroleum systems. Cambridge University Press.

Pfiffner, O., 1981. Fold-and-thrust tectonics in the Helvetic Nappes (E Switzerland). Geological Society, London, Special Publications 9, 319–327.

Pfiffner, O.A., 1993. The structure of the Helvetic nappes and its relation to the mechanical stratigraphy. Journal of structural Geology 15, 511–521.

Pfiffner, O.A., 2006. Thick-skinned and thin-skinned styles of continental contraction. Sspecial Papers-Geological Society of Aamerica 414, 153.

Pfiffner, O.A., 2015. Geologie der Alpen. volume 8416. UTB.

Pfiffner, O.A., Burkhard, M., Hänni, R., Kammer, A., Kligfield, R., Mancktelow, N., Menkveld, J., Ramsay, J., Schmid, S., Zurbriggen, R., 2011. Structural map of the Helvetic zone of the Swiss Alps, including Vorarlberg (Austria) and Haute Savoie (France) .

Poblet, J., Lisle, R.J., 2011. Kinematic evolution and structural styles of fold-and-thrust belts. Geological Society, London, Special Publications 349, 1–24.

Poirier, J., 1980. Shear localization and shear instability in materials in the ductile field. Journal of Structural Geology 2, 135–142.

Poulet, T., Veveakis, M., Herwegh, M., Buckingham, T., Regenauer Lieb, K., 2014. Modeling episodic fluid-release events in the ductile carbonates of the Glarus thrust. Geophysical Research Letters 41, 7121–7128.

Price, N.J., McClay, K.R., 1981. Thrust and nappe tectonics, Geological Society of London.

Price, R.A., 1988. The mechanical paradox of large overthrusts. Geological Society of America Bulletin 100, 1898–1908.

Ragan, D.M., 2009. Structural geology: an introduction to geometrical techniques. Cambridge University Press.

Ramsay, J., 1981. Tectonics of the Helvetic nappes. Geological Society, London, Special Publications 9, 293–309.

Ramsay, J.G., 1967. Folding and fracturing of rocks. Mc Graw Hill Book Company 568.

Ramsay, J.G., Casey, M., Kligfield, R., 1983. Role of shear in development of the Helvetic fold-thrust belt of Switzerland. Geology 11, 439–442.

Ramsay, J.G., Huber, M.I., 1987. The techniques of modern structural geology: Folds and fractures. volume 2. Academic press.

Ranalli, G., 1995. Rheology of the Earth. Springer Science & Business Media.

Ranero, C.R., Pérez Gussinyé, M., 2010. Sequential faulting explains the asymmetry and extension discrepancy of conjugate margins. Nature 468, 294.

Rebay, G., Spalla, M., Zanoni, D., 2012. Interaction of deformation and metamorphism during subduction and exhumation of hydrated oceanic mantle: Insights from the Western Alps. Journal of Metamorphic Geology 30, 687–702.

Rodgers, J., 1949. Evolution of thought on structure of middle and southern Appalachians. AAPG Bulletin 33, 1643–1654.

Rubey, W.W., King Hubbert, M., 1959. Role of fluid pressure in mechanics of overthrust faulting: II. Overthrust belt in geosynclinal area of western Wyoming in light of fluid-pressure hypothesis. Geological Society of America Bulletin 70, 167–206.

Ruh, J.B., Gerya, T., Burg, J.P., 2014. 3D effects of strain vs. velocity weakening on deformation patterns in accretionary wedges. Tectonophysics 615, 122–141.

Schmid, S.M., 1975. The Glarus overthrust: Field evidence and mechanical model. Ecologae Geol. Helvetia 68, 247–280.

Schmid, S.M., Fügenschuh, B., Kissling, E., Schuster, R., 2004. Tectonic map and overall architecture of the Alpine orogen. Eclogae Geologicae Helvetiae 97, 93–117.

Smoluchowski, M., 1909. II - Some Remarks on the Mechanics of Overthrusts. Geological Magazine 6, 204–205.

Stampfli, G., Borel, G.D., Marchant, R., Mosar, J., 2002. Western Alps geological constraints on western Tethyan reconstructions. Journal of the Virtual Explorer 8, 77.

Steck, A., 1999. Carte tectonique des Alpes de Suisse occidentale et des régions avoisinantes. Office fédéral des eaux et de la géologie.

Steinmann, M., Stille, P., 1999. Geochemical evidence for the nature of the crust beneath the eastern North Penninic basin of the Mesozoic Tethys ocean. Geologische Rundschau 87, 633–643.

Suppe, J., 1983. Geometry and kinematics of fault-bend folding. American Journal of science 283, 684–721.

Suppe, J., 1985. Principles of structural geology. Prentice Hall.

Tavarnelli, E., Butler, R., Decandia, F., Calamita, F., Grasso, M., Alvarez, W., Renda, P., Crescenti, U., Dóffizi, S., 2004. Implications of fault reactivation and structural inheritance in the Cenozoic tectonic evolution of Italy. The Geology of Italy, Special 1, 209–222.

Termier, P., 1906. La synthèse géologique des Alpes.

Termier, P., 1922. A la glorie de la terre: souvenirs d'un geologue .

Tricart, P., Lemoine, M., 1986. From faulted blocks to megamullions and megaboudins: Tethyan heritage in the structure of the Western Alps. Tectonics 5, 95–118.

Trümpy, R., Aubert, D., Bernoulli, D., 1980. Geology of Switzerland: Geological excursions. volume 10. Wepf.

Watts, A., Lamb, S., Fairhead, J., Dewey, J., 1995. Lithospheric flexure and bending of the Central Andes. Earth and Planetary Science Letters 134, 9–21.

Welbon, A., Butler, R., 1992. Structural styles in thrust belts developed through rift basins: a view from the western Alps, in: Structural and tectonic modelling and its application to petroleum geology. Elsevier, pp. 469–479.

Wiltschko, D., Chapple, W., 1977. Flow of weak rocks in Appalachian Plateau folds. AAPG Bulletin 61, 653–670.

Wissing, S., Pfiffner, O.A., 2003. Numerical models for the control of inherited basin geometries on structures and emplacement of the Klippen nappe (Swiss Prealps). Journal of structural geology 25, 1213–1227.

Zerlauth, M., Ortner, H., Pomella, H., Pfiffner, O.A., Fügenschuh, B., 2014. Inherited tectonic structures controlling the deformation style: an example from the Helvetic nappes of the Eastern Alps. Swiss Journal of Geosciences 107, 157–175.

CHAPTER 2

Quantification and visualization of finite strain in 3D viscous numerical models of folding and overthrusting

Richard Spitz[1,2], Stefan M. Schmalhoz[1,2], Boris J.P. Kaus[3], and Anton A. Popov[3]

[1]Faculté des géosciences et de l'environnement, Institut des Sciences de la Terre, University of Lausanne, Lausanne, Switzerland.

[2]Swiss Geocomputing Centre, University of Lausanne, Lausanne, Switzerland.

[3]Institute of Geosciences, Johannes-Gutenberg University, Mainz, Germany.

Journal of Structural Geology, 27 November 2019

Abstract

Finite strain analysis and three-dimensional (3D) numerical modelling are important methods to understand the deformation history of rocks. Here, we analyze finite strain in 3D numerical simulations of power-law viscous folding and overthrusting. Simulations with different and laterally varying detachment geometries cause a lateral transition from folding (for thicker detachments) to overthrusting. We compute the 3D finite strain tensor, the principal strain values and their orientations. We compute the Nádai strain, ε_S, and the Lode's ratio, ν, representing the strain symmetry (constriction or flattening). We apply Hsu diagrams to visualize strain distribution in ε_S - ν space, in combination with color-coding, indicating the corresponding position of strain data in the 3D model. We analyze the orientation and spatial variation of finite strain with polar and rose diagrams and quantify the spatial and temporal evolution of finite strain with strain profiles. Our results show that: (i) the magnitude of ε_S generally increases from folding to overthrusting, (ii) an initial flat ramp geometry of the detachment generates a distinctive pattern of ε_S, (iii) lateral variations of ε_S and ν can be used to identify lateral variations in sub-surface structures, and (v) internal strike-slip shearing is generated due to the folding-overthrusting transition.

Finite strain analysis in deformed rocks is one of the major objectives and essential tools in structural geology (e.g Ramsay, 1967; Ramsay and Huber, 1987; Pollard et al., 2005). The fundamental reason being that the quantification of finite strain is an irreplaceable method to understand the structural history and the deformational behavior of rocks (Ramsay, 1967). Finite strain can be estimated in many deformed rocks and uncertainties in finite strain estimates are likely considerably smaller than uncertainties in estimates of strain rate or stress. Moreover, finite strain analysis of geological structures such as folds, thrusts, shear zones, foliations and lineations is useful to determine the kinematic and dynamic conditions during the development of these structures on all geological scales. For example, the gradient of finite strain across a ductile shear zone can be related to the temperature gradient across the shear zone and the flow law parameters of the sheared rock (Bauville and Schmalholz, 2013; Bauville et al., 2013). Therefore, finite strain analysis enables assessing the thermo-mechanical process that was active during the deformation of rock units. Further applications of finite strain analysis include the fundamental understanding of the development of rock fabrics and foliations (Ramsay and Wood, 1973; Tullis and Wood, 1975), the correlation with magnetic fabrics in studies of anisotropic magnetic susceptibility (e.g. Kligfield et al., 1981; Borradaile and Henry, 1997; Burmeister et al., 2009; McCarthy et al., 2015), cross-sectional reconstruction (e.g. Woodward et al., 1986; Mitra, 1994) and the interpretation of spatial changes in strain regarding the temporal evolution (e.g. Ramsay, 1967; Means et al., 1980; Fossen and Tikoff, 1993). Consequently, there exists many studies focusing on strain analysis (Lisle et al., 2019) and for a recent review of the history of finite strain analysis we refer to McCarthy et al. (2019).

Strain can only be completely described in three dimensions (3D). Nevertheless, it is common to assume a plane strain deformation when analyzing strained geological materials (e.g. Twiss and Moores, 1992; Mookerjee and Mitra, 2009). However, a 3D finite strain analysis is essential for geological systems in which stratigraphy, basement structure and the associated structural style varies laterally along strike.(e.g. Laubscher, 1972; Merschat et al., 2005). Numerous studies of fold and thrust belts suggest that the development of different structural styles along orogens is controlled by distinctive lateral structural variations associated with tectonic inheritances (e.g. Laubscher, 1972; Ries, 1976; Beutner, 1977; Marshak et al., 1992; Marshak and Flöttmann, 1996; Mitra, 1997). Tectonic inheritances include, for example, variable depth of basins along strike or the lateral variation of detachment horizon thickness and strength (e.g. Macedo and Marshak, 1999; Von Tscharner et al., 2016). For example, such observations have been made in the Swiss Alps where studies link the deformation style to lateral variations of basement structures and stratigraphy (e.g. Pfiffner, 1993; Butler et al., 2006; Zerlauth et al., 2014; Bauville and Schmalholz, 2017). The quantification of finite strain and its spatial gradients can provide, for example, important information on the sub-surface basement geometry or the existence of sub-surface ramps or graben structures (e.g. Boutoux

et al., 2014). The significance of three dimensional geometry on the evolving finite strain is also supported by sandbox and numerical modeling (e.g. Gairola, 1977; Macedo and Marshak, 1999; Von Tscharner et al., 2016; Zwaan et al., 2016).

Many methods of strain analysis (e.g. Shimamoto and Ikeda, 1976; Fry, 1979; Mulchrone, 2003) could be naturally adapted to 3D but there are few finite strain studies focusing on the 3D deformation history (Tikoff and Fossen, 1999). In fact, the lack of suitable 3D data sets to perform a complete 3D finite strain analysis is a long lasting problem (e.g McCarthy et al., 2019). However, recent advances in, for example, tomography point to a feasible acquisition of such 3D data sets in the future (e.g. Adam et al., 2013; Robin and Charles, 2015; Zwaan et al., 2016). Additionally, a growing number of studies recognizes the utilization of 3D finite strain analysis as an essential approach to understand the kinematic evolution of geological structures (e.g. Fossen and Cavalcante, 2017; Fossen et al., 2018; Díaz Azpiroz et al., 2018). Because of the importance of 3D finite strain analysis for structural geology, we focus here on the quantification and visualization of finite strain and its gradients in 3D numerical models of power-law viscous flow applied to folding and overthrust shearing, referred to here as overthrusting. We use the open source 3D numerical code LaMEM for our simulations (Kaus et al., 2016). We perform simulations of the lateral transition from folding to overthrusting, whereby the transition is controlled by laterally varying the thickness and geometry of a weak detachment horizon. We base our 3D model configurations on a previous 2D numerical study by Jaquet et al. (2014) who show that the detachment thickness controls whether a mechanically competent viscous rock unit deforms dominantly by folding or overthrusting. Jaquet et al. (2014) show that a pre-existing weak zone in the competent layer can either be activated as shear zone and cause overthrusting or remain essentially undeformed and allow folding of the competent layer. We calculate the 3D finite strain tensor from the numerical strain field. In order to analyze the finite strain, we calculate various quantities, such as the Lode's ratio ν (Lode, 1926) and Nádai strain ϵ_s (Nádai and Hodge, 1963). Furthermore, we apply different visualization methods such as the Hsu diagram (Hsu, 1966; Hossack, 1968) or polar and rose diagrams. The main aims of this study are (i) to investigate the lateral transition from folding to overthrusting in 3D numerical models of viscous flow and (ii) to present and discuss various methods of 3D finite strain quantification and visualization for numerical simulations. We also provide two Matlab scripts, as supplementary material, that contain the calculation and visualization of finite strain for homogeneous 2D simple shear and 3D pure shear.

2.1 Model and finite strain calculation

2.1.1 Model configuration

Our 3D model configurations are created with the open source software package geomIO (Bauville and Baumann, 2019, `https://geomio.bitbucket.io/`) which can be used in combination with the LaMEM code. The configurations consist of an incompressible weak viscous matrix that surrounds an incompressible strong viscous layer (Figure 2.1). The strong layer mimics competent carbonate or sandstone units and has an initial viscosity of $\mu_L = 10^{22}$ $Pa \cdot s$ and a power-law stress exponent of n = 3. The matrix represents incompetent shale- or evaporate-rich units and has an initial viscosity of $\mu_M = 10^{20}$ $Pa \cdot s$ and a power-law stress exponent of n = 3. The above effective viscosity values are given for the applied homogeneous bulk deformation and effective viscosities can vary if the strain rate deviates form the reference strain rate associated with homogeneous bulk deformation (see next section). Both phases have a constant density of $\rho = 2500\ kg/m^3$. The matrix below the strong layer constitutes a detachment horizon whose thickness varies laterally in the X-direction (orthogonal to shortening direction; Figure 2.1). The model domain has width of $L_X = 50$ km, a length of $L_Y = 50$ km and a height of $L_Z = 10$ km with 1 km of sticky air ($\mu_{air} = 10^{19}$ $Pa \cdot s$) in the top region to mimic a free surface.

The initial thickness of the strong layer is constant with $H_L = 1$ km. In contrast, we variably decrease the detachment horizon thickness from $H_M = 1$ km at X = 50 km to $H_M = 0.125$ km at X = 0 km. To localize the deformation we prescribe a weak and oblique zone at Y = 25 km in the middle of the layer; following the 2D model configuration of Jaquet et al. (2014). The weak zone has the same rheology as the surrounding matrix ($\mu_M = 10^{20}$ $Pa \cdot s$, power-law stress exponent n = 3) and an initial thickness of 350 m (Figure 2.1g). Each configuration contains two passive marker layers that we use to analyze the finite strain. In the next section we will use the ratio H_M/H_L to refer to any changes of detachment horizon thickness.

In total we employ six different model configurations (Figure 2.1) to examine the effect of the spatial distribution of H_M/H_L and the obliqueness of the weak zone: In configuration A (Figure 2.1a) we decrease H_M/H_L from 1.0 to 0.125 in the lateral X-direction over X = 0 to 50 km (Figure 2.1h). Configuration B and Br (Figure 2.1b,c) employ the same H_M/H_L distribution as configuration A (Figure 2.1h), but have an oblique weak zone. The angle of the weak zone starting from X = 0 km is 15° for B and -15° for Br. Configuration C (Figure 2.1d,i) has a H_M/H_L increase over a shorter distance, creating a flat ramp geometry (Figure 2.1l). Here, H_M/H_L is constant with a value of 1.0 from X = 0 to 20 km and is then decreased linearly to $H_M/H_L = 0.125$ over the distance X = 20 to 30 km, from where it is constant again to X = 50 km. Similarly, configuration D and Dr (Figure 2.1e,f) use the same H_M/H_L

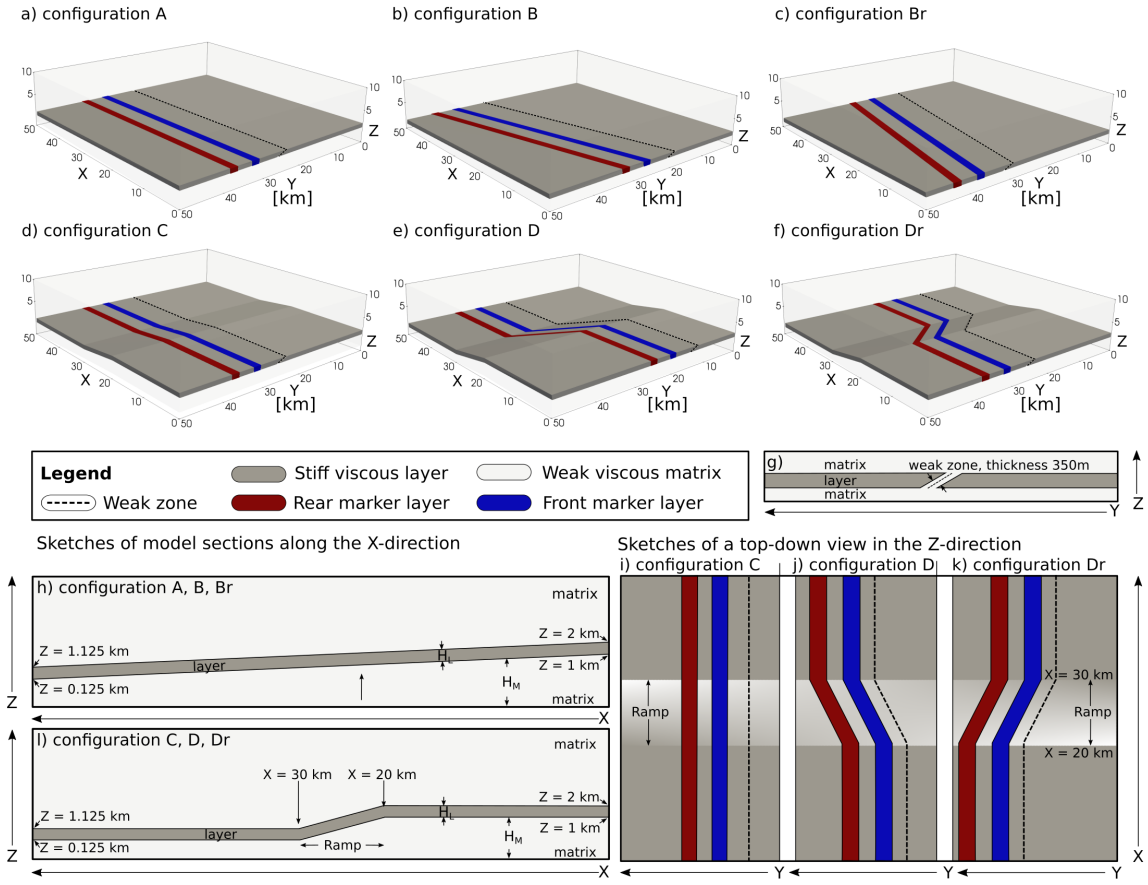

Figure 2.1: Display of our six initial model configurations. In red and blue: passive marker layers that are used to track and display parameters for the finite strain evolution. a) to f) 3D view of our model configurations. g) Sketch (not to scale) of a zoom-in around the pre-existing weak zone (same material properties as the matrix) with view in the X-direction. h) Sketch (not to scale) of a model section along the X-direction for configurations A, B, Br displaying the variability of H_M/H_L in the X-direction. l) Sketch (not to scale) of a model section along the X-direction for configurations C, D, Dr displaying the variability of H_M/H_L in the X-direction using a flat ramp. i) to k) Sketches (not to scale) of a top-down view in the Z-direction to indicate the geometry of the weak zone and marker layers in the X-direction for configuration C, D and Dr. The marker layers are initially parallel to the weak zone. In configuration D and Dr the weak zone has an oblique angle across the ramp. The ramp goes downward in the positive X-direction.

distribution as configuration C (Figure 2.1l). Here, for both configurations the weak zone is oblique with an angle of 60° and -60° across the flat ramp geometry (Figure 2.1j,k).

2.1.2 Mathematical Model

We solve for the conservation of mass and momentum for incompressible, slow viscous flow under gravity using the equations:

$$\frac{\partial v_i}{\partial x_i} = 0 \tag{2.1}$$

$$-\frac{\partial P}{\partial x_i} + \frac{\partial \tau_{ij}}{\partial x_j} = \rho g_i \tag{2.2}$$

where x_i(i = 1,2,3) refers to Cartesian coordinates in the three spatial directions, v_i are the components of the velocity vector, P is pressure (negative mean stress), $\tau_{ij} = \sigma_{ij} + P\delta_{ij}$ are components of the deviatoric Cauchy stress tensor, ρ is density and g_i the gravity acceleration vector. We use a purely mechanical model without temperature evolution. The components of the deviatoric strain rate tensor are defined by the viscous constitutive equation:

$$\dot{\epsilon}_{ij} = \frac{1}{2\eta_{eff}}\tau_{ij} \tag{2.3}$$

Where η_{eff} is the effective viscosity that depends on the power-law exponent n, the initial reference viscosity η_0 and the square root of the second invariant of the strain rate tensor $\dot{\epsilon}_{II} = (\frac{1}{2}\dot{\epsilon}_{ij}\dot{\epsilon}_{ij})^{\frac{1}{2}}$. The strain rate invariant, $\dot{\epsilon}_{II}$, is normalized by the square root of the second invariant of the reference strain rate tensor $\dot{\epsilon}^r_{II}$:

$$\eta_{eff} = \eta_0 \left(\frac{\dot{\epsilon}_{II}}{\dot{\epsilon}^r_{II}}\right)^{(1-\frac{1}{n})} \tag{2.4}$$

The value of $\dot{\epsilon}^r_{II}$ corresponds to homogeneous deformation for the applied pure shear shortening configuration, without a layer, so that η_0 is the constant effective viscosity of the model fluid since $\dot{\epsilon}_{II}/\dot{\epsilon}^r_{II} = 1$ for homogeneous pure shear. Deviations of η_{eff} from η_0 are, hence, caused by deviations of the strain rates from the homogeneous strain rate, which take place during deformation with a strong layer.

We mimic a free surface boundary condition on the top using a so-called sticky air layer. For all model sides, including the bottom, we apply a free slip boundary condition. The free slip boundary condition at the base is used to model a perfect décollement horizon below the strong layer. We induce bulk shortening of the model in the Y-direction by applying a velocity boundary condition. For every time step the velocity is recalculated in such a way that the bulk shortening strain rate is constant at $\dot{\epsilon}_{bg} = 10^{-15}\frac{1}{s}$. The shortening of the model in the

Y-direction is balanced by an elongation in the Z-direction, while the width in the X-direction does not change.

We conduct our simulations with the 3D numerical parallel code LaMEM that uses staggered grid finite difference discretization. Material properties are advected employing a marker-and-cell method. A detailed overview of LaMEM can be found in Kaus et al. (2016) and in the documentation on the official website (`https://bitbucket.org/bkaus/lamem`).

2.1.3 Finite Strain Calculation and Visualization

In 3D space the undeformed state of an object can be represented by a unit sphere. During a homogeneous deformation the sphere changes to an ellipsoid that can be described by three principal semi-axes. Any final state after a deformation can therefore be represented by a finite strain ellipsoid. Such a finite strain ellipsoid is defined by the magnitude and orientation of the three principal strains, which can be obtained from the finite strain tensor. In our numerical approach we compute the finite strain tensor from the finite deformation gradient tensor $\boldsymbol{F}$ following a standard continuum mechanics approach. (e.g. Bower, 2009; Ragan, 2009). In order to trace the evolution of finite strain we accumulate and store $\boldsymbol{F}$ on our numerical markers. To obtain the finite deformation gradient tensor we first compute the components of the incremental deformation gradient tensor $\boldsymbol{\Delta F}$ for every time step from the velocity field in the following manner:

$$\boldsymbol{\Delta F} = \boldsymbol{I} + \frac{\partial \boldsymbol{v}}{\partial \boldsymbol{x}} \Delta t, \tag{2.5}$$

where $\boldsymbol{I}$ is the second order identity tensor, $\boldsymbol{v}$ the velocity vector, $\boldsymbol{x}$ the spatial coordinate vector, and Δt the time step. The second term of equation (5) is also called the displacement gradient tensor and is an approximation derived from a Taylor series expansion, where the higher order terms are dropped. Next follows the successive update of the deformation gradient tensor $\boldsymbol{F}$ which is analogous to the cumulative coordinate mapping. If we consider a coordinate map $\boldsymbol{x} = \boldsymbol{x}(\boldsymbol{X}, t)$, where the current coordinates $\boldsymbol{x}$ are a function of the original coordinates $\boldsymbol{X}$ and time, we can use the chain rule on a time step:

$$\frac{\partial \boldsymbol{x}_{n+1}}{\partial \boldsymbol{X}} = \frac{\partial \boldsymbol{x}_{n+1}}{\partial \boldsymbol{x}_n} \frac{\partial \boldsymbol{x}_n}{\partial \boldsymbol{X}} \tag{2.6}$$

Following from equation (6), the deformation gradient tensor $\boldsymbol{F}$ is updated from the previous time step in a multiplicative manner:

$$\boldsymbol{F}_{n+1} = \boldsymbol{\Delta F}\, \boldsymbol{F}_n, \tag{2.7}$$

where $\boldsymbol{F}_n$ and $\boldsymbol{F}_{n+1}$ are the deformation gradients in the beginning and in the end of a time step, respectively. We proceed with the polar decomposition of the deformation gradient:

$$\boldsymbol{F} = \boldsymbol{V}\,\boldsymbol{R}, \tag{2.8}$$

where $\boldsymbol{R}$ is an orthogonal tensor representing rigid body rotation, and $\boldsymbol{V}$ is a symmetric positive definite tensor representing finite strain in the current configuration, which is called the left stretch tensor. The polar decomposition can be performed by computing the spectral representation of the left Cauchy-Green deformation tensor $\boldsymbol{B}$ as follows:

$$\boldsymbol{B} = \boldsymbol{F}\boldsymbol{F}^T = \boldsymbol{V}^2 = \sum_{i=1}^{3} \lambda_i^2\, \boldsymbol{n}_i \otimes \boldsymbol{n}_i \tag{2.9}$$

Here, λ_i and $\boldsymbol{n}_i$, respectively, are the eigenvalues and the eigenvectors of the left stretch tensor $\boldsymbol{V}$. The eigenvalues represent principal strains, and the eigenvectors represent the directions of the principal strain axes. Both quantities are required to visualize the finite strain ellipsoid. To illustrate the finite strain computation in detail, we provide a Matlab script in the supplementary material which presents the calculation of the finite strain ellipse and ellipsoid for 2D and 3D homogeneous shear, respectively.

In order to quantify and visualize the finite strain tensor we compute and plot the strain magnitude and the strain symmetry from the finite strain tensor. The strain magnitude or strain intensity can be expressed by the octahedral shear strain ε_s (Nádai and Hodge, 1963), also called Nádai strain. It provides a non-dimensional measure on the amount of strain that was applied during a homogeneous deformation. The second parameter is the Lode's ratio ν (Lode, 1926) and describes the strain symmetry, the shape of the ellipsoid. The Lode's ratio ν is restricted to values between -1.0 and 1.0. For the interval $-1.0 \leqslant \nu < 0$ the ellipsoid is general prolate, for $0 < \nu \leqslant 1.0$ oblate and $\nu = 0$ represents the boundary between an oblate-prolate ellipsoid. Besides the geometrical description ν also infers the deformation style: prolate ellipsoids imply a constrictional, oblate-prolate ellipsoids a plane strain, and oblate ellipsoids a flattening deformation regime. Both parameters are calculated from the natural strains $\varepsilon_{1,2,3} = \ln \lambda_{1,2,3}$ in the following manner:

$$\varepsilon_s = \frac{1}{\sqrt{3}} \sqrt{(\varepsilon_1 - \varepsilon_2)^2 + (\varepsilon_2 - \varepsilon_3)^2 + (\varepsilon_3 - \varepsilon_1)^2} \tag{2.10}$$

$$\nu = \frac{2\varepsilon_2 - \varepsilon_1 - \varepsilon_3}{\varepsilon_1 - \varepsilon_3} \tag{2.11}$$

The parameters ε_s and ν can be correlated with each other inside a Hsu diagram (Hsu, 1966; Hossack, 1968). This diagram consists of a 60 degree section of a polar diagram, where

the radial contours represent the ε_s values and the angular contours represent the ν values. Thus the Hsu diagram provides a graphical representation of finite strain that relates strain

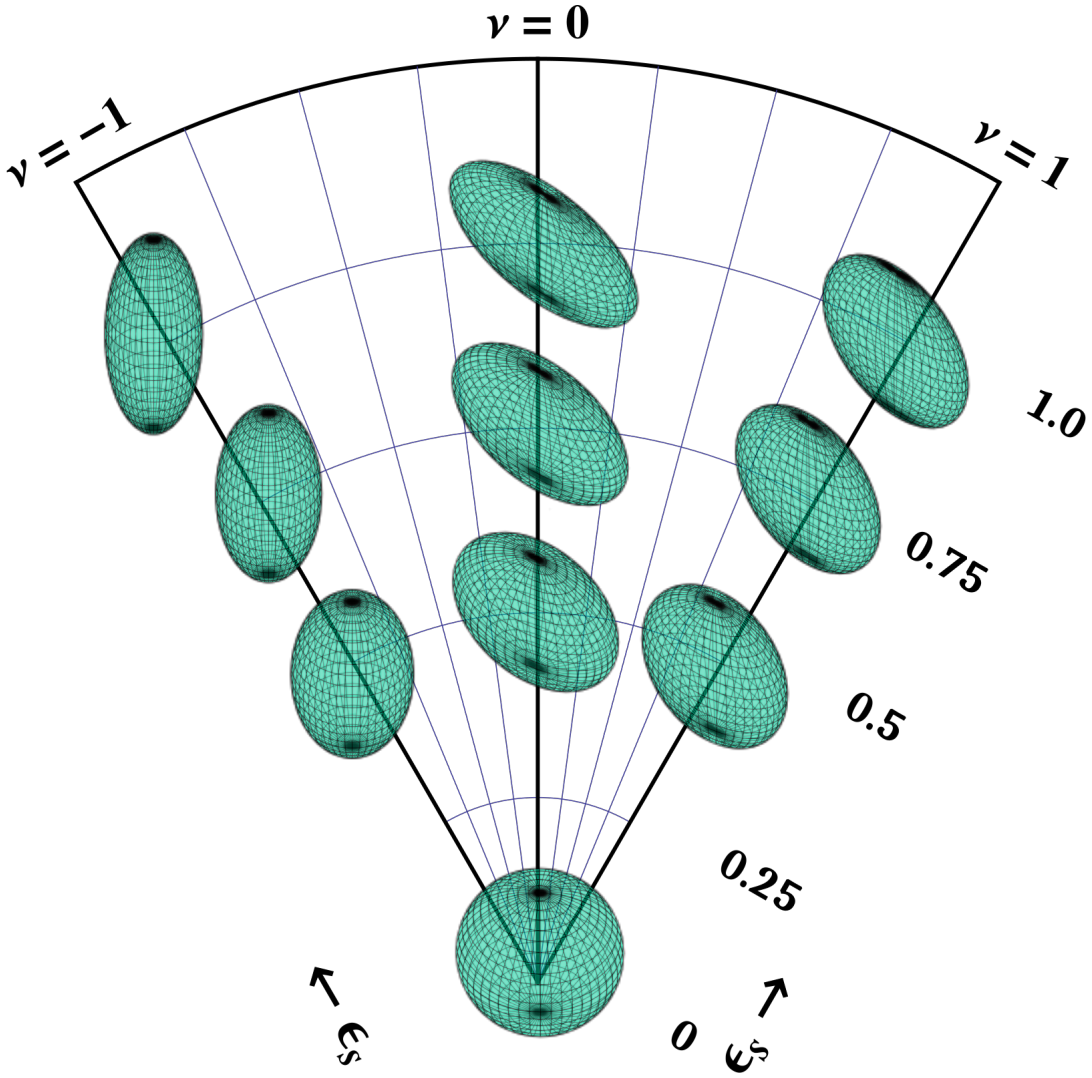

Figure 2.2: Example of a typical Hsu diagram, displaying the evolution of a sphere during ongoing deformation for different ε_s (radial contours) and ν values (angular contours).

magnitude to strain symmetry and aids in the identification of different deformation regimes (Figure 2.2). The strain magnitude-symmetry relation could also be displayed with the more commonly used Flinn-diagram (Flinn, 1962). However in a recent review of the Hsu and Flinn diagram Mookerjee and Peek (2014) conclude that the spatial distribution of the Flinn-diagram might obscure subtle kinematic patterns due to visual distortion. Hence, Mookerjee and Peek (2014) suggest that the Hsu diagram may be more useful to statistical treatments of three-dimensional data sets. In addition, we also calculate the orientation of finite strain major axis

which is given by the azimuth and inclination relative to the XY-plane. For example, Figure 2.3 displays the finite strain major axis orientation for our marker layers using a color-coded inclination on top of the directional vectors of the azimuth.

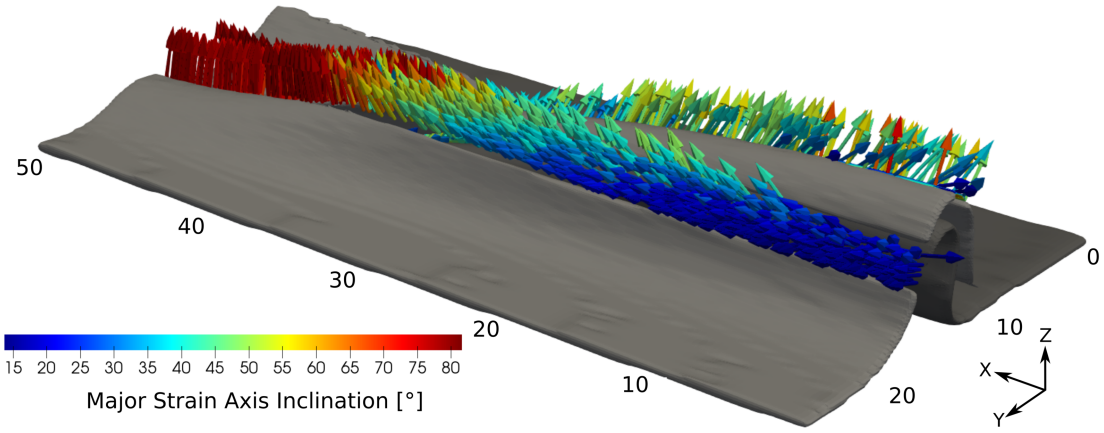

Figure 2.3: Orientation of the finite strain major axis for the two marker layers for configuration A after 40% bulk shortening. Vectors are pointing in the direction of the azimuth and are color-coded with the inclination of the major strain axis relativ to the XY-plane.

2.2 Results

2.2.1 General model evolution

We performed six simulations with a numerical resolution of 256x128x128 grid points utilizing six different initial geometries (Figure 2.1). Figure 2.4 shows the topographic evolution of configuration A from 10% to 40% bulk shortening. The top row displays the evolution of the model from the side that is dominated by folding and the bottom row from the side that is dominated by overthrusting. The deformation is initiated at the weak zone at Y = 25 km. For up to 20% bulk shortening overthrusting of the left layer on top of the right layer is the predominant mode of deformation. With further bulk shortening both layers undergo folding in areas of higher H_M/H_L. The height of the cylindrical fold depends on the ratio H_M/H_L. The transition between the folding and the thrusting domain displays a smooth cusp (Figure 2.4d, bottom row). In Figure 2.5 we display the topographic evolution after 40% bulk shortening for all simulations. In general, the fold and thrust evolution always follows the pre-existing weak zones (Figure 2.1). Configuration B (Figure 2.4b) shows as similar evolution to configuration A, with the fold hinge evolving along the oblique weak zone. Conversely, configuration Br (Figure 2.4c) shows the evolution of a continuous fold reaching to the end of the low H_M/H_L region, where we would have expected overthrusting. Figure 2.5d displays

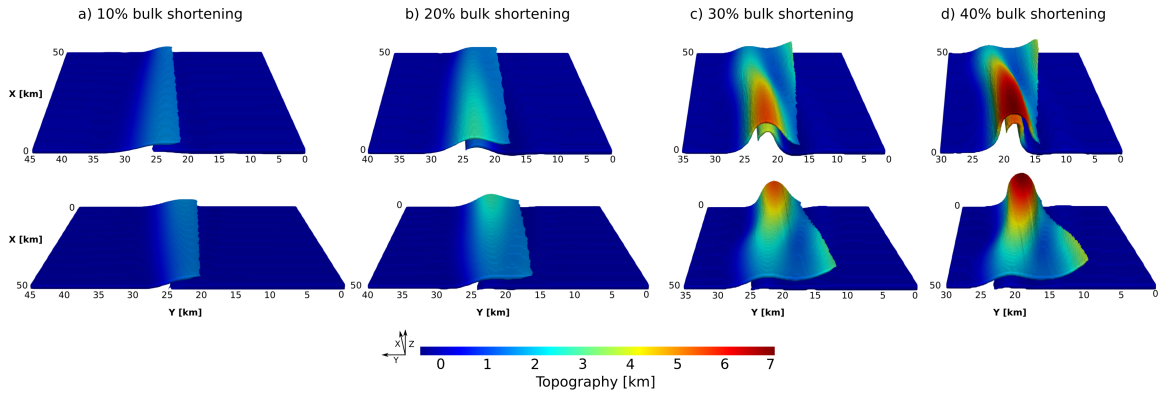

Figure 2.4: Topographic evolution of model configuration A. Panels a) to d) show model stages for bulk shortening in 10% increments from 10% to 40%,respectively. Top row: Model evolution with the view in the positive X-direction starting from X = 0 km. Bottom row: Model evolution with the view in the negative X-direction starting from X = 50 km.

the geometry of configuration C, where we observe three discrete zones: First a folding zone in front, followed by a transition zone across the flat ramp, joining into a thrusting dominated zone. We observe a similar pattern for configuration D and Dr (Figure 2.4e,f). In both simulations the transition zone follows the oblique ramp that culminates into a rear or frontal cusp in the transition zone, respectively.

In the following we focus on the analysis and visualization of finite strain in the rear and front marker layer (Figure 2.1a) of configuration A. The location of both marker layers was chosen in such a way that the rear marker layer is situated in the back limb of the evolving fold and the front marker layer in the front limb of the fold after 40% bulk shortening. Figure 2.6 shows the 3D geometry after 40% bulk shortening together with the a) ν and b) ε_s values of the marker layers. The magnitude and distribution of ν in the rear and front marker layer is similar. The highest ν values of 0.6 are inside the folding domain (X = 0 - 20 km). Going further in the X-direction the ν values decrease to 0.2 and then increase again to 0.4 along the transition from folding to thrusting. ν values along the marker layers are generally positive with the exception of the rear marker layer in the thrust sheet (X = 43 âĂŞ 50 km), where ν takes negative values of about -0.2. The negative values indicate that the rear layer in the thrusting sheet experiences constrictional strain. The ε_s values range from 0.014 to 0.21. Along the X-direction ε_s exhibits the minimum value for X = 0 to 30 km, whereas it increases to the maximum value from X = 30 - 50 km. In the front layer the maximum value occurs at around X = 35 km with ε_s = 0.18, where we also observe a slight kinking of the layer. In the rear layer, maximum ε_s values are located at the end of the thrusting domain. Here, the location of the higher strain values coincides with the constrictional strain given by ν. In general, ε_s values increase from the folding region to the thrusting region by one order of magnitude.

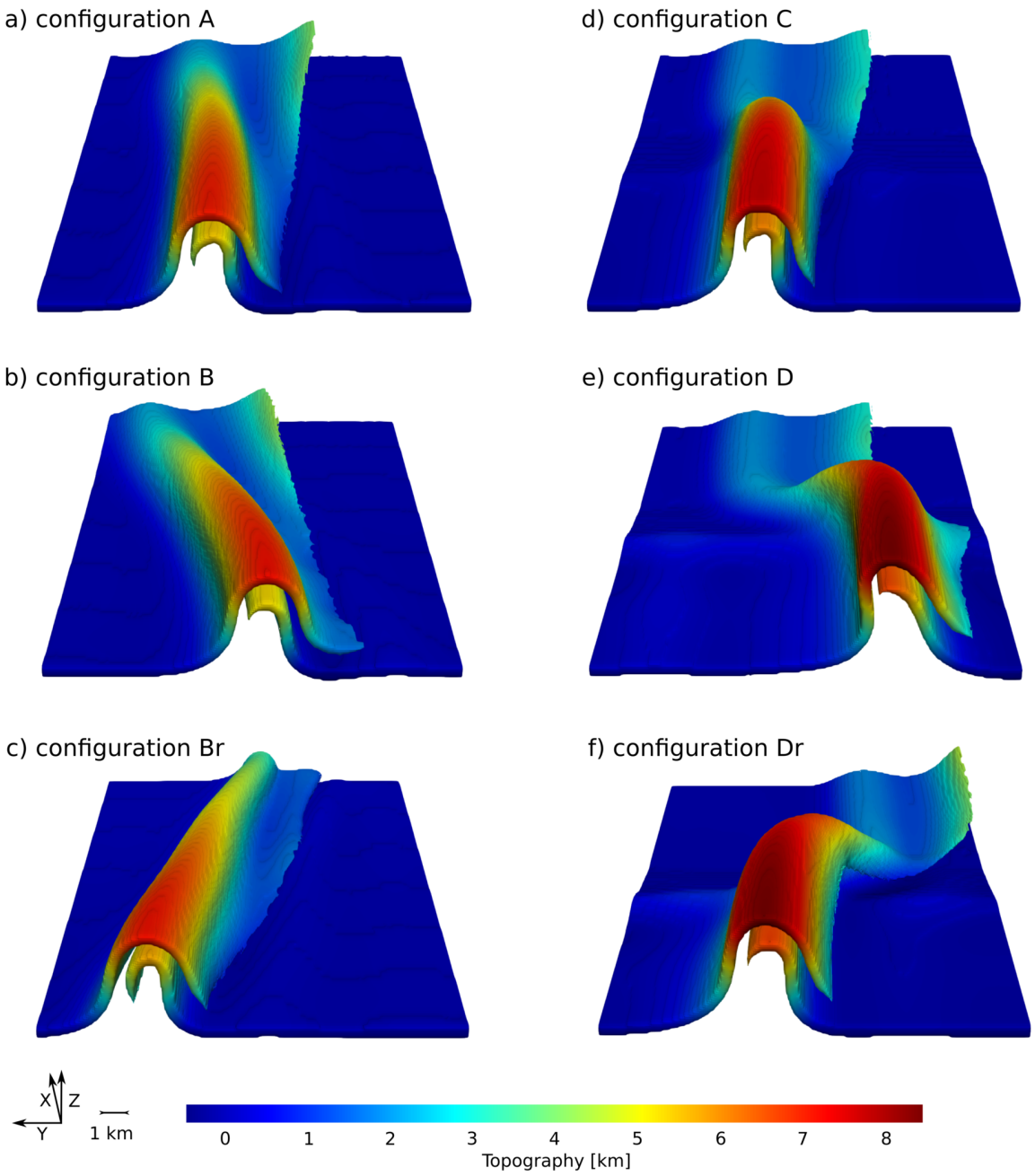

Figure 2.5: Topographic evolution of all six configurations after 40% bulk shortening, displaying the transition between folding and overthrusting. a) Configuration A: linear H_M/H_L distribution. b) Configuration B: linear H_M/H_L distribution with an oblique weak zone. c) Configuration Br: linear H_M/H_L distribution with a reversed oblique weak zone. d) Configuration C: H_M/H_L distribution facilitates a flat ramp geometry, e) configuration D: same lateral linear H_M/H_L distribution as configuration C but with a oblique weak zone across the ramp. f) Configuration Dr: same lateral linear H_M/H_L distribution as configuration C but with a reversed oblique weak zone across the ramp.

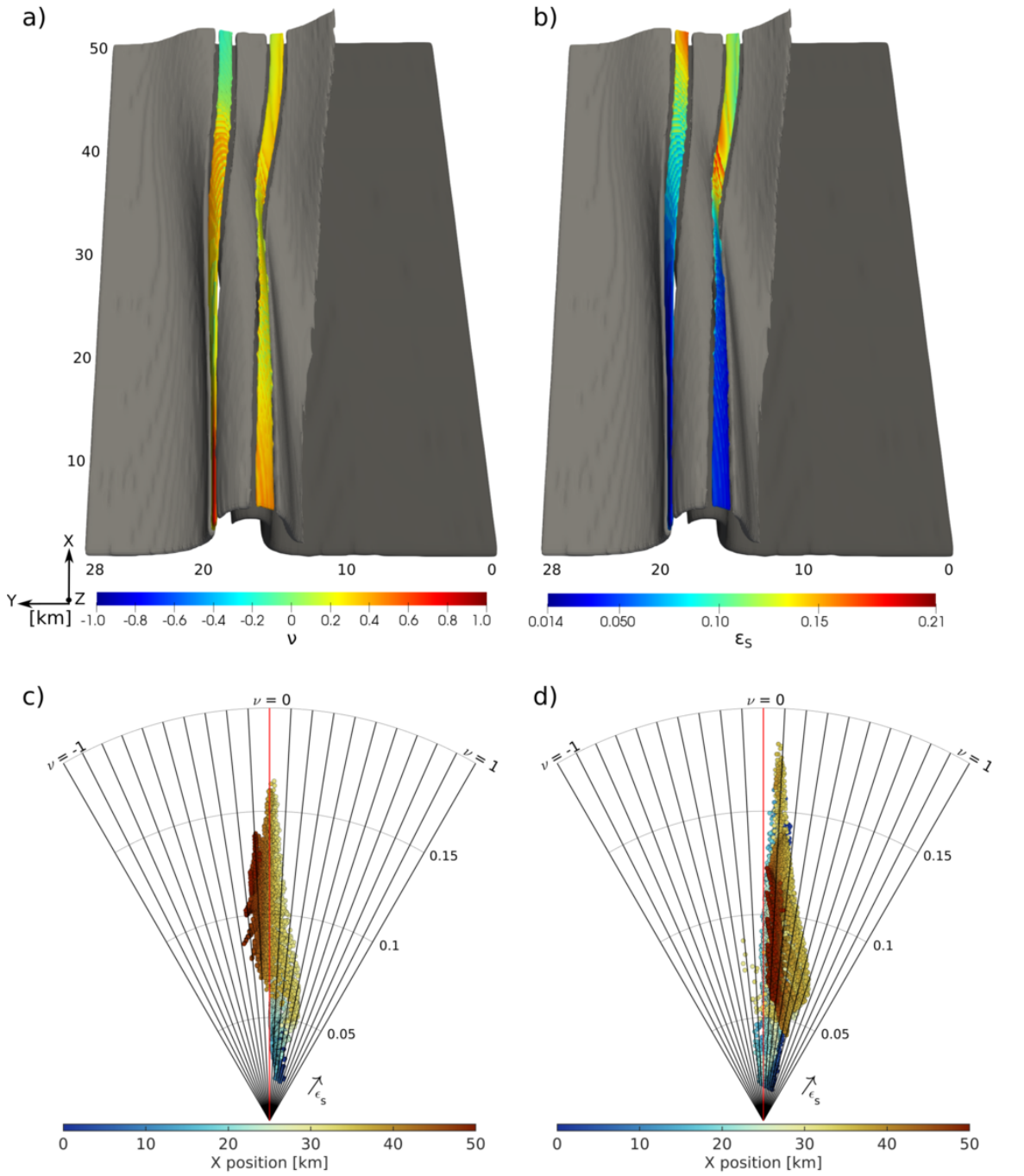

Figure 2.6: Results for model configuration A after 40% bulk shortening. a) Surface plot with the marker layers showing the ν values and b) showing the ε_s values. c) Hsu diagram for the rear marker layer, and d) Hsu diagram for the frontal marker layer with color-coded X-coordinate for all data points in the respective marker layer.

Figure 2.6c and d illustrates the relation between ν, ε_s and the corresponding X-position for each point of the rear and front marker layer inside a Hsu diagram. We observe a variable

distribution of ν and ε_s values for the same X-position, which is not apparent in the surface plot (Figure 2.6a,b). Both diagrams show a similar trend for ε_s. They display increasing values from the folding to the thrusting region. The Hsu diagrams show that ν can vary strongly for small ranges in X-position and small $\varepsilon_s < 0.1$. Moreover, they show that the deformation clearly deviates from plane strain ($\nu = 0$). For example, ν varies between 0 and 0.4 for $\varepsilon_s = 0.075$ in a X range from 30 to 40 km as seen in Figure 2.6c.

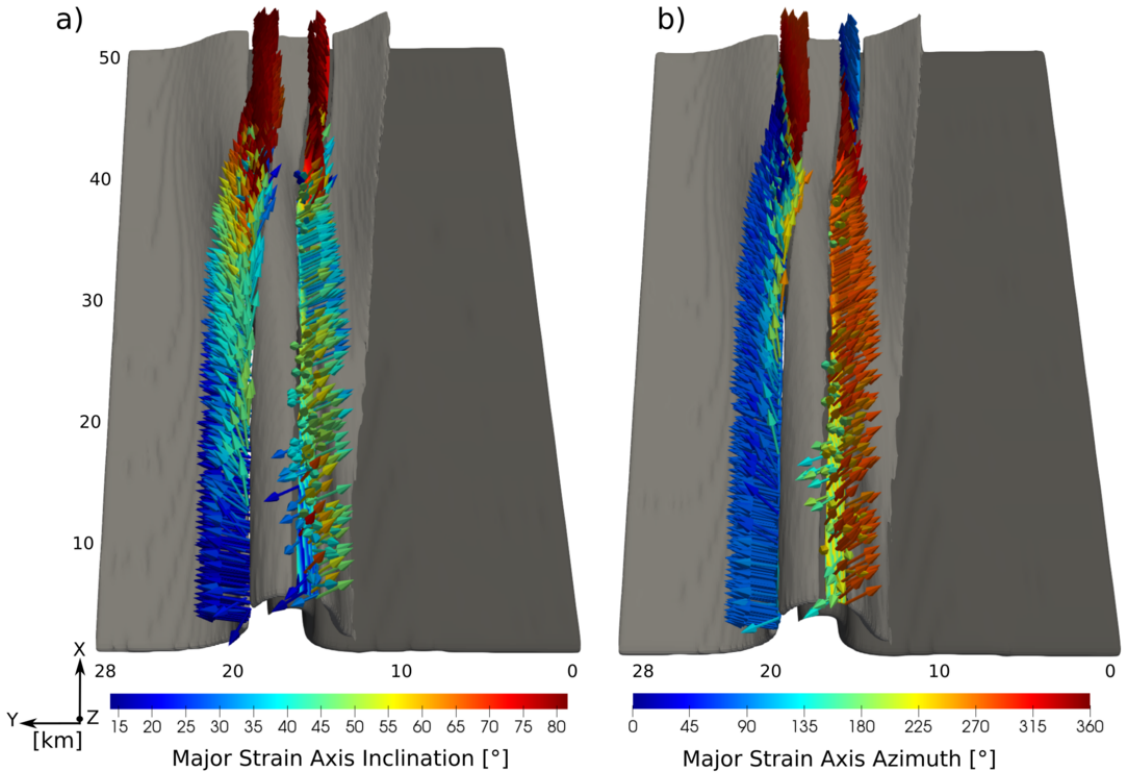

Figure 2.7: Results for model configuration A after 40% bulk shortening. a) Orientation of the finite strain major axis showing the color-coded inclination angle of the axes on the vector. b) Orientation of the finite strain major axis showing the color-coded azimuth of the axes on the vector.

Figure 2.7 shows the color-coded inclination (a) and the azimuth (b) of the major finite strain axis for the same simulation. For reference, an azimuth of 0 and 360° indicates that the major finite strain axis dips towards the positive X-direction. Azimuth values increase in the clockwise direction. For the inclination, an angle of 0° indicates that the major axis is parallel to the XY-plane. The inclination and azimuth point to three distinctive regions in our model configuration. For instance, the inclination in the rear layer (Figure 2.7a) reveals almost uniform values of 17° from X = 0 to 20 km. Next, from X = 20 to 40 km the inclination changes drastically to a range between 40° and 55°. Further in the thrusting region (X > 40 km) the inclination is almost vertical with a value of about 80 to 85°. The major finite

strain axis azimuth for the rear layer (Figure 2.7b) also reveals a sharp transition between an azimuth of about 90° in the folding domain to about 360° in the thrusting region (X $\simeq$ 40 km). Azimuth values in the rear and front marker layer that are in the folding region show uniform values of 90° and 270°, respectively. As expected, these orientations coincide with the bulk shortening direction.

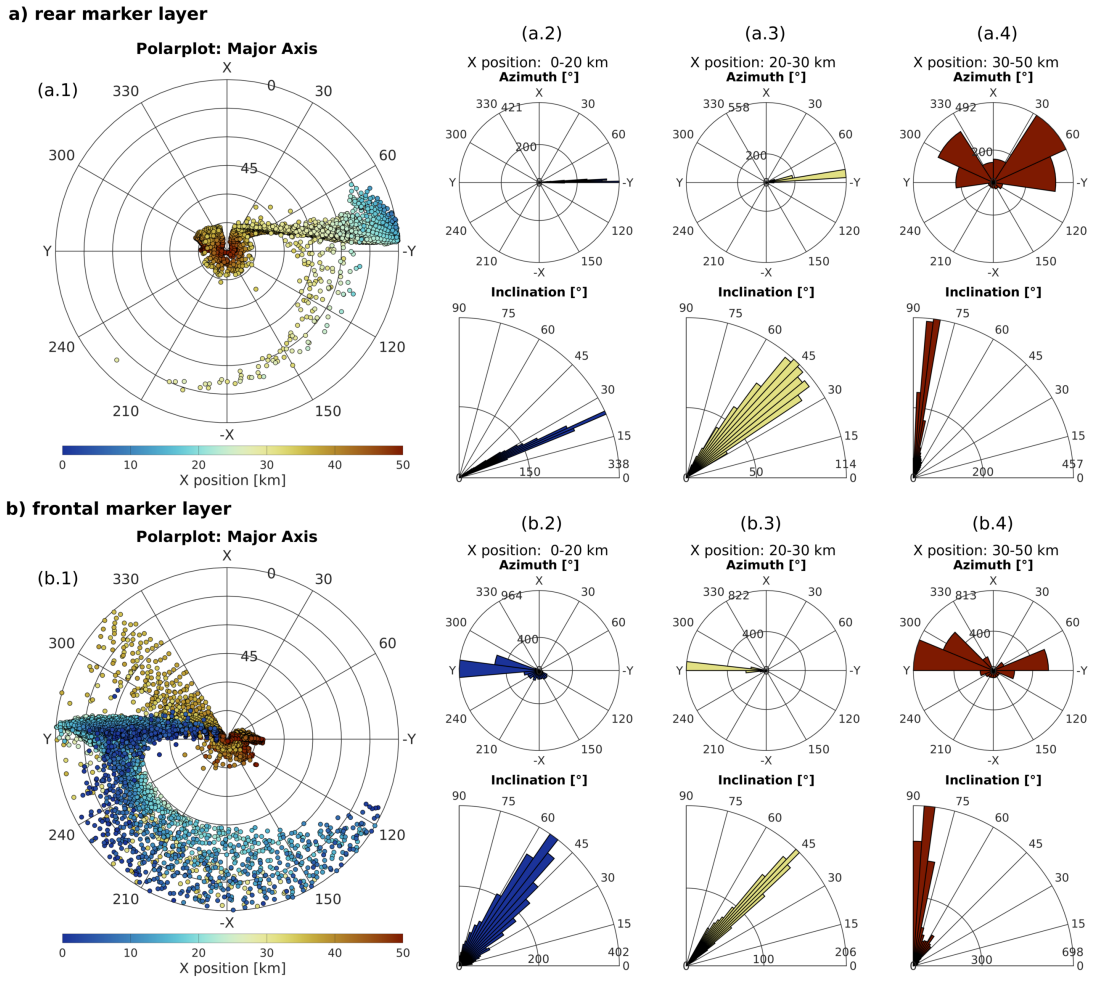

Figure 2.8: Orientation analysis for the finite strain major axis for the a) rear and b) front marker layer of configuration A after 40% bulk shortening. Polar diagram for (a.1) the rear layer and (b.1) the front layer with using a color-coded X-position. From left to right row wise: Polar histograms of the azimuth and corresponding inclination distribution for three different sections in X-direction: 0 - 20 km (a.2),(b.2), 20 - 30 km (a.3),(b.3) and 30 - 50 km(a.4),(b.4).

A detailed analysis of the major finite strain axis orientation is shown in Figure 2.8. Here, we utilize classical polar diagrams to illustrate the orientation of all data points. Additionally, we subdivide the marker layer in three sections in the lateral X-direction. For each of the sections we display a rose diagram for the azimuth and for the inclination. Data points in

the polar diagram are color-coded by X-position. Both polar diagrams reveal prevalent value clusters depending on the X-position. Additionally, we observe also some scatter that is more pronounced in the front marker layer. The significance of the scatter can be understood by taking the rose diagrams into account. For the rear marker layer (Figure 2.8a.1) we recognize three different clusters. The first cluster is located at an azimuth between 60° and 90° with an inclination between 0° and 30° (Figure 2.8a.1). This cluster represents the folding dominated region and has X-values between 0 and 25 km. Here, the rose diagrams for the first section (0 to 20 km) display a bulk azimuth around 90° with an inclination of around 20° to 28° (Figure 2.8a.2). The next cluster extends from the first cluster down to the mid point of the polar diagram. There, the azimuth is still similar to the first region with slight deviations (Figure 2.8a.1). Rose diagram values for the azimuth show bulk values close to 90°. However, the inclination increases to a bulk value around 45°, ranging from 30° to 60° in total (Figure 2.8a.3). The last cluster is located in the middle of the polar diagram showing almost a full 360° range for the azimuth. This cluster corresponds to X-values lying between 30 and 50 km. The rose diagram reveals that the bulk azimuth varies between 220° to 330° and from 30° to 90° (Figure 2.8a.3). Here, the bulk inclination is close to 90°. Hence, the principal strain axis is almost parallel to the vertical Z axis. The flipping of the azimuth values can be explained by the slight bending and bulging of the thrust sheet during overthrusting. Figure 2.8b.1 shows the result of the general polar diagram for the front marker layer. In contrast to the rear marker layer we do not recognize three different clusters, but rather two major clusters in addition with two zones of larger scatter. The first cluster has a bulk azimuth of 270° and inclinations from 0° to 90° and includes X-positions from 0 to 30 km. The cluster is accompanied by a large scatter in the lower half circle of the polar diagram. However, further inspection with the polar histograms (Figure 2.8b.2,3) shows that the scattered values are negligible compared to the overall bulk values. Bulk values of the azimuth shows an angle close to 270° and an inclination between 45° and 60°. The second cluster is located in the middle in the polar diagram and is connected to a scatter between the azimuth of 300° to 330° with inclinations from 0° to 90°. Here, the histograms show a bulk azimuth near 270° and 90° with high inclinations greater 80° (Figure 2.8b.4). The scatter can be identified in the inclination rose diagram and shows values between 45° and 80° (Figure 2.8b.4, bottom). This deviation from the bulk values could coincide with kinking of the front layer which is restricted to a short distance in X-direction. Our results show that finite strain quantities can be considerably variable within a viscous competent layer that deforms by both folding and overthrusting.

2.2.2 Evolution of ε_s and ν with progressive bulk shortening

Figure 2.9 shows the evolution of ε_s with progressive bulk shortening for 10, 20, 35 and 40% for the rear marker layer of configuration A. The magnitude of ε_s does not increase

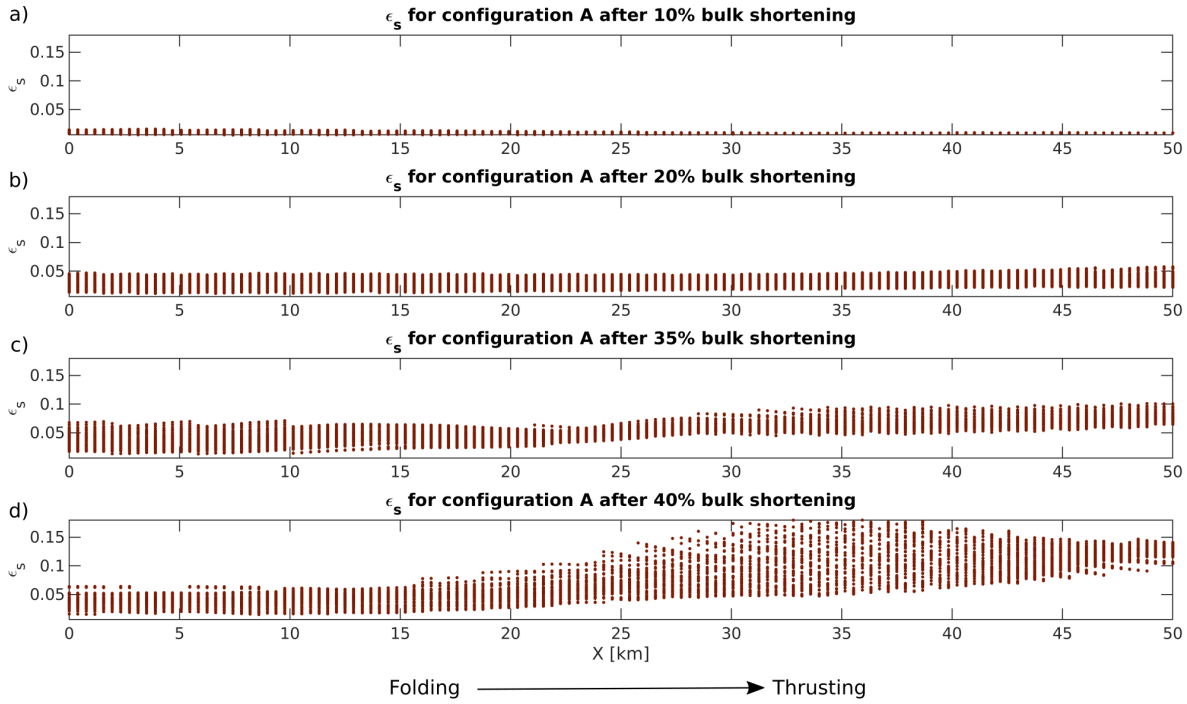

Figure 2.9: ε_s evolution for all points in the rear marker layer for configuration A for a) 10%, b) 20%, c) 35% and d) 40% bulk shortening.

significantly between 10% and 35% bulk shortening. From 35% on a slight strain increase towards the thrusting region is noticeable. At 40% bulk shortening ε_s (Figure 2.9d) values start to fan out between 20 and about 40 km X-position. The maximum ε_s values are around 0.18. One part of the marker layer rests in the back limb of the fold between X = 0 to 20 km, while the part between X = 40 to 50 km lies in the thrust sheet. The transition zone between folding and thrusting is therefore characterized by an increase of ε_s. This transition zone shows a larger variability of ε_s than the zones in which one deformation style is dominant. Similarly to the ε_s evolution, the ν evolution (Figure 2.10a-c) shows constant values from 10 to 35% bulk shortening. For these bulk shortening percentages values are close to zero, indicating a plane strain deformation. At 40% bulk shortening (Figure 2.10d) we observe ν ranging from 0.7 to 0 for X-positions between 0 and 40 km. The 40 km X-position marks the transition of ε_s from positive to negative values. Values from 40 km onwards range from 0 to -0.2, indicating a plane strain or constrictional strain ellipsoid. Overall we note two emerging trends, (i) for 10 to 20% (Figure 2.10a,b) bulk shortening ν values are negative on the folding side and positive on the thrusting side. However, (ii) once the rear marker layer becomes part of the rear fold limb ν takes on positive values in the folding region and transition zone and negative values at the end of the thrusting region (Figure 2.10c,d). In case of configuration A the ε_s distribution can be used to infer the width of the transition zone. Contrary, ν shows

homogeneous values for the folding and transition zone, but can be used to pinpoint the exact transition point to the thrusting domain.

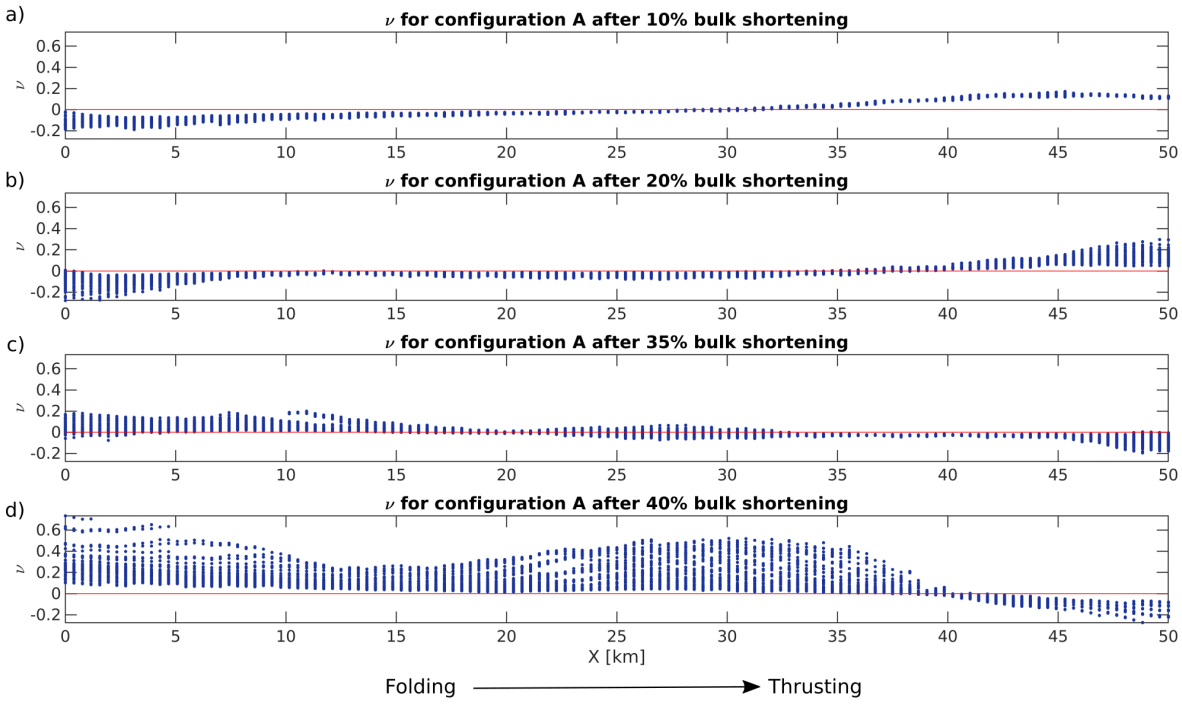

Figure 2.10: ν evolution for all points in the rear marker layer for configuration A for a) 10%, b) 20%, c) 35% and d) 40% bulk shortening. The red line indicates $\nu = 0$; plane strain deformation.

2.2.3 Profiles of ε_s and ν for all simulations

Spatial profiles of ε_s and ν for all simulations for the rear marker layer are given for a bulk shortening of 40 % in Figure 2.11 and Figure 2.12. The value distribution of ε_s in X-direction reflects the initial geometry and the transition from folding to thrusting. Simulations A, Br and B (Figure 2.11a-c) have smooth linear decrease of H_M/H_L from 1.0 to 0.125 and the ε_s values show a dense distribution from X = 0 to 20 km. The values then increase slowly with an increasing scatter from X = 20 to 40 km from where the scatter decreases again to an ε_s value around 0.15. In contrast, simulations C, Dr, and D (Figure 2.11d-f) show a different pattern of ε_s distribution. The strain magnitude rises sharply from X = 20 to 30 km, where we record a peak value of about 0.25. Simulation D and Dr show very tightly packed ε_s values in the transition zone. Here, the narrower value range could be linked to the oblique orientation of the weak zone across the ramp. After peaking, ε_s subsequently goes down to 0.15 in the thrusting region. The X-position of the peak ε_s values is directly related to the initial transition point of the flat ramp into the horizontal thrust sheet layer. Analogous, ν displays a characteristic distribution for the two types of different initial detachment horizon

configurations. With exception of simulation Br and B, ν values are positive with a variability from 0.2 to 0.8 in the folding domain (0 to 30 km). In contrast to the ε_s distribution we do not find a significant change of ν in the region of 20 to 30 km. Therefore ν cannot be used to identify the width of the transition zone. However, the immediate transition to the thrusting region is marked by a sharp collapse of ν to values close to zero, indicating a deformation mode close to plane strain.

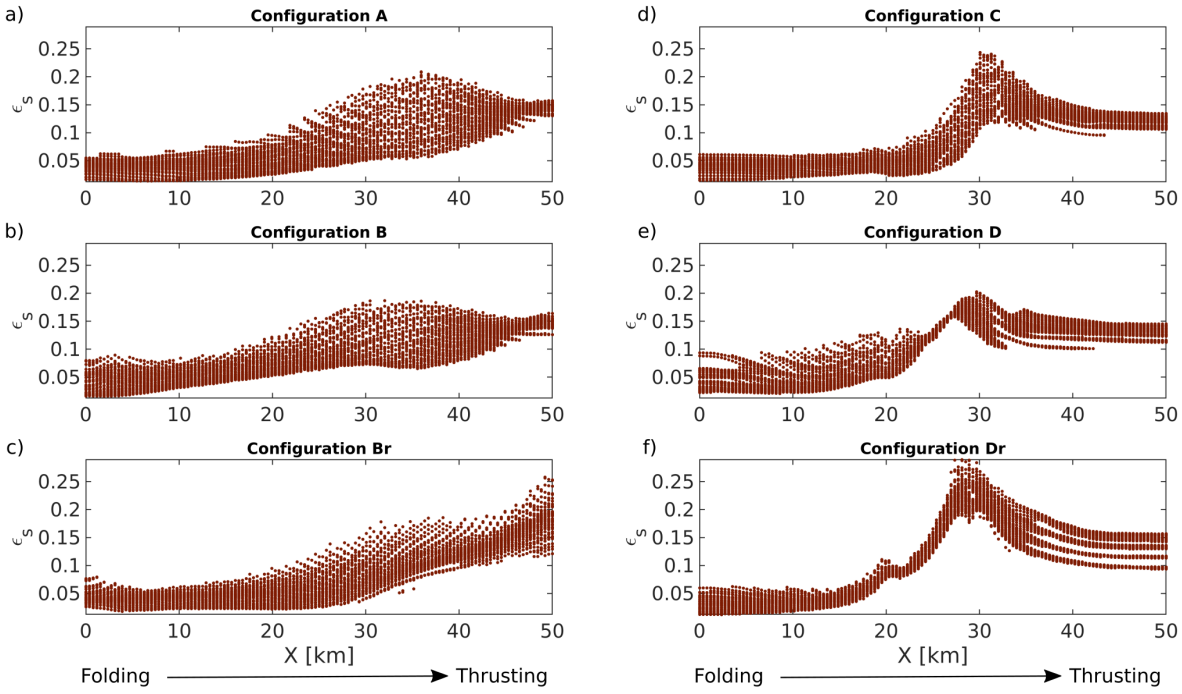

Figure 2.11: Compilation of ε_s values for all configurations for all points inside the rear marker layer after 40% bulk shortening. For all model configurations, ε_s shows higher values in the thrusting dominated region.

2.2.4 Bulk strike-slip shearing and internal lateral extension

Figure 2.13a displays the percentage of bulk strike-slip shear along the X-direction inside the rear marker layer. Positive shear values indicate that the folding domain moves faster in the shortening direction relative to the thrusting domain, whereas negative values imply the opposite. Bulk shear percentage between the folding and thrusting domain can be correlated to the initial orientation of the weak zone. In simulations A and C the weak zone is orthogonal to the shortening direction, resulting in a small bulk shear percentage of 1% compared to the other simulations. For simulations B and D the weak zone is oblique and for simulations Br and Dr the weak zone has the opposite obliquity. The obliquity orientation has a direct impact on the relative progression between the folding and overthrusting domains. We find a negative bulk shear for Br and Dr, whereas B and D with similar values display positive values.

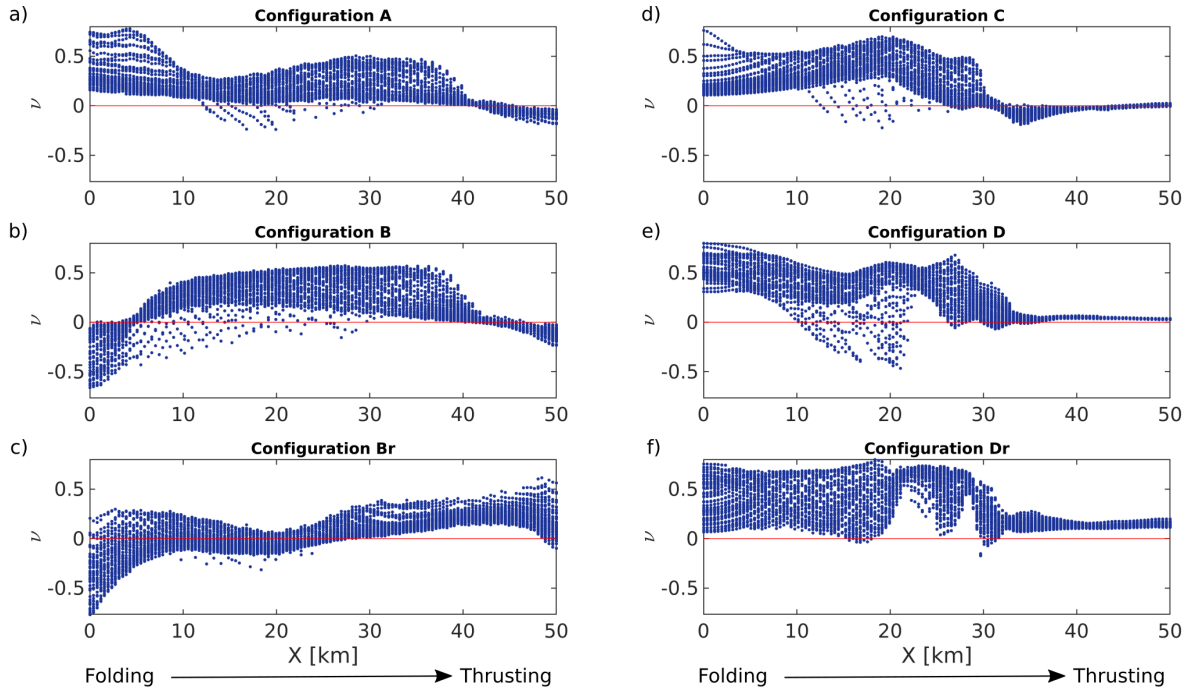

Figure 2.12: Compilation of ν values for all configurations for all points inside the rear marker layer after 40% bulk shortening.

Figure 2.13a implies that the overthrusting/folding layer experiences a lateral bulk strike-slip shearing due to the laterally varying deformation style, although the bulk deformation does not impose any bulk strike-slip shear.

In Figure 2.13b we show the change of average length of the rear marker layer during bulk shortening for all simulations. Positive values indicate an effective extension of the marker layer, whereas negative values indicate shortening. In contrast to the observation for the bulk strike-slip shear, we cannot link the polarity of the oblique weak zone to the change of layer length. Simulations B and Br show the same extensional behavior, while D and Dr show extension and compression of the rear layer. Similar to the internal strike-slip shear, Figure 2.13b illustrates that the rear marker layer experiences a lateral bulk extension or compression due to the laterally varying deformation style, although the imposed bulk deformation of the model in the lateral X-direction is zero.

2.3 Discussion

2.3.1 Finite strain visualization

Visualization of finite strain for 3D numerical simulations is challenging due to the various finite strain quantities, like ν and ϵ_s, and their evolution and variation in space and time.

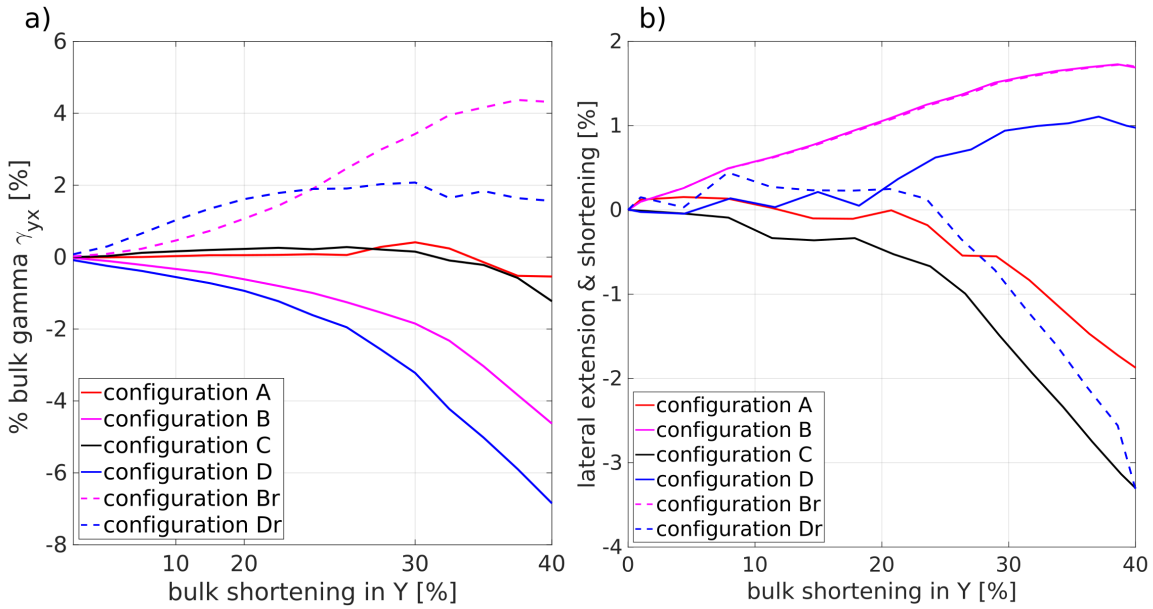

Figure 2.13: a) Evolution of bulk strike-slip shear strain, γ_{yx}, in the rear marker layer for all configurations. Positive values indicate higher relative displacement in the folding than in the thrust region. Negative values indicate the opposite. b) Evolution of relative extension or shortening of the length of the rear marker layer for all configurations. Positive values indicate extension and negative values indicate shortening.

Plotting values of ν and ϵ_s for individual locations in a Hsu diagram and color-coding the individual data points with respect to their spatial position in the 3D model is useful to characterize the variable finite strain in 3D models (Figure 2.6c,d). Such Hsu diagrams may also be useful for comparing finite strain from numerical simulations with finite strain data from geological field studies in order to gain further understanding on the deformation processes. We also display ν and ϵ_s separately in 2D profiles (e.g. Figure 2.11,Figure 2.12). These profiles are particularly useful to compare different simulations and corresponding ν and ϵ_s patterns. Similar to the surface plot for ν and ϵ_s (e.g Figure 2.6a) we additionally visualize the orientation of the principal strain axis, showing either the azimuth or inclination (Figure 2.7). Here, the primary advantage is the acquisition of a first order overview of the directions within the 3D geometry. Results of more complex model configurations that are directly based on geological reconstructions could be compared with data from geological maps, e.g. the orientation of stretching lineations (e.g. Dietrich, 1989; Steck, 2008). Yet, a more detailed analysis should be done with color-coded polar diagrams which help to identify clusters and patterns of data points. In addition, rose diagrams can provide a statistical analysis to identify the bulk direction of the finite strain major axis.

Finite strain quantification and visualization as we presented here is, of course, not only useful for fold and thrust belts, but has further applications in earth systems. For example, in mantle dynamics (Hess, 1964) finite strain orientation can be used to infer a first order

approximation of the lattice preferred orientation (McKenzie, 1979; Ribe, 1989) of the seismic anisotropies produced by ductile flow in the mantle. Hence, the visualization methods for finite strain presented here are equally applicable for other geological problems, such as the investigation of seismic anisotropies along a subducting plate (e.g. Buttles and Olson, 1998).

2.3.2 Modelling the lateral transition from folding to overthrusting

Many studies on fold-and-thrust belts using theoretical, analogue sandbox and numerical models assume a dominantly brittle or brittle-plastic deformation behavior (e.g. Chapple, 1978; Dahlen et al., 1984; Buiter, 2012; Graveleau et al., 2012). Yet, recent studies on fold-and-thrust belts suggest a systemic bias (Bond et al., 2007; Alcalde et al., 2017; Butler et al., 2018; Butler et al., 2019) towards brittle deformation in the interpretation of geological and seismic cross sections of fold-and-thrust belts. For example, Butler et al. (2019) argues that the over-reliance on idealization and over simplification of geological structures to a narrow range of geometrical structures, such as Dahlstrom's 'Foothills Family' (Dahlstrom, 1969), has resulted in a confirmation bias favoring brittle faulting as the dominant deformation style in fold-and-thrust belts. The above mentioned studies suggest that ductile folding, or buckling, might not be as rare in natural fold-and-thrust belts as often implied by previous studies. Therefore, folding and ductile deformation may play an important role during the evolution of fold-and-thrust belts, and ductile folding and brittle thrusting may often be of equal importance. Hence, our 3D viscous models of folding and overthrusting can provide important insights into the formation of fold-and-thrust belts.

Nearly all six different model configurations (Figure 2.1) show a transition between the two deformation styles folding and overthrusting (Figure 2.6); depending on the spatial variation of H_M/H_L and the weak zone geometry. The only exception is configuration Br (Figure 2.5c) which shows a continuous fold after 40% bulk shortening. However, in case of configuration Br overthrusting is still initiated at first, yet after ongoing shortening the fold propagates into the already established thrust sheet. This propagation might be explained by the differential deformation velocity between the two deformation styles caused by the orientation of the oblique weak zone. Since for configuration Br folding is initiated closer to the moving model boundary and overthrusting further away, fold development progresses relatively faster than overthrusting. Another reason could be the matrix thickness between the thrusting layer and the overthrusted layer. Small increases of the matrix thickness between both layers during overthrusting could favor folding. This result implies that despite initial H_M/H_L ratios favoring overthrusting, differential velocities and evolving H_M/H_L ratios during ongoing deformation could modify and change the favored deformation style from overthrusting to folding.

The oblique orientation of the weak zone along the ramp in configuration D and Dr (Figure 2.5e,f) results in a more uniform strain magnitude. In addition, the orientation of the weak zone determines the direction of the cusp in the transition zone. The two different spacial distributions of H_M/H_L ratio, either linear or more narrowly constrained by a flat ramp, produce a distinctive ϵ_s pattern (Figure 2.9). These different finite strain patterns could be used to infer subsurface structures from finite strain estimates in overlying geological units. For example, lateral or oblique ramps are quite common in nature (e.g. Butler et al., 2006; Wennberg et al., 1998; Zerlauth et al., 2014) and significantly influence the deformation at the surface (e.g. Boyer and Elliott, 1982). Given the knowledge of the mechanical stratigraphy, structural style and strain gradients from the field, computation of the finite strain could further aid in the refinement of geological models and reconstructions. Strain gradients and patterns could be used to pinpoint structural changes in the underlying lithology, but also to evaluate conceptual models.

Our numerical simulations record ca 2% bulk lateral extension and compression and up to 6% of bulk strike-slip shear in our marker layers (Figure 2.13). For the applied model configuration, these values indicate extensional, compressional and shear displacements in the order of kilometers (e.g. 2% extension equals 1 km). Such strains could locally produce brittle extensional and compressional faults with displacement directions orthogonal to the applied shortening direction although there was no bulk lateral deformation in the model. Similarly, local brittle strike-slip faults could be generated although there was no bulk strike-slip shear applied to the model. Our model, hence, shows the generation of considerable local strains which are only caused by the lateral transition from folding to overthrusting but not by an applied bulk deformation. If such finite strain would be observed in the field, it would have only a local significance and would not be usable for interpretations of the regional deformation. Our results show, hence, the importance of assessing whether observed deformation structures in the field are of only local or regional significance.

2.4 Conclusions

We present different visualization methods for 3D finite strain which are useful to characterize finite strain in 3D numerical simulations of folding and overthrusting. Hsu diagrams, indicating Nádai strain and Lode's ratio for individual locations, in combination with color-coding, indicating the relative spatial locations inside a model, are particularly useful to visualize finite strain and its spatial gradients. We also apply polar diagrams and rose diagrams to visualize the orientation of the principal strains and the spatial variation of this orientation in the 3D models. Our results show that finite strain varies considerably in space and time during the 3D evolution of folding and overthrusting

In the presented 3D models of power-law viscous flow, the lateral variation of deformation style, from folding to overthrusting, is caused by the lateral variation of the thickness and geometry of a detachment horizon. We applied bulk shortening only in one horizontal direction and there was no bulk deformation in the second, orthogonal horizontal direction. The lateral variation of the model geometry caused out-of-plane strain, orthogonal to the bulk shortening direction, and deviations from 2D plane strain which we quantified with Hsu diagrams. Furthermore, the strong layers experienced a bulk strike-slip shear deformation which was not imposed by the boundary conditions. Therefore, lateral variations in model geometry, mimicking natural tectonic inheritance, can cause (i) deviations from plane strain associated with lateral extension or compression and (ii) lateral bulk strike-slip shearing although there was no bulk lateral deformation and shear applied in the model. Consequently, natural observations of extensional and/or strike-slip shear structures do not necessarily indicate a regional-scale extension or strike-slip shearing. It is, hence, important to consider the impact of laterally varying geometries on the finite strain and shear in order to determine whether natural observations of finite strain have a regional significance or not.

Different lateral variations in geometry generate different lateral finite strain variations. Sharp lateral geometric variations, such as oblique ramps, cause considerable lateral variation in finite strain. Hence, finite strain patterns might be used in field studies to determine subsurface geometrical heterogeneities, such as sharp basement topography variations, associated with faults.

Acknowledgements

This work was supported by SNF grant No. 200020-149380 and the University of Lausanne. Moreover, this work was supported by a grant from the Swiss National Supercomputing Centre (CSCS) under project ID s785. In addition we thank Ludovic Räss and Philippe Logean for supporting us in the utilization of the Octopus Super Computing Cluster at the University of Lausanne. We also thank Arthur Bauville for his support in using the geomIO software.

Bibliography

Adam, J., Klinkmüller, M., Schreurs, G., Wieneke, B., 2013. Quantitative 3D strain analysis in analogue experiments simulating tectonic deformation: Integration of X-ray computed tomography and digital volume correlation techniques. Journal of Structural Geology 55, 127–149.

Alcalde, J., Bond, C.E., Johnson, G., Butler, R.W., Cooper, M.A., Ellis, J.F., 2017. The importance of structural model availability on seismic interpretation. Journal of Structural Geology 97, 161–171.

Díaz Azpiroz, M., Fernández, C., Czeck, D.M., 2018. Are we studying deformed rocks in the right sections? Best practices in the kinematic analysis of 3D deformation zones. Journal of Structural Geology .

Bauville, A., Baumann, T.S., 2019. geomIO: An Open-Source MATLAB Toolbox to Create the Initial Configuration of 2-D/3-D Thermo-Mechanical Simulations From 2-D Vector Drawings. Geochemistry, Geophysics, Geosystems .

Bauville, A., Epard, J.L., Schmalholz, S.M., 2013. A simple thermo-mechanical shear model applied to the Morcles fold nappe (Western Alps). Tectonophysics 583, 76–87.

Bauville, A., Schmalholz, S.M., 2013. Thermo-mechanical model for the finite strain gradient in kilometer-scale shear zones. Geology 41, 567–570.

Bauville, A., Schmalholz, S.M., 2017. Tectonic inheritance and kinematic strain localization as trigger for the formation of the Helvetic nappes, Switzerland. Swiss Journal of Geosciences 110, 523–534.

Beutner, E.C., 1977. Causes and consequences of curvature in the Sevier orogenic belt, Utah to Montana .

Bond, C.E., Gibbs, A.D., Shipton, Z.K., Jones, S., 2007. What do you think this is¿'Conceptual uncertainty"in geoscience interpretation. GSA today 17, 4.

Borradaile, G., Henry, B., 1997. Tectonic applications of magnetic susceptibility and its anisotropy. Earth-Science Reviews 42, 49–93.

Boutoux, A., Bellahsen, N., Lacombe, O., Verlaguet, A., Mouthereau, F., 2014. Inversion of pre-orogenic extensional basins in the external Western Alps: structure, microstructures and restoration. Journal of Structural Geology 60, 13–29.

Bower, A.F., 2009. Applied mechanics of solids. CRC press.

Boyer, S.E., Elliott, D., 1982. Thrust systems. Aapg Bulletin 66, 1196–1230.

Buiter, S.J., 2012. A review of brittle compressional wedge models. Tectonophysics 530, 1–17.

Burmeister, K., Harrison, M., Marshak, S., Ferré, E., Bannister, R., Kodama, K., 2009. Comparison of Fry strain ellipse and AMS ellipsoid trends to tectonic fabric trends in very low-strain sandstone of the Appalachian fold–thrust belt. Journal of Structural Geology 31, 1028–1038.

Butler, R.W., Bond, C.E., Cooper, M.A., Watkins, H., 2018. Interpreting structural geometry in fold-thrust belts: Why style matters. Journal of Structural Geology .

Butler, R.W., Bond, C.E., Cooper, M.A., Watkins, H., 2019. Fold–thrust structures–where have all the buckles gone? Geological Society, London, Special Publications 487, SP487–7.

Butler, R.W., Tavarnelli, E., Grasso, M., 2006. Structural inheritance in mountain belts: an Alpine–Apennine perspective. Journal of structural geology 28, 1893–1908.

Buttles, J., Olson, P., 1998. A laboratory model of subduction zone anisotropy. Earth and Planetary Science Letters 164, 245–262.

Chapple, W.M., 1978. Mechanics of thin-skinned fold-and-thrust belts. Geological Society of America Bulletin 89, 1189–1198.

Dahlen, F., Suppe, J., Davis, D., 1984. Mechanics of fold-and-thrust belts and accretionary wedges: Cohesive Coulomb theory. Journal of Geophysical Research: Solid Earth 89, 10087–10101.

Dahlstrom, C., 1969. Balanced cross sections. Canadian Journal of Earth Sciences 6, 743–757.

Dietrich, D., 1989. Fold-axis parallel extension in an arcuate fold-and thrust belt: the case of the Helvetic nappes. Tectonophysics 170, 183–212.

Flinn, D., 1962. On folding during three-dimensional progressive deformation. Quarterly Journal of the Geological Society 118, 385–428.

Fossen, H., Cavalcante, G.C.G., 2017. Shear zones–A review. Earth-Science Reviews 171, 434–455.

Fossen, H., Cavalcante, G.C.G., Pinheiro, R.V.L., Archanjo, C.J., 2018. Deformation–Progressive or multiphase? Journal of Structural Geology .

Fossen, H., Tikoff, B., 1993. The deformation matrix for simultaneous simple shearing, pure shearing and volume change, and its application to transpression-transtension tectonics. Journal of Structural Geology 15, 413–422.

Fry, N., 1979. Random point distributions and strain measurement in rocks. Tectonophysics 60, 89–105.

Gairola, V., 1977. Three-dimensional strains in fold-hinge zones. Tectonophysics 41, 291–319.

Graveleau, F., Malavieille, J., Dominguez, S., 2012. Experimental modelling of orogenic wedges: A review. Tectonophysics 538, 1–66.

Hess, H., 1964. Seismic anisotropy of the uppermost mantle under oceans. Nature 203, 629.

Hossack, J.R., 1968. Pebble deformation and thrusting in the Bygdin area (southern Norway). Tectonophysics 5, 315–339.

Hsu, T., 1966. The characteristics of coaxial and non-coaxial strain paths. Journal of Strain Analysis 1, 216–222.

Jaquet, Y., Bauville, A., Schmalholz, S.M., 2014. Viscous overthrusting versus folding: 2-D quantitative modeling and its application to the Helvetic and Jura fold and thrust belts. Journal of Structural Geology 62, 25–37.

Kaus, B., Popov, A.A., Baumann, T., Pusok, A., Bauville, A., Fernandez, N., Collignon, M., 2016. Forward and inverse modelling of lithospheric deformation on geological timescales, in: Proceedings of NIC Symposium.

Kligfield, R., Owens, W., Lowrie, W., 1981. Magnetic susceptibility anisotropy, strain, and progressive deformation in Permian sediments from the Maritime Alps (France). Earth and Planetary Science Letters 55, 181–189.

Laubscher, H., 1972. Some overall aspects of Jura dynamics. American Journal of Science 272, 293–304.

Lisle, R.J., Bastida, F., Aller, J., 2019. Measuring the research impact of the book Folding and Fracturing of Rocks by John G. Ramsay. Geological Society, London, Special Publications 487, SP487–8.

Lode, W., 1926. Versuche über den Einfluß der mittleren Hauptspannung auf das Fließen der Metalle Eisen, Kupfer und Nickel. Zeitschrift für Physik 36, 913–939.

Macedo, J., Marshak, S., 1999. Controls on the geometry of fold-thrust belt salients. Geological Society of America Bulletin 111, 1808–1822.

Marshak, S., Flöttmann, T., 1996. Structure and origin of the Fleurieu and Nackara Arcs in the Adelaide fold-thrust belt, South Australia: salient and recess development in the Delamerian Orogen. Journal of Structural Geology 18, 891–908.

Marshak, S., Wilkerson, M., Hsui, A., 1992. Generation of curved fold-thrust belts: Insight from simple physical and analytical models, in: Thrust tectonics. Springer, pp. 83–92.

McCarthy, D., Meere, P., Mulchrone, K., 2019. Determining finite strain: how far have we progressed? Geological Society, London, Special Publications 487, SP487–2018.

McCarthy, D.J., Meere, P.A., Petronis, M.S., 2015. A comparison of the effectiveness of clast based finite strain analysis techniques to AMS in sandstones from the Sevier Thrust Belt, Wyoming. Tectonophysics 639, 68–81.

McKenzie, D., 1979. Finite deformation during fluid flow. Geophysical Journal International 58, 689–715.

Means, W., Hobbs, B., Lister, G., Williams, P., 1980. Vorticity and non-coaxiality in progressive deformations. Journal of Structural Geology 2, 371–378.

Merschat, A.J., Hatcher Jr, R.D., Davis, T.L., 2005. The northern Inner Piedmont, southern Appalachians, USA: kinematics of transpression and SW-directed mid-crustal flow. Journal of Structural Geology 27, 1252–1281.

Mitra, G., 1994. Strain variation in thrust sheets across the Sevier fold-and-thrust belt (Idaho-Utah-Wyoming): Implications for section restoration and wedge taper evolution. Journal of Structural Geology 16, 585–602.

Mitra, G., 1997. Evolution of salients in a fold-and-thrust belt: the effects of sedimentary basin geometry, strain distribution and critical taper, in: Evolution of geological structures in micro-to macro-scales. Springer, pp. 59–90.

Mookerjee, M., Mitra, G., 2009. Understanding kinematic data from the Moine thrust zone in terms of a kinematics-based mathematical model of deforming thrust wedges. Journal of Structural Geology 31, 1556–1572.

Mookerjee, M., Peek, S., 2014. Evaluating the effectiveness of Flinn's k-value versus Lode's ratio. Journal of Structural Geology 68, 33–43.

Mulchrone, K.F., 2003. Application of Delaunay triangulation to the nearest neighbour method of strain analysis. Journal of Structural Geology 25, 689–702.

Nádai, A., Hodge, P., 1963. Theory of Flow and Fracture of Solids, vol. II. Journal of Applied Mechanics 30, 640.

Pfiffner, O.A., 1993. The structure of the Helvetic nappes and its relation to the mechanical stratigraphy. Journal of structural Geology 15, 511–521.

Pollard, D., Pollard, D.D., Fletcher, R.C., Fletcher, R.C., 2005. Fundamentals of structural geology. Cambridge University Press.

Ragan, D.M., 2009. Structural geology: an introduction to geometrical techniques. Cambridge University Press.

Ramsay, J.G., 1967. Folding and fracturing of rocks. Mc Graw Hill Book Company 568.

Ramsay, J.G., Huber, M.I., 1987. The techniques of modern structural geology: Folds and fractures. volume 2. Academic press.

Ramsay, J.G., Wood, D.S., 1973. The geometric effects of volume change during deformation processes. Tectonophysics 16, 263–277.

Ribe, N.M., 1989. Seismic anisotropy and mantle flow. Journal of Geophysical Research: Solid Earth 94, 4213–4223.

Ries, A., 1976. A Discussion on natural strain and geological structure-Patterns of strain variation in arcuate fold bets. Philosophical Transactions of the Royal Society of London. Series A, Mathematical and Physical Sciences 283, 281–288.

Robin, P.Y.F., Charles, C.R., 2015. Quantifying the three-dimensional shapes of spheroidal objects in rocks imaged by tomography. Journal of Structural Geology 77, 1–10.

Shimamoto, T., Ikeda, Y., 1976. A simple algebraic method for strain estimation from deformed ellipsoidal objects. 1. Basic theory. Tectonophysics 36, 315–337.

Steck, A., 2008. Tectonics of the Simplon massif and Lepontine gneiss dome: deformation structures due to collision between the underthrusting European plate and the Adriatic indenter. Swiss Journal of Geosciences 101, 515–546.

Tikoff, B., Fossen, H., 1999. Three-dimensional reference deformations and strain facies. Journal of Structural Geology 21, 1497–1512.

Von Tscharner, M., Schmalholz, S., Epard, J.L., 2016. 3-D numerical models of viscous flow applied to fold nappes and the Rawil depression in the Helvetic nappe system (western Switzerland). Journal of Structural Geology 86, 32–46.

Tullis, T.E., Wood, D.S., 1975. Correlation of finite strain from both reduction bodies and preferred orientation of mica in slate from Wales. Geological Society of America Bulletin 86, 632–638.

Twiss, R.J., Moores, E.M., 1992. Structural geology. Macmillan.

Wennberg, O.P., Milnes, A.G., Winsvold, I., 1998. The northern Bergen Are Shear Zone an oblique-lateral ramp In the Devonian extensional detachment system of western Norway. Norsk Geologisk Tidsskrift .

Woodward, N.B., Gray, D.R., Spears, D.B., 1986. Including strain data in balanced cross-sections. Journal of Structural Geology 8, 313–324.

Zerlauth, M., Ortner, H., Pomella, H., Pfiffner, O.A., Fügenschuh, B., 2014. Inherited tectonic structures controlling the deformation style: an example from the Helvetic nappes of the Eastern Alps. Swiss Journal of Geosciences 107, 157–175.

Zwaan, F., Schreurs, G., Naliboff, J., Buiter, S.J., 2016. Insights into the effects of oblique extension on continental rift interaction from 3D analogue and numerical models. Tectonophysics 693, 239–260.

CHAPTER 3

Control of 3D tectonic inheritance on fold and thrust belts: insights from 3D numerical models and application to the Helvetic nappe system, Switzerland

Richard Spitz[1,2], Arthur Bauville[4], Jean-Luc Epard[1], Boris J.P. Kaus[3], Anton A. Popov[3]and Stefan M. Schmalhoz[1,2]

[1]Faculté des géosciences et de l'environnement, Institut des Sciences de la Terre, University of Lausanne, Lausanne, Switzerland.

[2]Swiss Geocomputing Centre, University of Lausanne, Lausanne, Switzerland.

[3]Institute of Geosciences, Johannes-Gutenberg University, Mainz, Germany.

[4]Department of Mathematical Science and Advanced Technology, JAMSTEC, Yokohama, Japan.

In review at Solid Earth, November 2019

Abstract

Fold-and-thrust belts and associated tectonic nappes are common in orogenic regions. They exhibit a wide variety of geometries and often a considerable along-strike variation. However, the mechanics of fold-and-thrust belt formation and the control of the initial geological configuration on this formation are still incompletely understood. Here, we apply three-dimensional (3D) thermo-mechanical numerical simulations of the shortening of the upper crustal region of a passive margin to investigate the control of 3D laterally variable inherited structures on the fold-and-thrust belt evolution and associated nappe formation. We consider tectonic inheritance by applying an initial model configuration with horst and graben structures having laterally variable geometry and with sedimentary layers having different mechanical strength. We use a visco-plastic rheology with temperature dependent flow laws and a Drucker-Prager yield criterion. The models show the folding, detachment and horizontal displacement of sedimentary units, which resemble structures of fold and thrust nappes. The models further show the stacking of nappes. The detachment of nappe-like structures is controlled by the initial basement and sedimentary layer geometry. Significant horizontal transport is facilitated by weak sedimentary units below these nappes. The initial half-graben geometry has a strong impact on the basement and sediment deformation. Generally, deeper half-grabens generate thicker nappes and stronger deformation of the neighboring horst while shallower half-grabens generate thinner nappes and less deformation in the horst. Horizontally continuous strong sediment layers, which are not restricted to inital graben structures, cause detachment folding and not overthrusting. The amplitude of the detachment folds is controlled by the underlying graben geometry. A mechanically weaker basement favors the formation of fold nappes while stronger basement favors thrust sheets. The applied model configuration is motivated by the application of the 3D model to the Helvetic nappe system of the French-Swiss Alps. Our model is able to reproduce several first-order structural features of this nappe system, namely (i) closure of a half-graben and associated formation of the Morcles and Doldenhorn nappes, (ii) the overthrusting of a nappe resembling the Wildhorn and Glarus nappes and (iii) the formation of a nappe pile resembling the Helvetic nappes resting above the Infrahelvetic complex. Furthermore, the finite strain pattern, temperature distribution and timing of the 3D model is in broad agreement with data from the Helvetic nappe system. Our model, hence, provides a first-order 3D reconstruction of the tectonic evolution of the Helvetic nappe system based on thermo-mechanical deformation processes.

3.1 Introduction

Fold-and-thrust belts are common in nature and typically associated with orogenic belts, such as the Himalayas or the European Alps (e.g. Price and McClay, 1981; Lacombe and Bel-

lahsen, 2016). The structural interpretation of fold-and-thrust belts is based on the interaction between the crystalline basement and the overlying sedimentary cover. Two end-member deformation styles are commonly distinguished: thin-skinned deformation, without significant basement involvement, and thick-skinned deformation, with significant basement involvement (Rodgers, 1949; Pfiffner, 2006). Due to their importance for the fundamental understanding of mountain building processes and for natural resources exploration, the formation of fold-and-thrust belts has been studied since several decades with field and modelling studies (e.g. Davis et al., 1983; Dahlen, 1984; Dahlen and Suppe, 1988; Beutner, 1977; Price and McClay, 1981; Gillcrist et al., 1987; Butler, 1989; Ramsay, 1989; Buchanan and Buchanan, 1995: Dunn et al., 1995; Mitra, 1997; Lacombe and Mouthereau, 2002; Wissing and Pfiffner, 2003; Simpson, 2011; Yamato et al., 2011; Ruh et al., 2012; Fernandez and Kaus, 2014; Bellahsen et al., 2012; Bauville and Schmalholz, 2015; Lacombe and Bellahsen, 2016; Bauville and Schmalholz, 2017). However, the mechanical deformation processes controlling fold-and-thrust belt evolution are still incompletely understood. One challenge for understanding fold-and-thrust belt evolution is that the formation, spacing, orientation and time-sequence of thrusts, shear zones and folds are controlled by two different factors: First, the mechanical deformation behavior of rocks, which can be dominated either by brittle-frictional sliding or by ductile creep and can further be strongly affected by various mechanical softening mechanisms, such as frictional strain softening, reduction of effective friction by fluid overpressure, grain size reduction with damage or thermal softening. Second, the geometrical configuration, such as half-graben structures or orientation of sedimentary layers, and variations in rock strength, for example between basement and cover or within the cover by alternation of strong, such as carbonates, and weak, such as shales, sediments. To illustrate these two controlling factors in a simple way, let us consider the deformation of a linear viscous material under homogeneous pure shear. Adding a circular inclusion with a smaller viscosity to the viscous material will not generate a shear zone inside the linear viscous material for this deformation configuration. The only possibility to generate a shear zone in the viscous material is to add a softening mechanism, such as thermal softening (Jaquet et al., 2015; Kiss et al., 2019) or grain-size reduction with damage (Bercovici and Ricard, 2003; Austin et al., 2008). In contrast, if the linear viscous material is sheared over a non-planar interface, resembling a half-graben, then a shear zone can develop inside the linear viscous material even without any softening mechanism (Bauville and Schmalholz, 2017). Therefore, a main challenge for understanding the thermo-mechanical evolution of fold-and-thrust belts is to determine whether the major thrusts and shear zones have been controlled by a particular rheological softening mechanism or by pre-existing geometrical and mechanical heterogeneities, referred to here as tectonic inheritance. In nature, there is most likely a continuous transition between these two controlling factors.

Many studies employing analogue and numerical models have been performed with a focus on the impact of different rheological models. Studies investigated the impact of brittle,

brittle-ductile, visco-plastic and visco-elasto-plastic rheological models on fold-and-thrust belt evolution, and also studied, for example, the impact of fluid pressure and associated reduction of effective friction (e.g. King Hubbert and Rubey, 1959; Stockmal, 1983; Merle, 1989; Simpson, 2011; Ruh et al., 2014; Poulet et al., 2014; Bauville and Schmalholz, 2015; Granado and Ruh, 2019). Other numerical studies focused more on the impact of tectonic inheritance, in the form of mechanical heterogeneities, on fold-and-thrust belt evolution (Wissing and Pfiffner, 2003; Bauville and Schmalholz, 2017). The majority of numerical modeling studies uses two dimensional (2D) models, which were often able to produce results that are to first oder comparable with geological reconstructions and cross-sections. However, it is well known that the style of fold-and-thrust belts can vary considerably along-strike the belt (e.g. Hamilton, 1988; Mitra and Fisher, 1992; Mitra, 1997; Mouthereau et al., 2002; Fitz Diaz et al., 2011; Nemčok et al., 2013). Inherited, laterally varying pre-existing structures are important, for example, in the Alps where pre-Alpine laterally varying passive margin structure presumably exert a strong control on the deformation style (Pfiffner, 1993; Pfiffner et al., 2011). A recent study of the Iberian passive margin by Lymer et al. (2019) highlights the complex 3D architecture of such margins. Their results imply that fault systems disappear laterally or link together in lateral direction along the margin, consequently creating discontinuities and geometrical asymmetries. Therefore, it is important to consider the 3D inherited heterogeneities of passive margins when studying fold-and-thrust belts that resulted from the deformation of passive margins, as is the case for the Helvetic fault-and-thrust belt (Pfiffner et al., 2011).

Here, we apply a 3D thermo-mechanical numerical model to investigate the fundamental impacts of mechanical heterogeneities, representing graben structures and sedimentary layering, on the deformation style during fold-and-thrust belt formation. A particular aim is to apply our model results to the Helvetic nappe system in the Swiss-French Alps (see next section). We employ an initial model configuration that mimicks a simplified upper crustal region of a passive margin and is composed of a basement and several sedimentary units. The passive margin contains a half-graben system that varies along the lateral direction. Moreover, we apply laboratory derived temperature dependent dislocation creep flow laws for all our model units and consider a brittle-frictional Drucker-Prager yield stress. We use a typical velocity boundary condition to simulate the large scale deformation conditions during tectonic wedge formation (Simpson, 2011; Ruh et al., 2014). In order to keep our model relatively simple, we concentrate on the thermo-mechanical processes on the macroscale and the impact on kilometer-scale structures. Hence, we do not consider microscale processes such as grain size reduction involving secondary mineral phases and damage. Furthermore, our model does not include hydro-chemical coupling. Hence, we do not model processes such as fluid release and decarbonatization (Poulet et al., 2014).

The aims of our study are to: (1) understand the impact of lateral changes in half-graben geometry on the deformation style, (2) investigate the importance of the spatial distribution

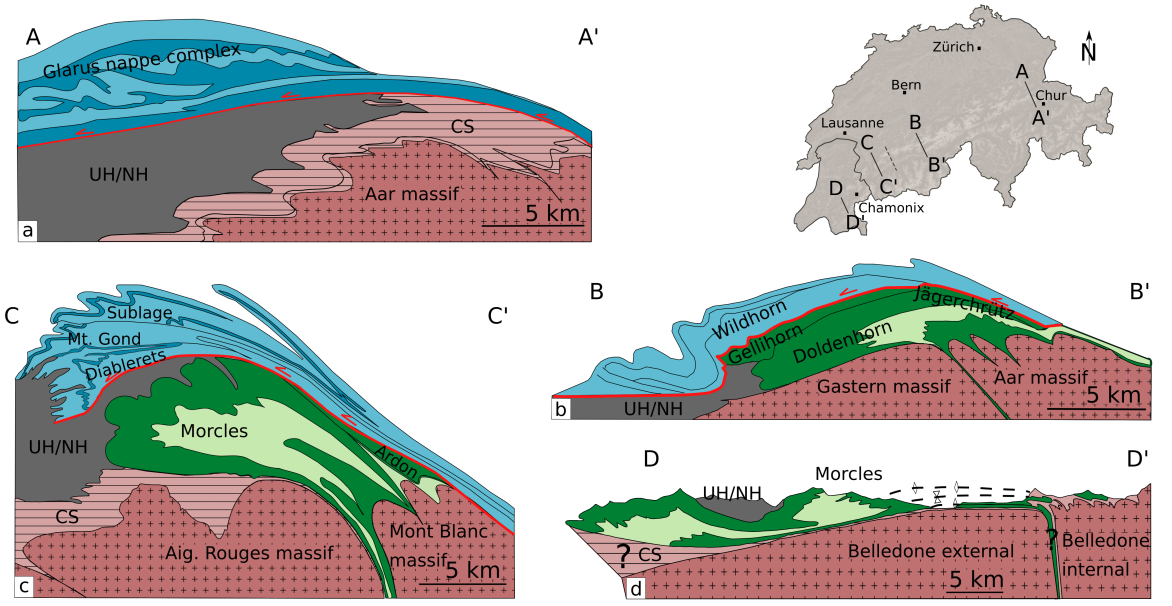

Figure 3.1: Simplified geological cross-sections along strike of the Helvetic nappe system. a) Glarus nappe complex (modified after Pfiffner, 2015). b) Doldenhorn nappe (modified after Kirschner et al., 1999). c) Morcles nappe (modified after Escher et al., 1993). d) Morcles nappe at the Belledonne massif (modified after Epard, 1990). UH/NH = Ultrahelvetics/North Helvetics. CS = Cover sediments.

of a competent layer and half-graben geometry during fold-and-thrust belt formation and (3) discuss the application of our numerical models to the formation of the Helvetic nappe system.

3.2 Overview of the Helvetic Nappe system

The Helvetic nappe system is a fold-and-thrust belt complex that was formed during the Alpine orogeny when the European passive margin collided with the Adriatic margin (e.g. Trümpy et al., 1980; Pfiffner, 2015). The system consists of a pile of tectonics nappes, which mainly comprise Mesozoic and Cenozoic sediments derived from the former European continental margin (Masson et al., 1980; Ramsay, 1981; Pfiffner, 1993; Escher et al., 1993; Steck, 1999; Pfiffner et al., 2011). Commonly, the nappe system is subdivided in the structurally upper Helvetic nappes, considered mainly as allochtonous thrust nappes, and the structurally lower Infrahelvetic complex, which can involve par-authochtonous fold nappes (Pfiffner, 1993; Pfiffner et al., 2011) (Figure 3.1).

The onset of Alpine burial of the proto-nappe system is constrained by the last deposited sediments with ages of ca. 28 to 34 Ma (Kirschner et al., 1995; Nibourel et al., 2018). Peak metamorphic conditions in the Helvetic nappe system occurred between ca. 25 and 17 Ma, indicating the end of the main phase of nappe stacking (Kirschner et al., 1995; Nibourel

et al., 2018). The main phase of nappe formation and stacking occurred presumably during a period of ca. 10 to 15 Ma (Masson et al., 1980; Milnes and Pfiffner, 1980; Burkhard, 1988; (Kirschner et al., 1995; Nibourel et al., 2018). Uplift and exhumation of the Helvetic nappe system occurred between ca. 20 Ma and today (Kirschner et al., 1995; Nibourel et al., 2018). We focus here on the main phase of nappe formation and stacking and do not consider the subsequent uplift and exhumation of the Helvetic nappe system.

The Helvetic nappe system exhibits a wide range of nappe geometries, including two commonly considered end-member nappe styles, namely fold nappes and thrust nappes, or thrust sheets (Termier, 1906; Epard and Escher, 1996). Fold nappes are recumbent folds with fold amplitudes of several kilometers and with a stratigraphic inversion in a prominent overturned limb. Thrust nappes are coherent allochtohonous rock sheets that are displaced along a basal shear zone and lack a prominent overturned limb.

We consider here four simplified geological sections across the Helvetic nappe system in the Swiss-French Alps and focus on several prominent nappes within these sections (Figure 3.1). The first order tectonic features of these four cross sections and the associated nappes will be compared with our 3D modelling results.

The first section includes the Glarus nappe of the Eastern Swiss Helvetic nappes (Figure 3.1a). Geological reconstructions suggest a displacement of approximately 50 km from its original location along a thin basal thrust zone that is composed of Mesozoic sediments (e.g. Pfiffner, 2015). Studies suggest that the Glarus basal thrust originates inside Carboniferous strata allowing for the transport of the Glarus nappe consisting of Permian Verrucano units at its base (e.g. Schmid, 1975; Pfiffner, 1993; Pfiffner, 2015). Observations on the thrust zone suggest earlier viscous dominated deformation followed by dominantly brittle deformation (Herwegh et al., 2008). A number of studies investigated the complex deformation behavior of the thrust zone and suggest the involvement of pressurized fluids that resulted in hydrofracture networks and the reduction of the friction at the base (e.g. Burkhard et al., 1992; Badertscher and Burkhard, 2000; Badertscher et al., 2002; Herwegh et al., 2008; Hürzeler and Abart, 2008). Recently, Poulet et al., 2014 suggest a superposition of viscous and brittle deformation mechanisms due to ductile shear heating resulting in decarbonatization and the release of overpressurized fluids causing brittle fracturing.

The second section includes the Doldenhorn nappe, belonging to the Infrahelvetic complex, which has been overthrusted by the Wildhorn nappe, belonging to the Helvetic nappes (Figure 3.1b). The Doldenhorn nappe consists of Mesozoic and Cenozoic parautochthonous sediments that have been squeezed and sheared out of a pre-Alpine half-graben, referred to here as North Helvetic basin (Figure 3.2). The Gellihorn and Jägerchrütz nappes are minor nappes and their sediments are considered as deposits on a basement high, likely a horst, which seperated the half-graben including the Doldenhorn sediments from the more distal marginal basin, referred

to here as Helvetic basin, on which the Wildhorn sediments have been deposited (Masson et al., 1980) (Figure 3.2). The Doldenhorn nappe roots in the Aar basement massif. Studies indicate metamorphic peak temperatures in the Doldenhorn nappe of up to $380°C$ (Herwegh and Pfiffner, 2005; Ebert et al., 2007a). These temperatures allowed for ductile deformation and folding of the Doldenhorn nappe during nappe formation. Colder temperatures around ca. $250\ °C$ in the structurally higher Wildhorn nappe were likely responsible for a deformation style resembling more a thrust nappe.

The third section includes the Morcles fold nappe (Figure 3.1c) belonging to the Infrahelvetic complex. It is overlain by a major thrust nappe, which is termed in this region the Wildhorn super-nappe (Steck, 1999). The term super-nappe is used, because the nappe can be subdivided, from bottom to top, into the Diablerets, Mont-Gond and Sublage nappes. Similarly to the Doldenhorn nappe, the Morcles nappe is considered as the result of the closure of the North Helvetic basin and the subsequent extrusion of sediments during compressional Alpine tectonics (e.g. Ramsay, 1981; Pfiffner, 1993). This North Helvetic basin comprised kilometer thick sequences of shale-rich units with competent carbonate units in between. Different to the Doldenhorn nappe, the Morcles nappe exhibits less pronounced shearing at its base, a more prominent overturned limb and stronger internal isoclinal folding. The strongly thinned and overturned limb is in contact with the crystalline Aigulles-Rouges massif below and its autochthoneous sediments. Between the Morcles and Wildhorn nappe is a minor sedimentary nappe, the Ardon nappe, which is considered as originating from the horst region, from a similar paleogeographic position as the Jägerchrütz nappe (Figure 3.2). Estimates of metamorphic peak temperatures range between $250°C$ and $380°C$ and therefore support a dominantly ductile deformation regime (Leloup et al., 2005; Boutoux et al., 2016). Furthermore, the deformation of the Morcles nappe is constrained by finite strain measurements. The data highlights a pattern of increasing strain from the front of the nappe towards the root zone and also from the top to the bottom. Strain ellipses show X/Y ratios > 400 at the contact between the overturned limb and the basement-cover (Ramsay and Huber, 1987; Casey and Dietrich, 1997). Microstructural observations of the basal mylonitic shear zone in the overturned limb of the fold nappe indicate ductile creep in the calcite-rich lithologies (Austin et al., 2008). The Wildhorn super-nappe, as a whole, resembles more a thrust sheet but exhibits significant internal deformation. For example, the Diableret nappe is separated from the Mont Gond nappe by an isoclinal fold indicating significant ductile deformation inside the super-nappe.

Due to the topographic Rawil depression, there is no continuous outcrop from the Doldenhorn towards the Morcle nappe. However, geological reconstructions suggest, that the Doldenhorn and Morcles nappes originate from the same, lateral continuous North Helvetic basin and that the Wildhorn nappe and super-nappe result from the same laterally continuous Helvetic basin of the Mesozoic passive European margin (Epard, 1990). The North Helvetic basin is considered absent in the eastern region of the Helvetic nappe system, which explains the

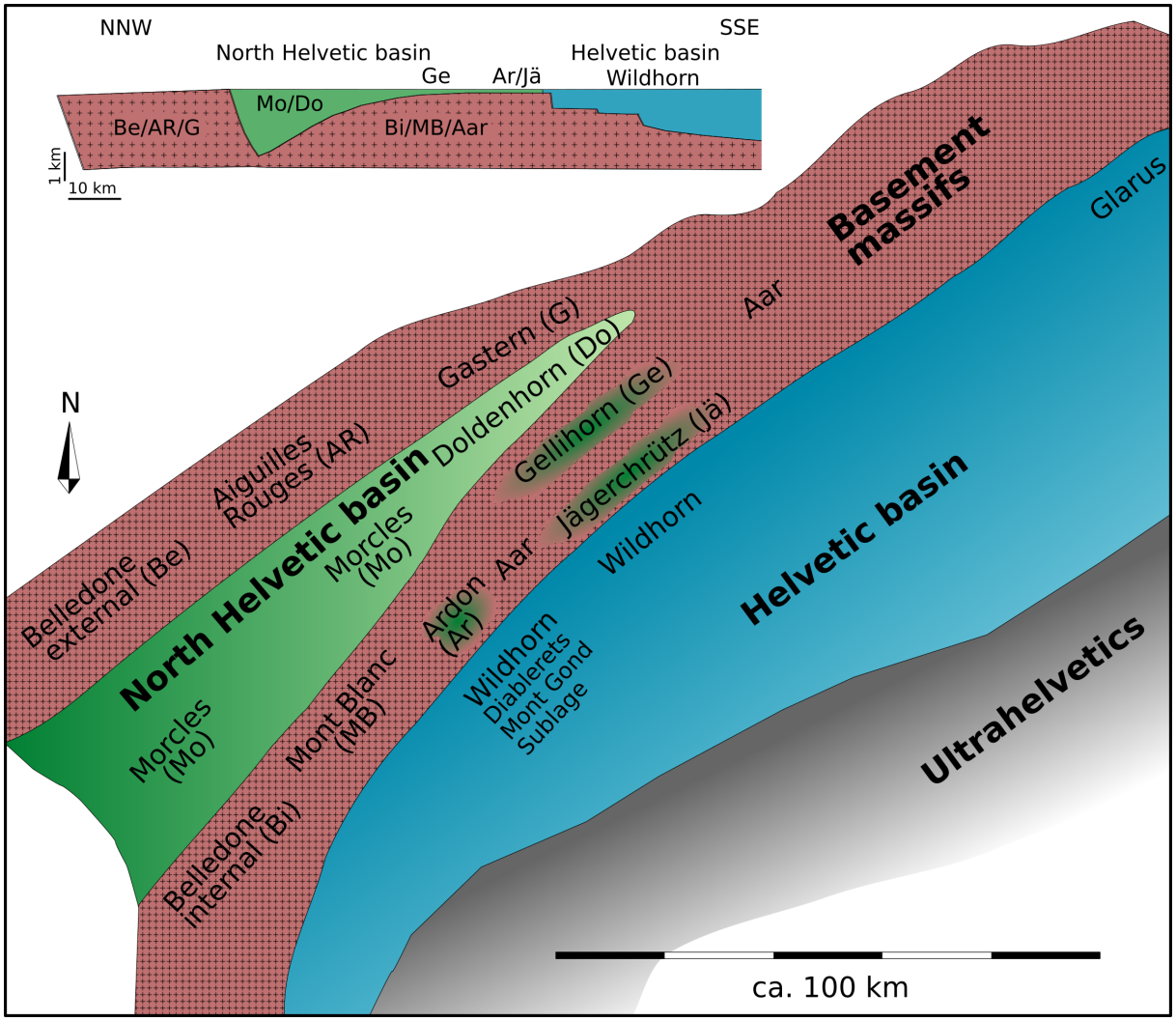

Figure 3.2: Simplified paleogeographic map of the lower cretaceous showing the assumed distribution of the basement massifs and sedimentary units forming the discussed tectonic nappes of the Helvetic nappe system (modified after Epard, 1990 and Pfiffner, 2015). The cross section on the top left represents a section through the SW region across the Helvetic nappe system (modified after Jaquet et al., 2018).

absence of significant nappes in the Infrahelvetic complex below the Glarus thrust. The Doldenhorn nappe can be considered as an intermediate nappe type between a thrust nappe, represented by the Glarus thrust, and a fold nappe, represented by the Morcles nappe.

The fourth section includes also the Morcles nappe and is located in the French Alps (Epard, 1990) (Figure 3.1d). In this section, no Helvetic nappes are outcropping. In contrast to the Morcles fold nappe in the third section, the Morcles nappe is here not a fold nappe but rather a thrust nappe (cp. Figure 3.1c and 3.1d, respectively), because there is no prominent overturned limb. The basement massif is there termed Belledone massif, but the Morcles

nappe in the French region is considered as a geological continuity from the Morcles nappe in the Swiss region (Epard, 1990) (Figure 3.2).

Some studies suggested mechanical explanations for the variation in nappe style within the Helvetic nappe system. The formation of fold nappes in the Southwestern part of Switzerland and the lack of such fold nappes in the Northeastern part is explained by lateral variations of the mechanical stratigraphy, that is the alteration of mechanically strong, such as carbonates, and weak, such as shales, sedimentray units (Pfiffner, 1993; Pfiffner et al., 2011). Different thickness ratios, n, of weak to strong sedimentary units cause a different mechanical response during shortening. Low ratios $n < 0.5$ favor imbricate thrusting and harmonic folding while higher ratios of n favor fold nappes and detachment folding (Pfiffner, 1993). This impact of thickness ratios on deformation style, which was derived by field observations, is also supported by 2D numerical simulations (Jaquet et al., 2014). Moreover, Von Tscharner et al. (2016) quantified, with 3D numerical models of viscous deformation, the impact of laterally varying half-graben depth on the folding of sedimentary layers in the half-graben. Their 3D model results also confirm that laterally varying sediment thickness has a strong impact on fold amplification and nappe formation. However, their models do not generate thrust nappes and also not the stacking of nappes, as observed in the Helvetic nappe system. A comparison of observed finite strain gradients across the Morcles fold nappe with finite strain gradients resulting from a theoretical thermo-mechanical shear zone model utilizing calcite flow laws suggests that the Morcles fold nappe was generated by heterogeneous shearing during Alpine shortening (Bauville and Schmalholz, 2013), as was already suggested by kinematic models (Ramsay et al., 1983; Dietrich and Casey, 1989; Casey and Dietrich, 1997).

3.3 Methods

3.3.1 Numerical method

We apply the concept of continuum mechanics to describe the deformation of rocks with a system of partial differential equations (e.g. Mase, 1970). To solve the resulting system of equations numerically, we apply the 3D thermo-mechanical parallel code LaMEM (Kaus et al., 2016; `https://bitbucket.org/bkaus/lamem`) for our simulations. The equations describing the conservation of mass, linear momentum and energy are:

$$\frac{\partial v_i}{\partial x_i} = 0 \tag{3.1}$$

$$-\frac{\partial P}{\partial x_i} + \frac{\partial \tau_{ij}}{\partial x_j} = \rho g_i \tag{3.2}$$

$$\rho C_p \frac{\partial T}{\partial t} = \frac{\partial}{\partial x_i}\left(\lambda \frac{\partial T}{\partial x_i}\right) + H_R + H_S \tag{3.3}$$

where x_i (i = 1,2,3) refers to Cartesian coordinates in the three spatial directions (i=1 indicates x-direction, i=2 y-direction and i=3 z-direction), v_i are the components of the velocity vector, P is pressure (negative mean stress), $\tau_{ij} = \sigma_{ij} + P\delta_{ij}$ are components of the deviatoric Cauchy stress tensor (with δ_{ij} being the Kronecker delta), ρ is density, $g_i = [0\ 0\ g]$ the gravity acceleration vector with g being the gravitational acceleration, C_p is the specific heat, T the temperature and λ the thermal conductivity. The source term H_R refers to the radiogenic heat production and $H_S = \tau_{ij}\dot{\epsilon}_{ij}$ for shear heating. The components of the deviatoric strain rate tensor $\dot{\epsilon}_{ij}$ are defined by the visco-plastic constitutive equations:

$$\dot{\epsilon}_{ij} = \dot{\epsilon}_{ij}^{vs} + \dot{\epsilon}_{ij}^{pl} = \frac{\tau_{ij}}{2\eta_{eff}} + \dot{\epsilon}_{II}^{pl}\frac{\tau_{ij}}{\tau_{II}} \tag{3.4}$$

where $\dot{\epsilon}_{ij}^{vs}$ is the viscous strain rate tensor, $\dot{\epsilon}_{ij}^{pl}$ is the plastic strain rate tensor, η_{eff} is the effective viscosity, τ_{ij} are components of the deviatoric stress tensor and $\tau_{II} = (\frac{1}{2}\tau_{ij}\tau_{ij})^{\frac{1}{2}}$ is the square root of the second invariant of the deviatoric stress tensor.

The temperature dependent viscosity η_{eff} for the considered dislocation creep is:

$$\eta_{eff} = \frac{1}{2}\left(B_n\right)^{-\frac{1}{n}}\left(\dot{\epsilon}_{II}\right)^{\frac{1}{n}-1} exp\left(\frac{E_n}{nRT}\right) \tag{3.5}$$

where n is the stress exponent, $\dot{\epsilon_{II}} = (\frac{1}{2}\dot{\epsilon_{ij}}\dot{\epsilon_{ij}})^{\frac{1}{2}}$ the square root of the second invariant of the strain rate tensor, B_n the creep constant, E_n the activation energy and R the universal gas constant. The components of the plastic strain rate tensor $\dot{\epsilon}_{ij}^{pl}$ are determined by enforcing the Drucker-Prager yield criterion given by:

$$\tau_{II} \leq \tau_Y = \sin(\phi)P + \cos(\phi)C \tag{3.6}$$

Here, τ_Y is the yield stress, ϕ the friction angle and C the cohesion.

The system of equations is discretized with a staggered grid finite difference approach and solved with LaMEM. Material properties are advected employing a marker-and-cell method. In order to maintain computational stability for large time steps we employ a stabilized free surface boundary condition. For detailed information on the LaMEM code see Kaus et al. (2016) and the documentation on the official website (`https://bitbucket.org/bkaus/lamem`).

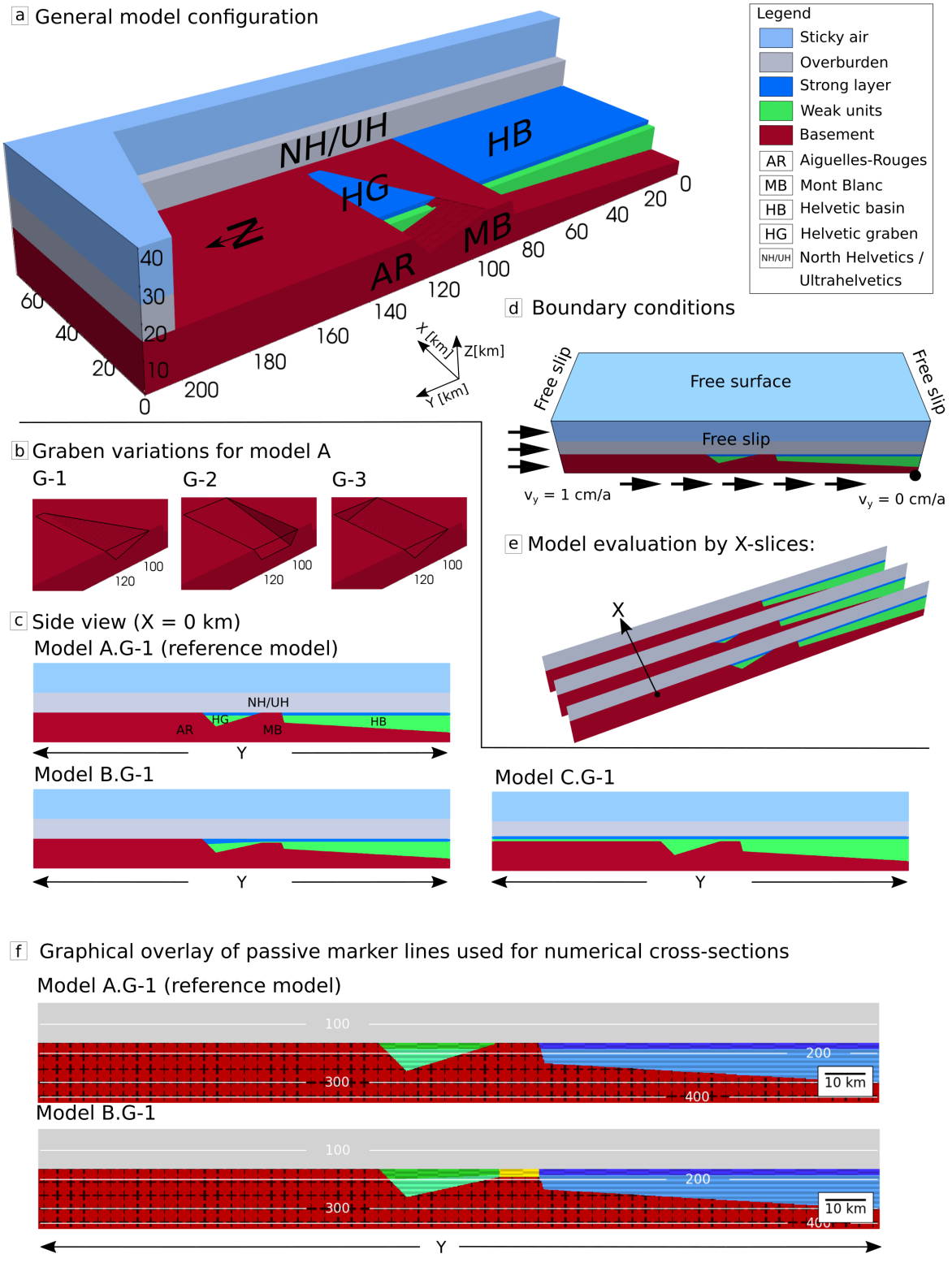
a General model configuration
NH/UH
HB
HG
MB
AR
Z
0
20
40
60
80
100
120
140
160
180
200
10
20
30
40
60
X [km]
Z[km]
Y [km]
Legend
Sticky air
Overburden
Strong layer
Weak units
Basement
AR Aiguelles-Rouges
MB Mont Blanc
HB Helvetic basin
HG Helvetic graben
NH/UH North Helvetics / Ultrahelvetics
d Boundary conditions
Free slip
Free surface
Free slip
Free slip
v_y = 1 cm/a
v_y = 0 cm/a
b Graben variations for model A
G-1
G-2
G-3
100
120
e Model evaluation by X-slices:
X
c Side view (X = 0 km)
Model A.G-1 (reference model)
NH/UH
HG
AR
MB
HB
Y
Model B.G-1
Y
Model C.G-1
Y
f Graphical overlay of passive marker lines used for numerical cross-sections
Model A.G-1 (reference model)
100
200
300
400
10 km
Model B.G-1
100
200
300
10 km
Y

Figure 3.3: a) 3D geometry of our reference model configuration using a laterally disappearing half-graben, and highlighting the distribution of our numerical phases and their material properties. Here, the color *green* refers to weak materials and *dark blue* to strong materials. The configuration is based on the paleogeographic reconstructions as indicated by the abbreviations on the model: AR = Aiguilles Rouges massif, MB = Mont Blanc massif, HB = Helvetic Basin, NH/UH = North Helvetic flysch and Ultrahelvetic units, HG = North Helvetic graben. b) Display of our three different half-graben systems used as initial setup. c) Cross-sectional view at X = 0 km for three models utilizing half-graben G-1 in combination with three different stratigraphic distributions. d) Sketch displaying our boundary conditions. e) 3 cross-sectional slices along X-direction to explain our model evaluation. f) Subfigure highlighting our passive marker overlay which is used to distinguish the different structural units HG (*green*) and HB (*blue*) from each other. Temperature isotherms are shown in $[^{\circ}C]$.

3.3.2 Model configuration

The model configuration (Figure 3.3a) has a lateral width of X = 70 km, a length of Y = 210 km and height of Z = 40 km. Our numerical resolution for most simulations is 128 × 256 × 128 (X × Y × Z) grid points with a mesh refinement in Z-direction using 96 grid points between Z = 8 and 32 km and 16 grid points each for Z < 8 km and Z > 32 km. Our model consists of five units which are, from top to bottom: a sticky air, a cover, a strong layer, a weak unit and a basement unit. Each unit has distinctive mechanical properties, such as for example, a flow law, friction angle, or cohesion that corresponds to natural materials. In addition to the standard parameters of the flow laws we add a pre-factor f to the creep constant B_n to facilitate a brittle-ductile transition zone at a depth of 8−10 km. The details of the mechanical properties for each unit are listed in Table 3.1. The initial model geometry is based on a simplified and idealized cross-section of the European crustal continental passive margin. The basement constitutes the bottom of the model domain and has a maximum height of 15 km. It involves a half-graben (HG) that is separated by a horst from a larger distal basin (HB) to the right (Figure 3.3b). HG represents the half-graben region in which the sediments of the Morcles and Doldenhorn nappes have been deposited, HB represents the Helvetic Basin in which the sediments of the Wildhorn nappe have been deposited and the horst between HG and HB represents the domain on which the sediments of the Ardon and Gellihorn nappes have been deposited (Fig. 3.2). In the reference configuration HG is becoming shallower and finally disappears towards the NE-direction (positive X-direction; Figure 3.3a). The half-graben, between 110 km > Y > 90 km, is subjected to different geometries in our different model configurations with respect to its lateral extend (X-direction). The total dimensions of the graben system are fixed with a maximum depth of 7 km, a length of 25 km (Y-direction) and a width of 50 km (X-direction). In contrast, the geometry of the distal basin (Y < 90 km) is constant and has no variations in the X-direction for all model configurations. Both half-graben and basin are filled with a weak unit, mimicking shale-rich sediments, that is overlain

by a strong layer with a thickness of 1.5 km, mimicking strong carbonates. Additionally, we apply a 10 km thick sediment cover, mimicking the North Helvetic Flysch and Ultrahelvetic units. We assume that these cover unit have been thrust on top of the proto-Helvetic nappe system before the onset of nappe formation. Finally, we use a low density, low viscous sticky air unit ($\eta = 10^{19}\ Pa.s^{-1}$, $\rho = 1\ kg.m^{-3}$) on top to simulate a free surface boundary condition.
In order to investigate the impact of the geometry of HG on the structural evolution of our model we use two different series of simulations. In the first one, we vary the geometry of HG in lateral direction using three different geometries (Figure 3.3b), namely G-1 to G-3. Here, we also define our reference model A.G-1. It compromises HG, G-1, that linearly shallows and narrows out in lateral X-direction. The next configuration, G-2, is HG without lateral geometrical variations, which is bounded by a 90° wall to the adjacent basement. Our third configuration, G-3, is HG being a full graben that shallows out in lateral direction while the length in Y-direction is constant.
In the second series (Figure 3.3c) we employ the same HG as in the reference configuration, G-1, but modify the spatial connection between the strong layer and the underlying basement. In model B.G-1 we decrease the height of the horst in such a way that the strong layer and a part of the weak unit rests on the top of the horst. Additionally, we also thicken the left part of the strong layer which is connected to the basement in a wedge like shape (Figure 3.3c). In the last model, C.G-1, we extend the strong layer to the left of the HG (Figure 3.3c). For C.G-1, the layer is not connected with the basement, but underlain by an additional 0.5 km thick layer of weak units (Figure 3.3c).
To test the impact of the vertical strength distribution in the basement, we performed an additional simulations, D.G-1, with the same configuration as the reference model, A.G-1, but we cut-off the deviatoric stresses in the basement at 40 MPa. Numerically, this is done by setting the cohesion in the basement to 40 MPa and setting the friction angle to zero. Such yield criterion corresponds essential to a pressure-insensitive von Mises yield strength and mimics a semi-brittle deformation, or a low temperature plasticity.
We apply free slip boundary conditions on all sides of the model except on the top where we model a free surface boundary condition with the sticky air method (Figure 3.3d). In order to mimic the kinematic conditions during tectonic wedge formation, we apply a constant velocity boundary condition on the bottom face and the left XZ-face of our model (Figure 3.3d). We induce bulk shortening of the model by moving the left boundary and the bottom boundary in positive Y-direction with a constant velocity of $v_y = 1\,cm/yr$. This boundary condition is similar to typical sandbox analogue models of accretionary wedge formation. The bulk shortening strain rate $\dot{\epsilon}_{bg}$ is recalculated from the velocity boundary condition for every time step. The shortening of the model in Y-direction is balanced by an elongation in Z-direction, with no changes of the width in X-direction.

We use a linear, vertical temperature gradient of $16.6°C/\text{km}$ with a fixed temperature of $20°C$ at the surface and $435°C$ at the bottom of the model. The heat flux through all vertical model sides is zero. Furthermore, we use passive marker lines and patterns to improve the visualization of 2D cross-sections of our 3D model (Figure 3.3f). Also , we slightly change the color scheme to highlight the two major basement structures HG and HB, together with the sediments on top of the basement horst (*yellow*). The darker colors inside the HG and HB indicate the strong layer while the lighter colors correspond to the weak units. The layering and patterns are passivley advected with the numerical velocity field. Hence, they do not influence the material properties and deformation and are simply there for visualization purposes.

Table 3.1: Table listing the material properties of our model units for most models, where ρ is the density, A is the pre-exponential factor, f is custom pre-factor, n is the power-law exponent, Q is the activation energy, λ is the thermal conductivity, ϕ is the friction angle, and C is the cohesion. Some additional parameters are constant: Here the thermal expansion coefficient $\alpha = 3 \times 10^{-5}\ K^{-1}$, the heat capacity $C_p = 1050\ J.K^{-1}$ and the radiogenic heat production $Q_r = 10^{-6}\ W.m^{-3}$. We use following creep flow laws: [1]Schmid et al. (1977),[2]Hansen et al. (1983),[3]Kronenberg et al. (1990).

Model unit	$\rho\ [kg.m^{-3}]$	**Rheology**	f	A$[Pa^{-n}.s^{-1}]$	n	Q $[J.mol^{-1}]$	$\lambda[W.m^1K^{-1}]$	ϕ [°]	C [MPa]
Cover	2750	Calcite[1]	0.1	1.58×10^{-25}	4.2	4.45×10^5	2.0	30	1
Strong layer	2750	Calcite[1]	1.0	1.58×10^{-25}	4.2	4.45×10^5	2.5	30	1
Weak units	2750	Mica[2]	1.0	1×10^{-138}	18.0	5.10×10^5	2.5	5	1
Basement	2800	Granite[3]	1.0	3.16×10^{-26}	3.3	1.87×10^5	3.0	30	10

3.4 Results

3.4.1 3D model evolution

We first provide an overview of the general model evolution of all six performed 3D simulations. Figure 3.4 shows the structural evolution for three different bulk shortening for each model configuration. All models, except model C.G-1 (Figure 3.3c), show the formation of nappe-type structures in the strong layers and stacking of the strong layer from HB on top of the strong layer of HG. Model C.G-1 does not generate any nappe-like structure or overthrusting, but generates detachment folds.

In the first stage of our reference model A.G-1 (Figure 3.4a) the strong layer of HB is detached from the horst by the formation of a shear zone. Both the strong layer and the weak units below are thrusted on top of the horst culminating in a horizontal displacement of about 10 km. Our model generated a structure resembling a thrust sheet or thrust nappe. The HB experiences closure. In the region of HB, the weak sediments and the basement are thickened with ongoing bulk shortening. Initially, the basement experiences an uplift at the right boundary due to the imposed velocity discontinuity. The basement uplift increases the topography at the right boundary of the model (i.e. the backstop). The HG shows minor

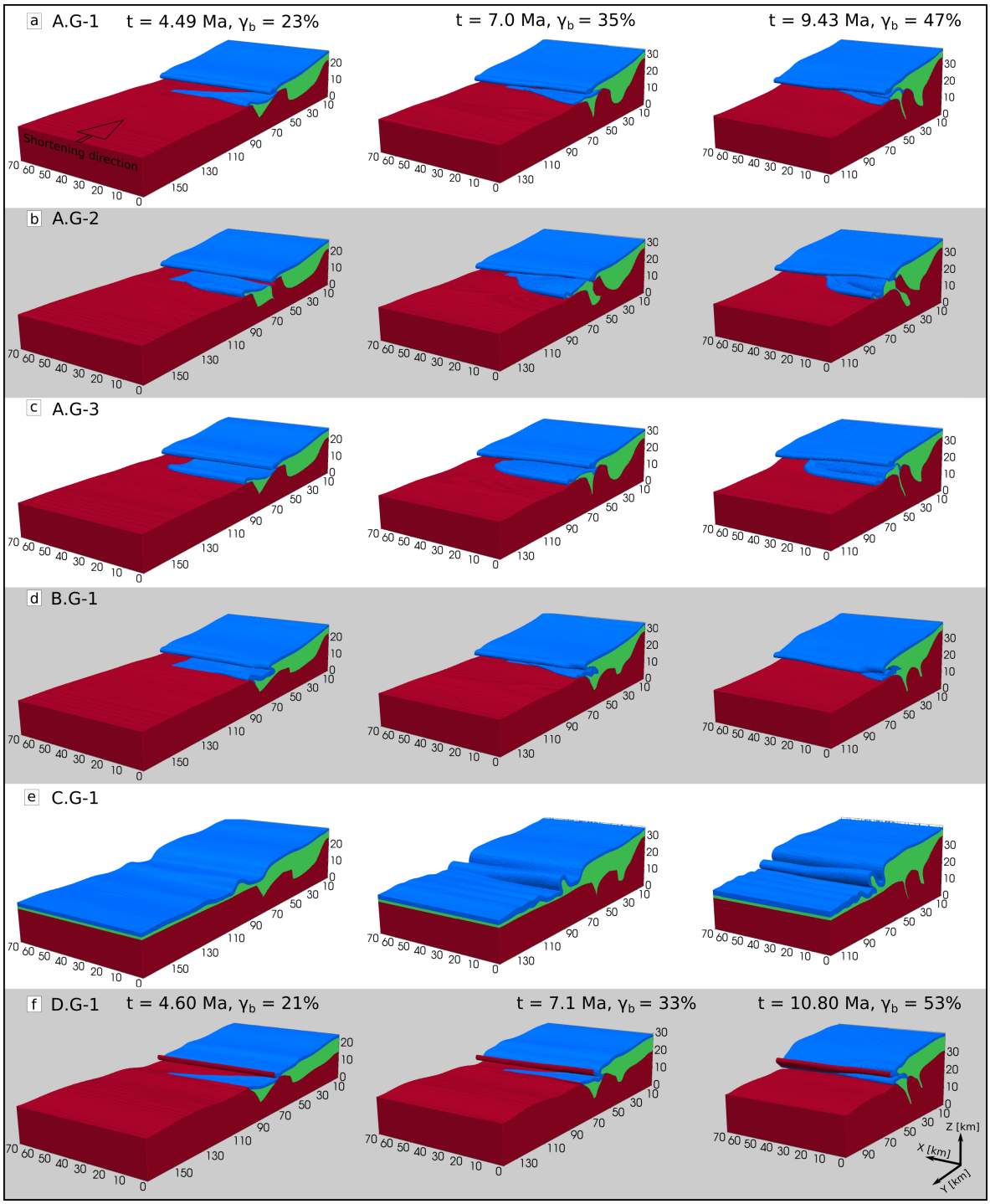

Figure 3.4: 3D model evolution for our six simulations, using a graphical threshold to highlight the deformation of the strong layer, weak units and the basement. Rows correspond to the configuration and columns to the total bulk shortening γ_b.

signs of deformation at 23%. The strong layer is partially sheared and squeezed out in front of HG. Additionally, we observe a slight depression of the strong layer in the rear of HG. In the next shortening stage, (Figure 3.4b) the closure and inversion of HG is in progress. The strong layer has been squeezed out of HG. The horizontal displacement of the strong layer of HG decreases in positive X-direction associated with decreasing depth of HG. Furthermore, the thrust nappe from HB has advanced on top of HG and the horst exhibits a dome-like shape. At 47 % bulk shortening (Figure 3.4c), the half-graben is almost completely closed resulting in the formation of a elongated cusp dipping towards the backstop. The infill of HG has been extruded and compromises a nappe that is overthrust by a nappe from HB. The front of the nappe from HB is essentially straight along the lateral, X-direction, indicating that the displacement of the nappe is essentially unaffected by the formation of the nappe below, whose front varies significantly along the X-direction. We only observe a slightly higher topography above the nappe from HG, causing a slight tilting of the nappe from HB towards the positive X-direction.

Model A.G-2 (Figure 3.4b) deviates in the structural evolution from model A.G-1. At 23 % bulk shortening (Figure 3.4b), the strong layer of HG is displaced more out of HG than for model A.G-1. The basement horst is slightly sheared towards the left, that is against the shortening direction. This shearing of the horst increases with progressive bulk shortening. At 47 % bulk shortening (Figure 3.4b) the HG is nearly closed at its top, but the closure of the HG did not form a cusp, as for model A.G-1. In contrast, the sediments still in the HG become thicker with depth, because for the considered geometry of the HG it is more difficult to squeeze out all the sediments (Figure 3.4b). The strong layer of HG has been completely detached from the horst showing a higher slope in front of the extruded sediments. Overall, this model shows a significantly higher degree of basement involvement, with the up doming horst separating the nappe from HG from the thrust nappe from HB. Nevertheless, the front of the nappe from HB was displaced in the same uniform manner as in the reference model, A.G-1.

Model A.G-3 displays a similar evolution as model A.G-1 (Figure 3.4c). The geometry of HG results in a almost straight front of the squeezed out strong layer. There is a slight curvature at the lateral boundary between the lateral end of HG and basement (Figure 3.4c). The final stage (Figure 3.4c) shows a nappe originating from HG that is almost homogeneous in lateral X-direction. However, even though the depth of the half-graben is constant up to X = 50 km there is a notable decrease of nappe height from X = 30 to 50 km. This tilting of the nappe front towards the positive X-direction can be explained by the adjacent basement, which might affect the degree of half-graben closure due to the strength contrast between the sediment and basement units. At 47 % bulk shortening (Figure 3.4c) the nappe from HB did not fully thrust over the fold nappe.

Model B.G-1 (Figure 3.4d) exhibits a continuous strong layer from HG to HB across the horst, but has the same geometry of HG than reference model A.G-1. At 23 % bulk shortening (Figure 3.4d) we observe a similar deformation of the strong layer at HG than in model A.G-1. However, a larger amount of weak sediments from HB is displaced across the horst against the shortening direction. At 35 % bulk shortening the HG is less closed that for the same bulk shortening of the reference model (Figure 3.4d). Inside the initially continuous strong layer, a shear zone develops that forms a nappe of sediments from the region of the HB. At 47 % bulk shortening (Figure 3.4d) two nappe structures have formed; one consisting of sediments from HG and a structurally higher one consisting of sediments from HB. The two nappes are also stacked. However, in this model the strong layer has no connection anymore to the horst.
Model C.G-1 (Figure 3.4e), with a strong layer resting above the entire basement, shows detachment folding. The lateral variations in basement geometry are not significant enough to generate a shear zone in the strong layer, which eventually would form a nappe structure. The deformation of the basement and HG is similar to model B.G-1. The detachment fold with the largest amplitude originates from the region of HG (Figure 3.4e). With progressive shortening, this detachment fold is displaced across the basement against the direction of shortening (Figure 3.4e).
In model D.G-1 (Figure 3.4f), with a stress cut-off in the basement at 40 MPa, the shortening is more homogeneously distributed in the basement, so that during the initial stages of shortening (23 %; Figure 3.4f) the basement at large distance from the backstop is already thickened. Consequently, the basement uplift around the backstop is significantly lower compared to all other models. Furthermore, during nappe formation some parts of the uppermost basement are also sheared-off from the basement. The nappe forming from the strong layer of HG resembles a fold nappe.

3.4.2 2D numerical cross sections

We discuss the deformation in the 3D models by analyzing six 2D cross sections parallel to the shortening direction (Y-direction) but at six different location along the lateral X-direction (Figure 3.5). The six cross sections are located along the lateral direction from X = 0 km to X = 50 km with 10 km spacing.
For the reference model A.G-1 (Figure 3.5) at 23% shortening (Figure 3.5, left column), the sediments from HB have been detached from their original position and thrusted across the basement horst all along the lateral direction (everywhere in the left column of Figure 3.5). The displaced sediments from HB resemble a thrust nappe. Around the backstop (right side) there is significant basement uplift. The cross sections show, from top to bottom, the shallowing and disappearance of HG. The strong layer is already sheared-out of HG, whereby the horizontal displacement is larger for deeper HG. Both nappes originating from HB and HG are deforming at the same time. The temperature around the top of the horst is ca. $300°C$.

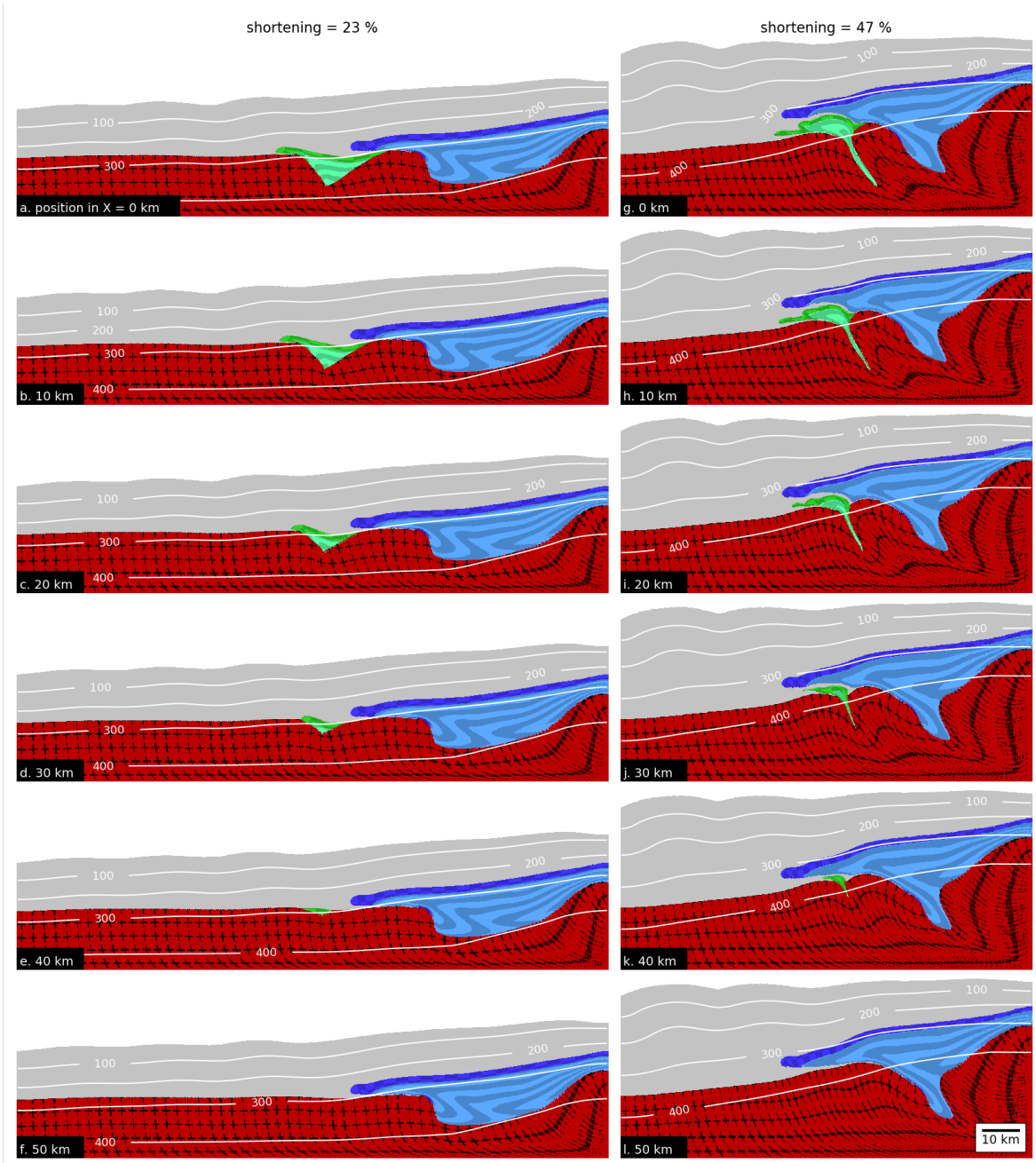

Figure 3.5: Graph showing lateral cross-sections for two different states of bulk shortening for the geometrical evolution of model A.G-1. Cross-sections are taken in 10 km steps from X = 0 km to X = 50 km. Additionally we display the isothermal lines in degree Celsius [$°C$]. Columns correspond to the bulk shortening state and rows to cross-section X-position.

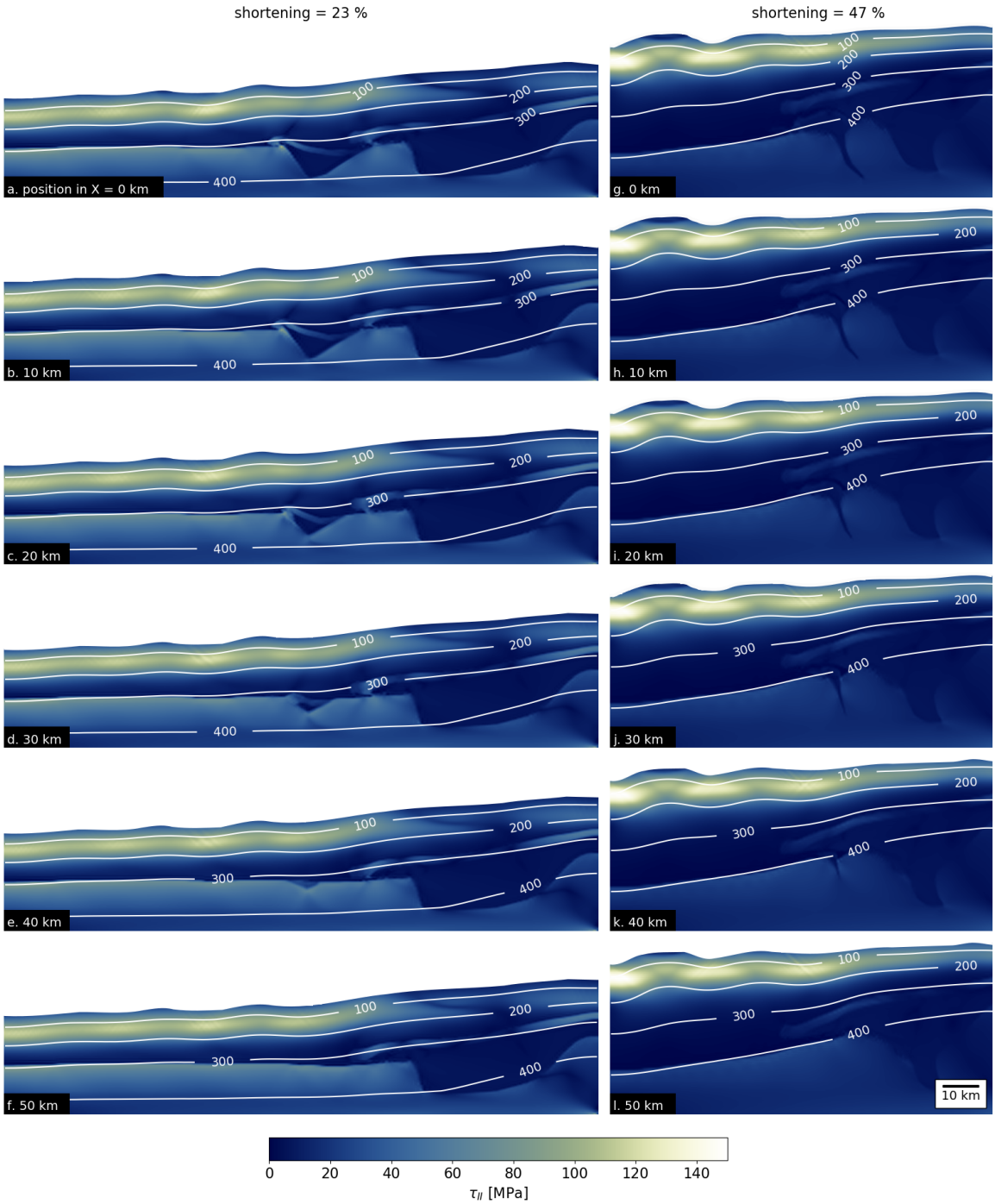

Figure 3.6: Graph showing lateral cross-sections for two different states of bulk shortening for the second invariant of the deviatoric stress τ_{II} of model A.G-1. Cross-sections are taken in 10 km steps from X = 0 km to X = 50 km. Additionally we display the isothermal lines in degree Celsius. Columns correspond to the bulk shortening state and rows to cross-section X-position.

The passive marker lines in the weak sediments of HB indicate ductile flow generating passive shear folds. In the basement the passive marker symbols ('crosses') indicate an increase in shear strain from the top to the bottom of the basement due to decrease in basement viscosity associated with a temperature increase. At 47% bulk shortening (Figure 3.5g-l, right column) the nappe from HB is thrust completely above the nappe from HG. The HG has been almost closed with the weak sediments residing now inside a cusp between the neighboring basement units, which dips towards the backstop. In the deeper region of HG the passive markers in the weak sediments indicate a fold nappe structure. The very frontal part of the nappe from HG resembles a thrust nappe, formed exclusively by the strong layer, whereas the main part of the nappe, including also the weak sediments, resembles a fold nappe (Figure 3.5g-i). Between the upper nappe from HB and the lower nappe from HG are cover sediments that have been dragged between the two nappes during overthrusting of the nappe from HB (Figure 3.5g-k). The nappe from HG disappears in lateral direction with the disappearance of HG. For the cross section without HG (Figure 3.5l) there is only a nappe from HB resembling a thrust nappe. Despite the significant lateral variation of the depth of HG and the associated lower nappe, the horizontal displacement of the upper thrust nappe is essentially the same along the lateral direction. Consequently, nappe formation of sediments from HG does not affect the horizontal displacement of the overthrusting nappe from HB. The horst exhibits a significant internal deformation in the regions with a deep HG, indicated by the passive marker symbols. The temperature isotherms are affected by the deformation and thickening of the model. Generally, the sediments are getting hotter during the deformation. At 23% bulk shortening the strong layer of HG has a temperature of ca. $300°C$ while the temperature of the strong layer of HB is less than $300°C$. At 47% bulk shortening the isotherms indicate that both strong layers were heated by ca. $50°C$.

Additionally to the cross sections showing the structural and thermal evolution of model A.G-1, we display the same cross sections but indicating the magnitude of the deviatoric stress invariant, τ_{II}, to quantify the state of stress (Figure 3.6). The largest stress is ca. 140 MPa and occurs at the brittle-ductile transition in the cover, in a depth of ca. 5 km. At 23% bulk shortening (Figure 3.6a-f) the top of the basement exhibits τ_{II} values between 40 MPa and 80 MPa. After 47% bulk shortening τ_{II} values in the basement are strongly decreased, down to 10 MPa to 20 MPa, due to the increase of basement temperature. Overall, there are no considerable lateral variations in τ_{II}.

The cross-sections for model A.G-2 indicate overall a similar structural evolution as our reference model (Figure 3.7) in the sense that the sediments are sheared-out of HG and HB, form nappe-like structures and are piled at 46% bulk shortening. However, the different initial geometry of HG also generates differences in the structural evolution: At 23% bulk shortening the nappe from HB is less displaced across the horst for a deeper HG. The reason is that due to the different geometry of HG, the basement horst is also significantly sheared towards the

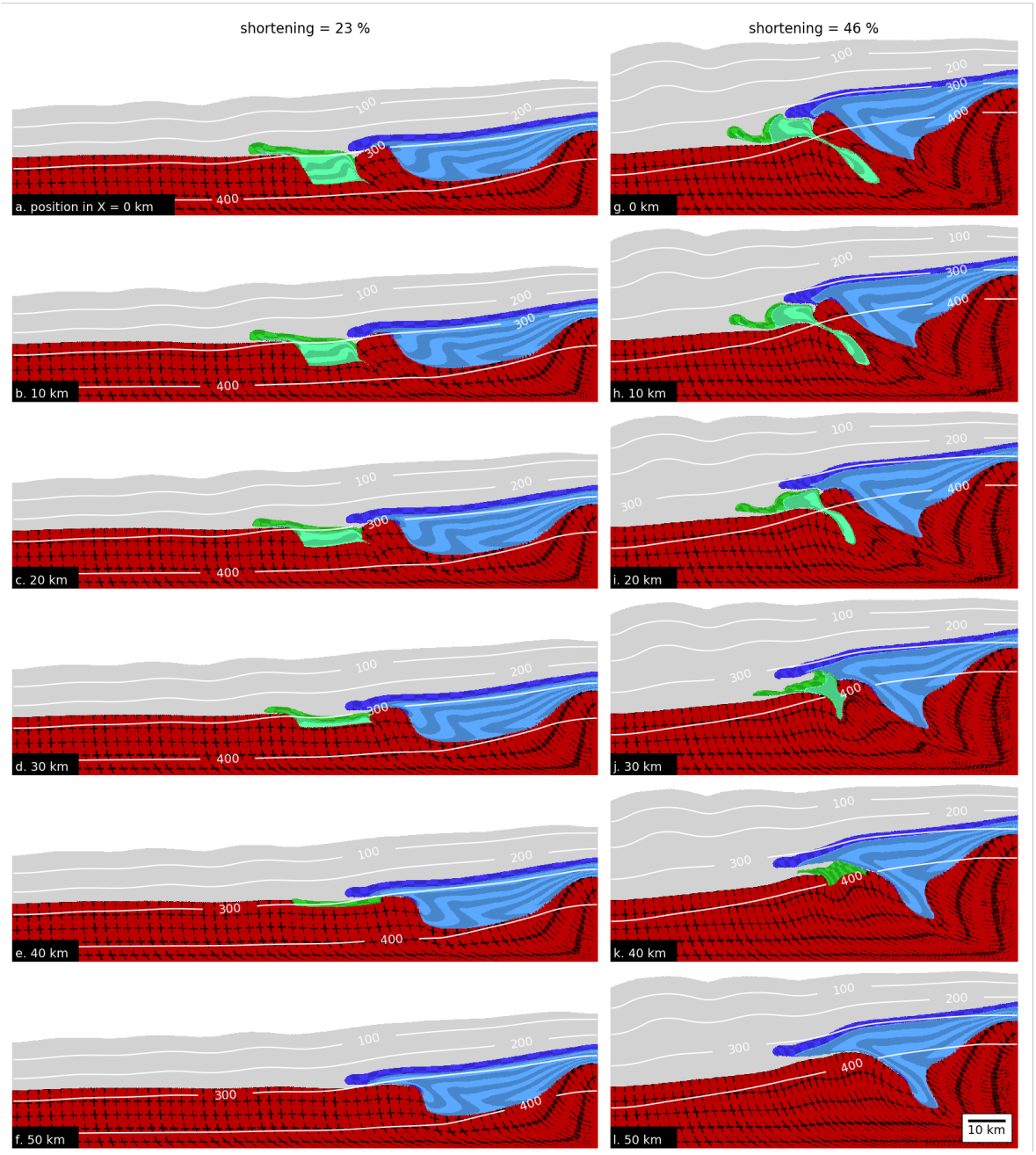

Figure 3.7: Graph showing lateral cross-sections for two different states of bulk shortening for the geometrical evolution of model A.G-2. Cross-sections are taken in 10 km steps from X = 0 km to X = 50 km. Additionally we display the isothermal lines in degree Celsius [$°C$]. Columns correspond to the bulk shortening state and rows to cross-section X-position.

left model side and represents, hence, a less stiff obstacle for a deep HG. Therefore, both the nappe from HB and the horst are sheared together towards the left model side. For a shallower HG, the horst represents a mechanically stiffer obstacle for the nappe from HB and, hence, the nappe is overthrust more to the left. At 46% bulk shortening (Figure 3.7g-l) we also observe extrusion of sediments from HG, but for the deepest regions of HG a significant amount of the sediments remains trapped between the basement at depth. Around the region where HG is deepest, the horst is sheared significantly and even sheared slightly on top of the basement that was initially to the left of HG (Figure 3.7g-i). The strong layer from HG is essentially disconnected from the horst and a significant part of this strong layer resembles more a thrust nappe. The temperature evolution of model A.G-2 is similar to the one of the reference model. The results indicate that the geometry of HG has a strong impact of the structural evolution of the nappes and the basement, although the first order structural evolution is similar to the reference model.

Model A.G-3 (Figure 3.8) shows a similar structural evolution as the reference model. The main difference can be observed in the cross section located at the lateral boundary of HG at X-position 50 km (Figure 3.8l). There, sediments of HG have been extruded laterally out of HG, which can be seen by a pocket of sediments inside the basement.

Model B.G-1 (Figure 3.9) shows a different nappe evolution than model A.G-1. At 23% bulk shortening (Figure 3.9a-f) in the region where the horst is overlain by weak sediments and a strong layer (*yellow*), the strong layer is sheared off the horst and pushed across HG by the strong layer from HB (Figure 3.9a). In the region where the horst is overlain only by the strong layer (*yellow*), the strong layer is continuously sheared and dragged by the sediments from HB (Figure 3.9b). The degree of shearing decreases with decreasing thickness of the yellow layer (Figure 3.9b-d). At 47% bulk shortening, HG is also almost closed and nearly all sediments have been squeezed out (Figure 3.9g-f). At X = 0 km (Figure 3.9f) the strong layer is completely detached from the basement. The layer initially resting on the horst has been sheared above the sediments from HG and is itself overthrust by the sediments from HB. This structure resembles the vertical stacking of three nappes whose sediments were originally horizontally next to each other. With decreasing thickness of the strong layer from the horst, its shearing across the sediments from HG is also decreasing (Figure 3.9i-k). Despite a horizontally continuous strong layer from HG to HB, a major shear zone developed in the strong layer and caused the generation of a nappe-like structure. The shear zone development inside the strong layer is only due to the geometrical variation of the underlying basement, because the strong layer has homogeneous material properties.

Model C.G-1, with a continuous strong layer across the entire model domain (Figure 3.10), shows a very different evolution compared to the reference model, because no prominent shear zones form in the strong layer, which could develop a nappe-like structure and significant overthrusting.

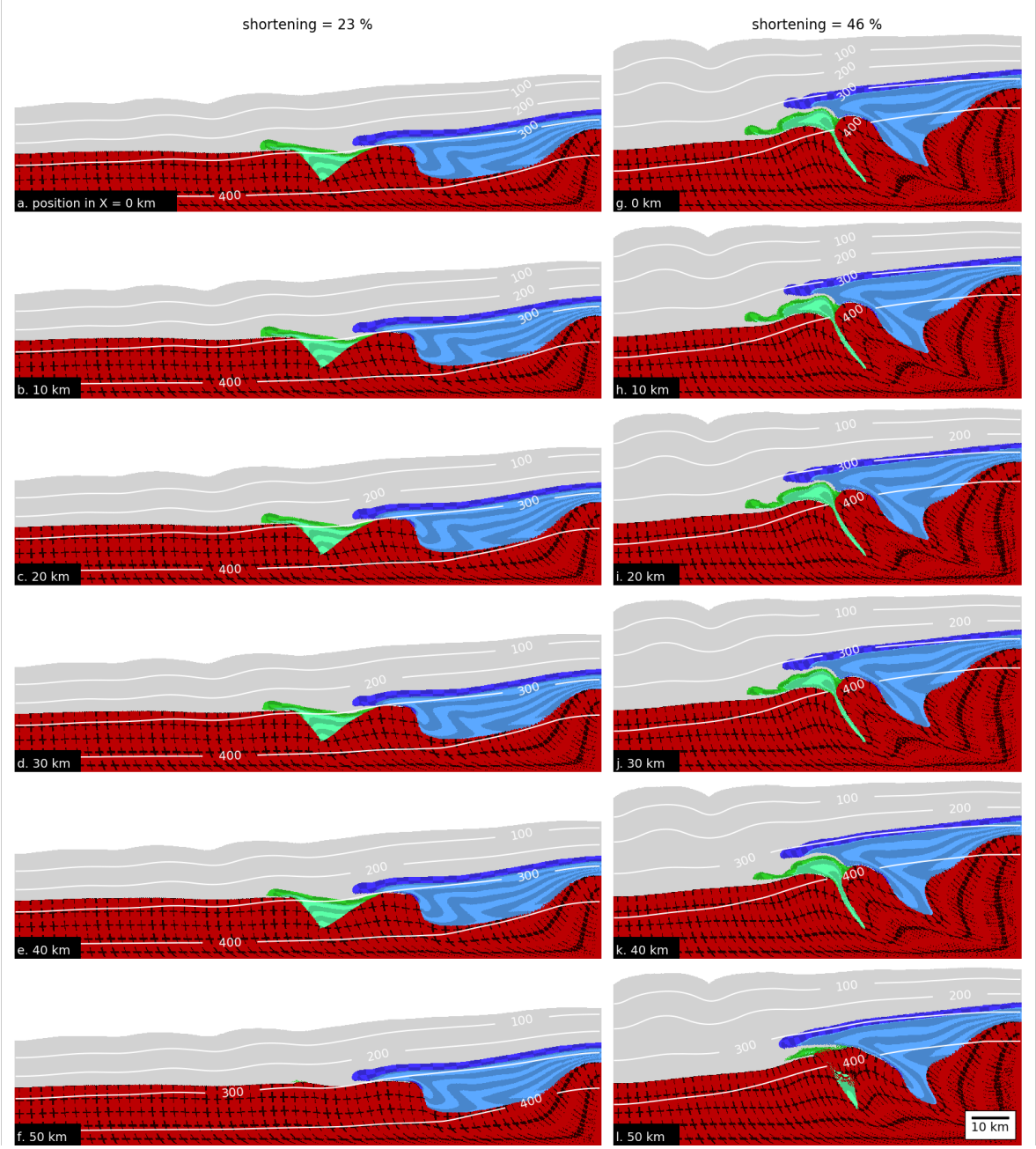

Figure 3.8: Graph showing lateral cross-sections for two different states of bulk shortening for the geometrical evolution of model A.G-3. Cross-sections are taken in 10 km steps from X = 0 km to X = 50 km. Additionally we display the isothermal lines in degree Celsius [$°C$]. Columns correspond to the bulk shortening state and rows to cross-section X-position.

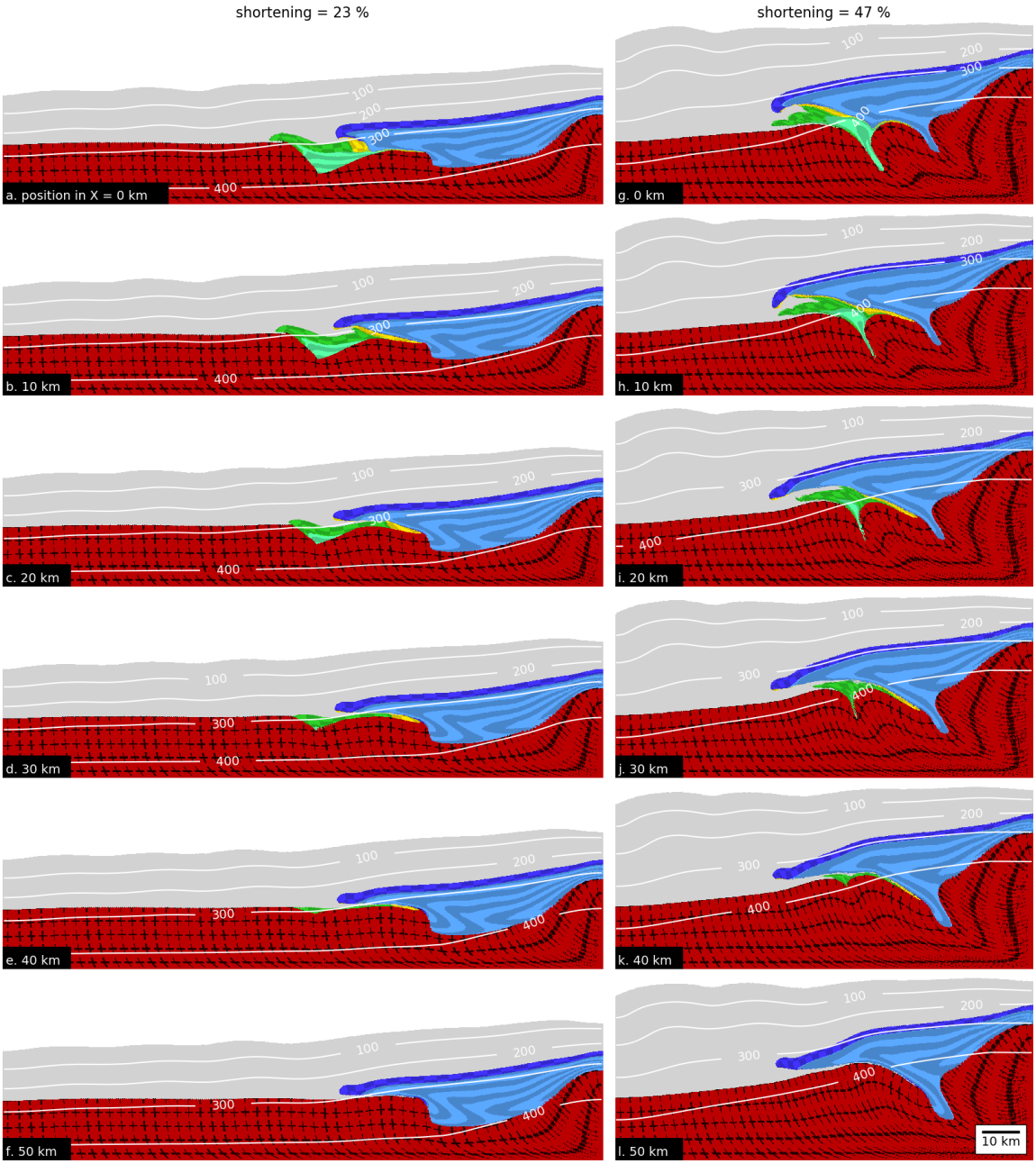

Figure 3.9: Graph showing lateral cross-sections for two different states of bulk shortening for the geometrical evolution of model B.G-1. Cross-sections are taken in 10 km steps from X = 0 km to X = 50 km. Additionally we display the isothermal lines in degree Celsius [$°C$]. Columns correspond to the bulk shortening state and rows to cross-section X-position.

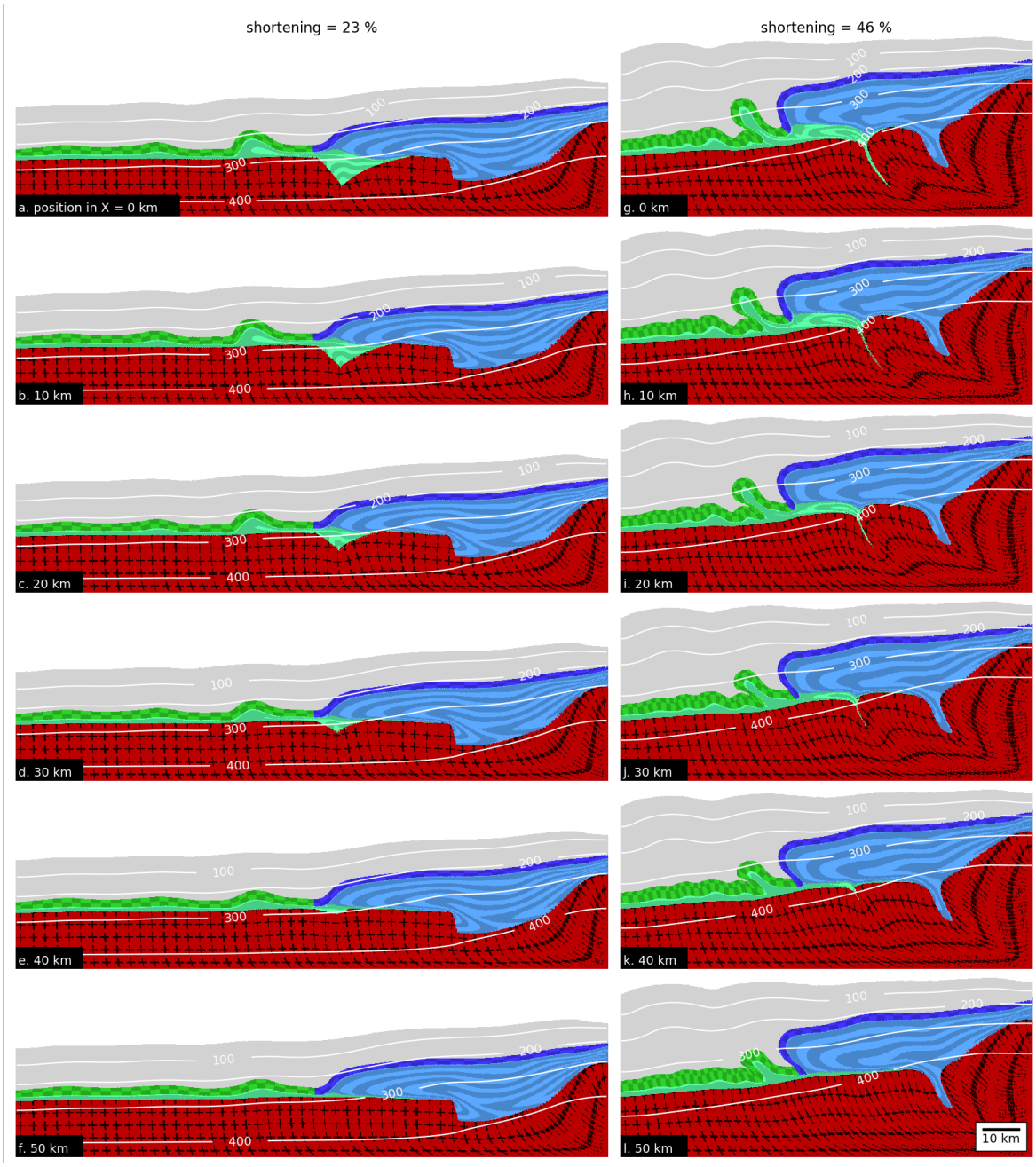

Figure 3.10: Graph showing lateral cross-sections for two different states of bulk shortening for the geometrical evolution of model C.G-1. Cross-sections are taken in 10 km steps from X = 0 km to X = 50 km. Additionally we display the isothermal lines in degree Celsius [$°C$]. Columns correspond to the bulk shortening state and rows to cross-section X-position.

The strong layer initially above HG develops a detachment fold. At 23% bulk shortening (Figure 3.10a-f) this detachment fold already shows a great variability in amplitude in lateral X-direction of the model. During the initial stages of folding, the core of this fold was filled with half-graben sediments and progressively displaced towards the left where the basement top is horizontal (Figure 3.10a-e). In the region without half-graben, only a small amount of weak sediments was available to fill the fold core so that considerable amplification was inhibited (e.g. cp. Figure 3.10f and a), as is the case for detachment, or décollement, folding (e.g. Epard and Groshong Jr, 1993; Schmalholz et al., 2002; Butler et al., 2019). During bulk shortening, the detachment fold is displaced across the basement towards the left. The HG is also closed after 47% bulk shortening (Figure 3.10g-j). Similarly to the other models the weak half-graben sediments have been extruded and some of these sediments have filled the core of the detachment fold. The green marker lines in Figure 3.10g indicate that the fold was continuously fed by the half-graben sediments during ongoing deformation. Hence, the amplitude of the largest individual fold decreases towards the model side without a half-graben (Figure 3.10g,l). The strong layer initially from HB forms a thick nappe-like structure with a slightly overturned layer at the front. However, no overthrusting above the sediments from HG occured.

Compared to the reference model, model D.G-1 (Figure 3.11) shows only a minor basement uplift at the right boundary at 21% bulk shortening (Figure 3.11a-f). Instead, the bulk shortening is distributed more homogeneously throughout the basement, resulting in significant thickening also in the basement on the left model side. Because the top of the basement is weaker, the strong layers can shear-off and displace slices of the basement (e.g. Figure 3.11a). Further bulk shortening results in the extrusion from sediments from HG resulting in a structure resembling a fold nappe. This fold nappe is overthrust from the sediments from HB, resembling a thrust nappe (Figure 3.11g-l). The last deformation stage is shown for 53% bulk shortening, because $6-7$% more bulk shortening is required to overthrust the sediments from HB, compared to the reference model. The strong layer from HG forming the fold nappe exhibits an overturned limb that is still in contact with the basement. Thus, this model does not form any structure similar to a thrust nappe for the sediments from HG. The passive marker symbols show gentle folding of the basement, also on the model side without half-graben (Figure 3.11l). In contrast, the reference model (Figure 3.5l) exhibits updoming of the basement without well developed folding.

3.4.3 Nádai strain and Lode's ratio

We compute the Nádai strain ε_s (Nádai and Hodge, 1963) and Lode's ratio ν (Lode, 1926) for our simulations, which are two quantities to quantify 3D finite strain. Both parameters are computed from the natural logarithm of the finite strain principal axes, ϵ_1, ϵ_2 and ϵ_3. The

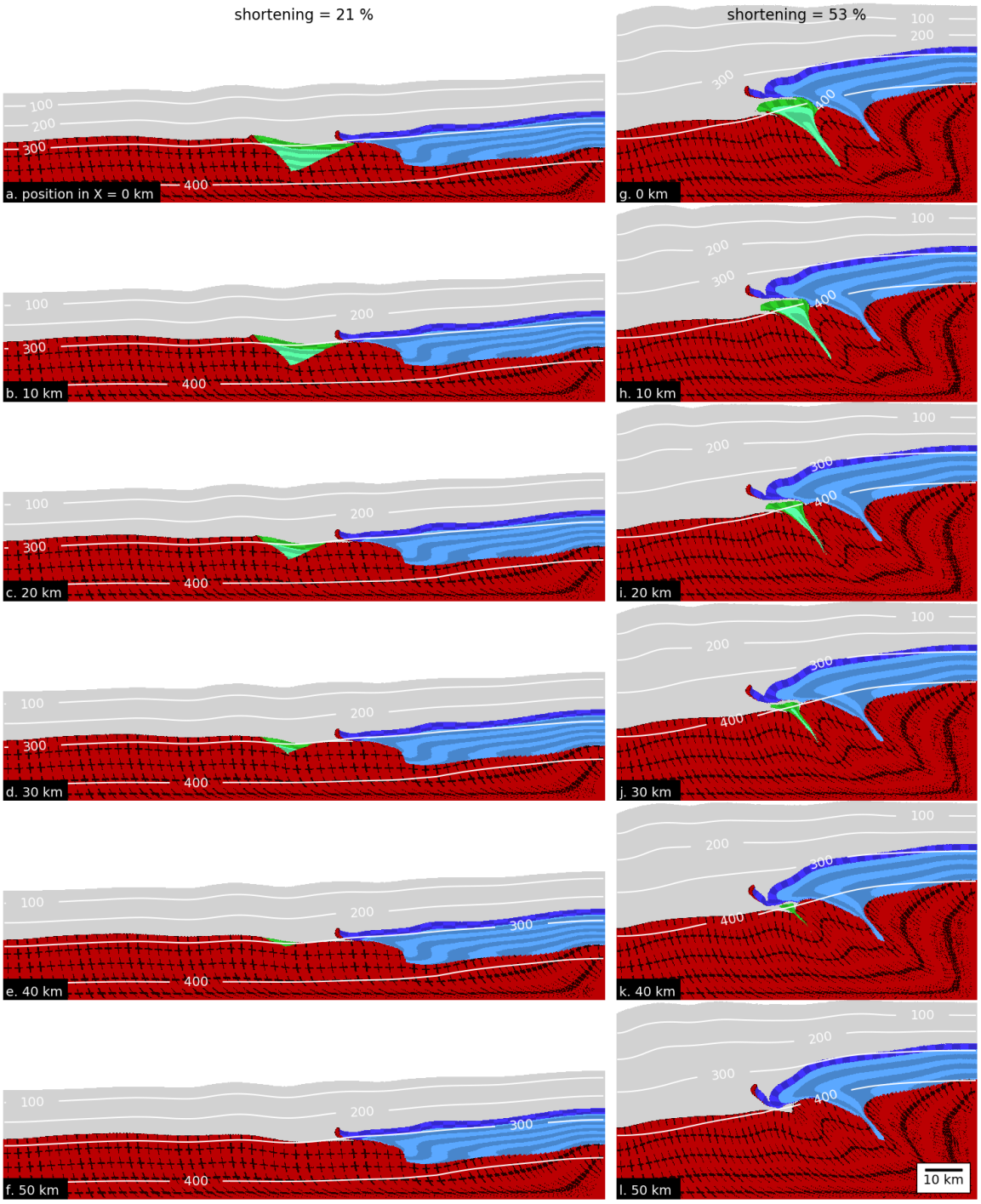

Figure 3.11: Graph showing lateral cross-sections for two different states of bulk shortening for the geometrical evolution of model D.G-1. Cross-sections are taken in 10 km steps from X = 0 km to X = 50 km. Additionally we display the isothermal lines in degree Celsius [$°C$]. Columns correspond to the bulk shortening state and rows to cross-section X-position.

Nádai strain ε_s is the octahedral shear strain and provides a non dimensional value for the strain magnitude:

$$\varepsilon_s = \frac{1}{\sqrt{3}}\sqrt{(\varepsilon_1 - \varepsilon_2)^2 + (\varepsilon_2 - \varepsilon_3)^2 + (\varepsilon_3 - \varepsilon_1)^2} \tag{3.7}$$

The Lode's ratio provides information on the strain symmetry and strain regime and can exhibit values in the interval of $[-1\ 1]$. In particular, $\nu < 0$ indicate a prolate strain ellipsoid (constrictional strain), $\nu = 0$ a prolate-oblate strain ellipsoid (plane strain) and $\nu > 0$ an oblate strain ellipsoid ellipsoid (flattening strain):

$$\nu = \frac{2\varepsilon_2 - \varepsilon_1 - \varepsilon_3}{\varepsilon_1 - \varepsilon_3} \tag{3.8}$$

We display both quantities for model A.G-1 (Figure 3.12) for three different cross-sections, which provides a representative image of the finite strain distribution also for the other models. The first section is taken at the maximum depth of HG (X = 0 km), the second at half of the depth (X = 25 km), and the last at the section where the half-graben disappears (X = 50 km). In general, ε_s values are highest on the right side on top of the basement horst, ranging between 3.5 to 4. The extent of this shear zone, for the same intensity, changes laterally with changing depth of HG. For example, the shear zone roots much deeper into the basin on the side without HG (cp. Figure 3.12a-c). Moreover, ε_s outlines the fold nappe structure indicating that the fold nappe is surrounded by highly strained material. Here, maximal values of ε_s increase laterally with decreasing depth of HG. Another lateral difference is the intensity of the shear zone located on the left side of the model in front of the extruded sediments. This shear zone also gains intensity in lateral direction with decreasing half-graben depth. Similarly to ε_s the, Lode's ratios ν (Figure 3.12d-f) pinpoint the shear zone on top of the horst and outline the fold nappe.

Overall, ν values are close to zero which indicates a plane strain deformation. The largest deviations from plane strain are located in the cross section of maximum depth of HG (Figure 3.12d). Furthermore, values around the fold nappe in the range of 0.5 imply a flattening regime. In contrast, the shear zone at the rear of the basement horst displays negative values that are in the order of -0.2 to -0.5, indicating a constrictional deformation.

3.5 Discussion

3.5.1 Impact of lateral geometry variations and rheological layering

Our models show the detachment of sedimentary units and their subsequent horizontal transport. Depending on the model configuration, the sedimentary units resemble fold or thrust nappes. The strain localization necessary to detach the sedimentary units and to transport them horizontally without significant internal deformation occurred without any mechanical

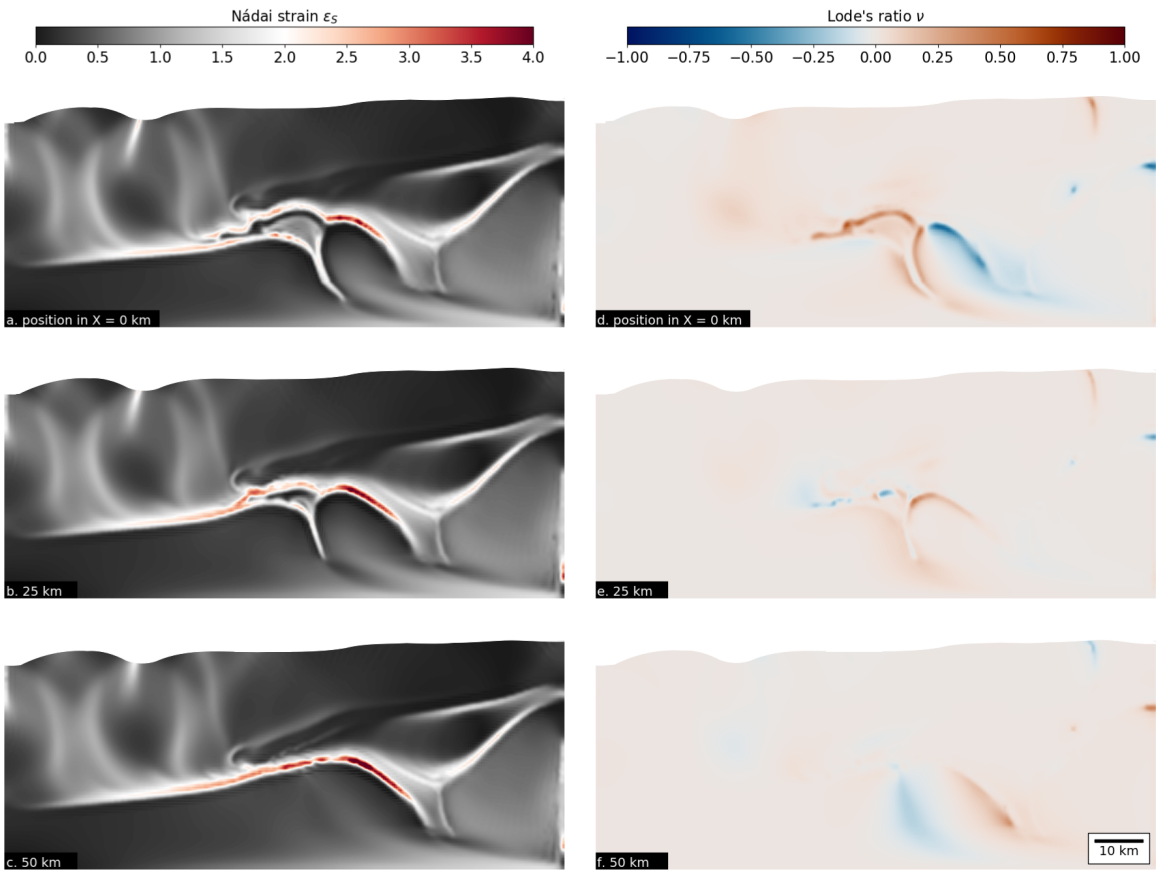

Figure 3.12: Graph showing three different cross-sections of model A.G-1 displaying Nádai strain (first column) and Lode's ratio (second column). Row-wise cross-sections at X = 0, 25, 50 km, respectively.

softening mechanism. In our models, the main cause of the strain localization is the initial geometrical configuration and the variations of mechanical strength between the model units. Strain localization and associated shear zone formation due to geometrical and strength variations has been shown with 2D numerical simulations to occur even for linear viscous material (Bauville and Schmalholz, 2017). For such strain localization no variation of effective material properties develops and it is, hence, sometimes termed kinematic strain localization, which is fundamentally different to so-called dynamic softening mechanisms in which the effective material properties change, for example due to local heating, grain size reduction or fluid infiltration (Bauville and Schmalholz, 2017). Moreover, the formation of fold nappes by pushing ductile material against a rigid obstacle, without dynamic softening, was shown, for example, with laboratory deformation experiments (e.g. Bucher, 1956) and numerical simulations (e.g. Peña and Catalán, 2004). Dynamic softening mechanism are most likely active in nature, but their intensity and the required deformation conditions are still contentious. Furthermore, dynamic softening mechanisms most likely intensify the strain localization shown in our models,

but our models show that, in principle, such dynamic softening mechanism are not essential to generate nappe-like structures.

The emplacement of the sediments from HB in the style of a thrust nappe is observed in all models with exception of model C.G.-1. The thrust nappe exhibits a laterally uniform front despite the deformation and nappe formation in HG below (Figure 3.4). Even in the case of model A.G-2, where the basement horst is strongly incorporated in the deformation, we do not observe large horizontal displacement gradients in the thrust nappe. Hence, deformation of such relatively small graben systems might play only a minor role on the displacement variations along strike of fold-and-thrust belts. In our models, the uniform thrust front is the result of the initially straight boundary between basement horst and HB. Consequently, we infer that the initial large scale basin architecture plays a major role in the geometry of orogenic salients. Several studies (e.g. Thomas, 1977; Marshak et al., 1992; Boyer and Elliott, 1982) of different orogens also indicate that the sediment basin thickness is of particular importance in the expression of salients. In this context, Macedo and Marshak (1999) investigated the effect of variable basin geometries during bulk shortening using 3D sandbox models. Their study implies that basin-controlled salients are strongly controlled by the basin topography, that is, variations of sedimentary thickness inside the basin. There are, however, additional conditions such as the indenter shape or the direction and orientation of convergence of the colliding plates that influence the overall shape of orogens (e.g. Laubscher, 1972; Ries, 1976; Mitra, 1997). Naturally, the investigation of such large scale boundary effects would require a different model configuration than in our study.

Volume variations related to the lateral changes in the depth of HG are always expressed in the lateral variations of the thickness of the extruded nappe. The thinning out of the initial graben structure is reflected in a decrease of height and a decrease of length of the nappe. These lateral variations also affect the lateral amplitude variation of the major detachment fold of simulation C.G-1. The local geometry around the major detachment fold resembles a thin skinned tectonic style where most deformation is concentrated in the cover sediment. However, much of the sediments filling the core of the detachment fold originate from HG, which is more than 10 km away from the detachment fold (Figure 3.11g-l). Closure of HG resulted in movement of sediments from HG into the core of the detachment fold. This result shows that detachment fold initiation and progressive evolution can be controlled by the inherited basement structure, Additionally, this finding suggest that predominately thin skinned tectonics can passively be influenced by underlying heterogeneities due to variations in the basement architecture. Nevertheless, the expression of such detachment folds in our models also depends largely on the thickness ratio between incompetent and competent units. Our findings are, therefore, in broad agreement with previous field observations and numerical studies (e.g. Pfiffner, 1993; Jaquet et al., 2014).

3.5.2 Comparison with the Helvetic nappe system

Model A.G-1 and B.G-1 are able to reproduce several first-order structural features of the Helvetic nappe system. In addition, we are also able to connect the two different main kinematic deformation phases of the Western Helvetics and the Eastern Helvetic Nappes. The formation of the main basal thrust originates in weak sedimentary units, comparable to the Cretaceous Palfris shales, of our Helvetic basin equivalent. Similarly to the PrabÃľ deformation phase in the West and the contemporaneous Calanda phase in the East (e.g. Pfiffner, 2015), this basal thrust aids in the transport of a laterally uniform thrust nappe in our simulations. Given the simplifications of our model we attribute the resulting major thrust front to the formation of basal thrust of the Wildhorn super-nappe in the West and the Glarus thrust in the East. Continuous bulk shortening leads to shear localization at the contact between the strong layer and the horst in the basin. Subsequently, the layer is detached and translated with help of the weak sediments across the basement horst and onto the half-graben, resembling a thrust sheet or nappe. We record a first noticeable deformation of the half-graben approximately 2 Ma in our simulations. This timing is in agreement with a study by Jaquet et al. (2018) which proposes a similar time interval between the onset of the Helvetic nappes and the onset of the basal thrusting at the Morcles half-graben. Continuing, the vertical extrusion and squeezing-out of the half-graben sediments takes place simultaneous with stacking of the major thrust nappe on top at about 6 to 7 Ma. The resulting nappe stack shows major structural differences in the lateral direction of the model. This along-strike variation is comparable to the lateral structural variations in the Helvetic nappe system. At the end of our simulations we record approximately 10 Ma for the complete process of nappe stack formation. This timing is in broad agreement with studies of the Morcles nappe complex (e.g. Kirschner et al., 1996; Boutoux et al., 2016) that suggest an emplacement duration of 10 to 15 Ma.

Figure 3.13 shows a comparison between geological cross-sections taken along-strike of the Helvetic nappe systems with selected zoomed in numerical cross-sections in lateral direction of our model. The first cross-section a) of model A.G-1 (Figure 3.13d,e,f) shows our equivalent of the Morcles nappe at the maximum depth of the half-graben. The result here is similar to 2D numerical studies by Bauville and Schmalholz (2015) who investigated fold nappe formation and nappe stack formation also in application to the Helvetic nappe system, respectively. To first order we reproduce an extruded fold nappe with a shape comparable to the Morlces nappe, which means that its the length only slightly exceeds its height. The strong layer is still connected to the adjacent basement horst and the deformed internal weak units, highlighted by the green passive marker lines, resembles a recumbent fold. The inner part of the fold nappe roots into a steep cusp, analogues to the Chamonix zone between the Aiguilles-Rouges and Mont Blanc massif (Figure 3.13a). Moreover, we find significant amount of material from the overburden between the thrust nappe and the fold nappe, but also below the fold nappe. The material between the two nappes resembles the Ultrahelvetics in the geological cross-sections,

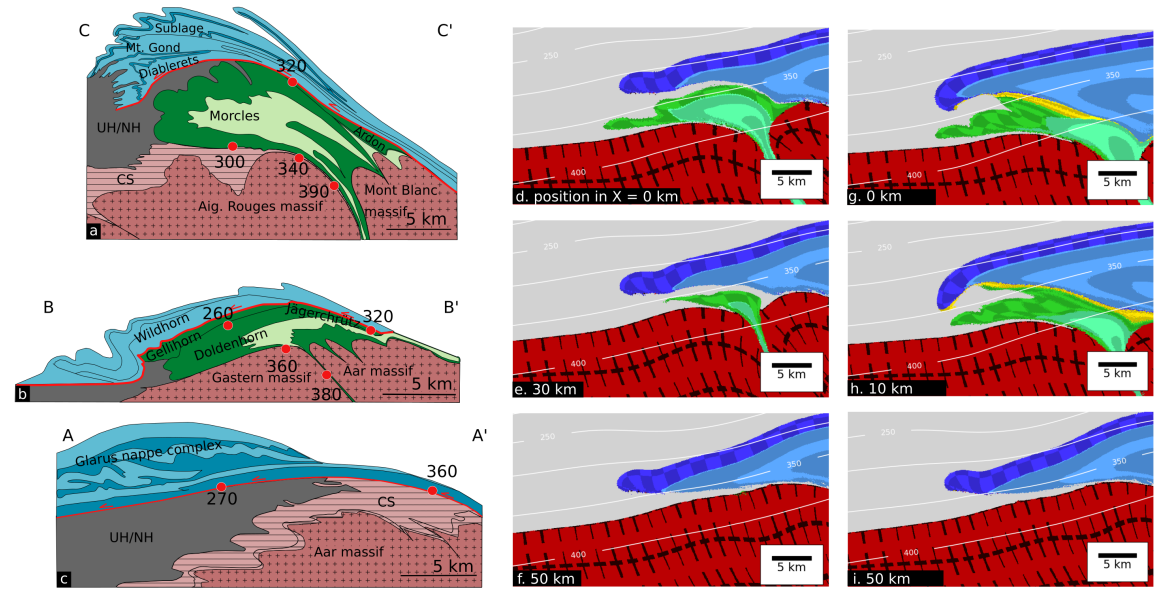

Figure 3.13: Comparison between the geological cross-sections of the Morcles nappe, Doldenhorn nappe and Glarus nappe complex with sections taken from our numerical simulations. Columnwise(left to right) 1.column: geological-cross sections, 2.column: sections from model A.G-1, and 3.column: sections from model D.G-1. Temperatures taken from Ebert et al. (2008). UH/NH = Ultrahelvetics/North Helvetics. CS = Cover sediments.

whereas the material below the fold nappe corresponds to undeformed cover-sequences of the basement. Turning now to the Morcles equivalent of model B.G-1 (Figure 3.13g) we find a significant different structure of the extruded fold nappe. There are several major differences that are connected to the initial mechanical layering inside the half-graben. First, the fold nappe shows a far greater length to height aspect ratio than the natural analogue. Secondly, the strong normal limb is not in contact with the basement horst. Due to the continuous strong layer the structure shows greater shearing at the contact between the fold and thrust nappe.

Proceeding with cross-section e) of our numerical model A.G-1 (Figure 3.13e), we find similarities with the geological cross-section of the Doldenhorn nappe (Figure 3.13b). The extruded nappe shows similar aspect ratio and shape like the Doldenhorn nappe with the length significantly exceeding the thickness. However, cross-section h) of model B.G-1 (Figure 3.13h) provides an even better match with the structure of the Doldenhorn nappe. The resulting fold nappe shows a comparable shape and size. Due to the initial rheological layering this model forms a thin thrust sheet on top of the fold nappe. We interpret this thrust sheet as an analogue to the Gellihorn and Jägerchrütz nappes, which are essentially thin thrust sheets on top of the Doldenhorn nappe (Pfiffner et al., 2011).

Finally the numerical cross-sections without half-graben (Figure 3.13f,i) exhibit a similar displacement and shape for both of our models. The finding suggests that underlying nappe

formation in HG and minor variations in the vertical rheological layering has a negligible effect on the horizontal displacement parallel to the shortening direction along strike of the major thrust sheet. To first order, this structure is comparable to the Glarus nappe complex displayed in Figure 3.13c.

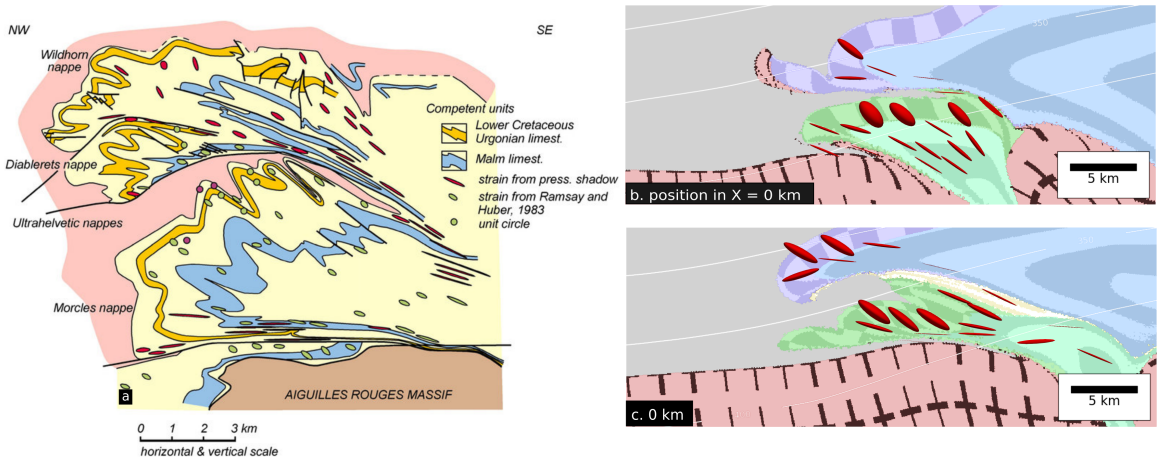

Figure 3.14: Comparison between finite strain from the Morcles nappe (taken fromBastida et al. (2014); after Casey and Dietrich (1997) modified from Dietrich and Casey (1989), green strain ellipses from Ramsay and Huber (1987)) and selected finite strain ellipses from model A.G-1 and model D.G-1.

Additionally, we also find a first order agreement when comparing the finite strain pattern between field measurements from the Morcles nappe and our numerically calculated finite strain (Figure 3.14). Generally, the aspect ratio of the strain ellipses increases towards the bottom and root zone of the nappe, indicating significant shearing. Furthermore, we observe less deformed ellipses in the top, normal limb of our Morcles equivalent with ellipses of higher aspect ratios (Figure 3.14b, d) near the contact between the fold nappe and the thrust nappe. Figure 3.14b shows a better match for the finite strain pattern in the upper limb, whereas Figure 3.14c displays a better fit for the contact zone. We also observe a subhorizontal orientation of the major finite strain axis towards the root zone of the nappe (Figure 3.14c). Numerical finite strain computation is a useful tool to compare numerical models with natural observations. The comparison can efficiently be used to recognize where the numerical model requires adaptation to the real data.

However, certain first order features of the Helvetic nappe system we could not reproduce with our models. The first shortcoming is the protrusion and shearing out of the strong layer of the half-graben. In 3D view this process is expressed as a thin carpet in front of the fold nappe (e.g. Figure 3.4c,f), resembling a nose-like feature in the 2D cross-sections. Shearing out of the layer inhibits the formation of an outer recumbent limb as observed in the Morcles nappe (Ramsay et al., 1983). Here, our results are in contrast with previous 2D thermo-mechanical numerical modelling results by Bauville and Schmalholz (2015), who successfully simulated the

formation of a recumbent fold limb during half-graben inversion. One of the main reasons for this deviation lies in the viscosity ratio (η_R) between overlying strong layer (η_L) and the half-graben infill (η_I). In the simulations of Bauville and Schmalholz (2015), both the layer and the infill have the same viscosity ($\eta_R = 1$), whereas our simulations, using different creep flow laws for each units, show that the infill viscosity η_I can be up to three orders of magnitude smaller than the strong layer viscosity η_L ($\eta_R = 1000$). Secondly, temperature estimates from several authors (e.g. Kirschner et al., 1999; Herwegh and Pfiffner, 2005; Ebert et al., 2007b) indicate lower peak temperature conditions along the different basal nappe contacts in comparison with our simulations. For example, Ebert et al. (2008) reports increasing temperatures of $270°C$ to $390°C$ from the front of the Morcles nappe to its root. Here we find a close match with root zone temperatures, whereas our front part of the fold nappe exhibits temperatures in the range of $370°C$ (e.g. Figure 3.13d). Similar temperature comparisons between our Doldenhorn and Glarus thrust complex equivalents show the same trend (see Figure 3.13). Moreover, the cross-sections of model B.G-1 exhibit slightly higher temperatures inside the core of the fold nappe, in consequence of the significantly thicker thrust nappe above. In summary our models show a good match for the root zone temperatures, but higher temperatures at the front of the nappe complexes compared to natural observations. Ebert et al., 2008 suggests a horizontal temperature gradient of approximately $6°C/km$ along the nappe interface for all three cross-sections. We only register a horizontal gradient of $2°C/km$ along the basal thrust surfaces. Additional constraints are given by Leloup et al. (2005) and Boutoux et al. (2016) who indicate peak metamorphic temperatures of $320°C$ for the Aiguilles-Rouges massif and $400°C$ for the Mont Blanc massif. Despite these discrepancies our model conforms to the temperature trends of natural observations, showing increasing temperatures from the front to the root zones of the nappes. Further improvements could be made by adjusting the initial geothermal gradient or by modifying the initial geometrical configuration. For the latter case, primarily, Nibourel et al. (2018) demonstrate that the Aar massif experienced a $10-15°$ southwards dip in relation to the isotherms. Essentially such a configuration would, for example, place the half-graben system further up in the isotherms. This adjustment would lead to cooler temperatures in the front of the nappe and greater horizontal temperature gradients during and after nappe emplacement. In terms of large scale structural components our simulations lack the formation of parasitic folds, smaller imbricate thrusts or the detachment between different levels inside the major thrust complex. Modelling of such smaller-scale features would require (i) a higher numerical resolution in combination with (ii) a drastically more complex rheologically layering. In addition, field observations indicate the existence of several large scale shear zones in the Mont Blanc and Aar massif. Our models do not reproduce such features, mainly because of our mechanically homogeneous basement unit which represents a large simplification compared to the natural complexities. There are, for example, several studies regarding the Aar massif that correlate the formation of ductile and brittle shear zones to inherited pre-alpine heterogeneities

(e.g. Berger et al., 2017; Mair et al., 2018). In particular, structures such as foliations, mafic dykes or folds present mechanical anisotropies that can culminate in localized strain and shear zones (e.g. Bell, 1978; Carreras et al., 2010; Herwegh et al., 2017; Wehrens et al., 2017). Finally, our model does not fully resolve the large scale kinematics and intricate deformational history of the Helvetic nappe system. For example, reconstructions between the SW and the NE of the Helvetics show a differential horizontal displacement of the thrust nappes of up to 50 km (e.g. Pfiffner, 2015). Here, variations are likely due to the initial basement geometry and convergence of subducting plate e.g. obliquity of the plate which have not been taken into account in our model.

3.5.3 Comparing geological with modelled cross sections: The Morcles nappe

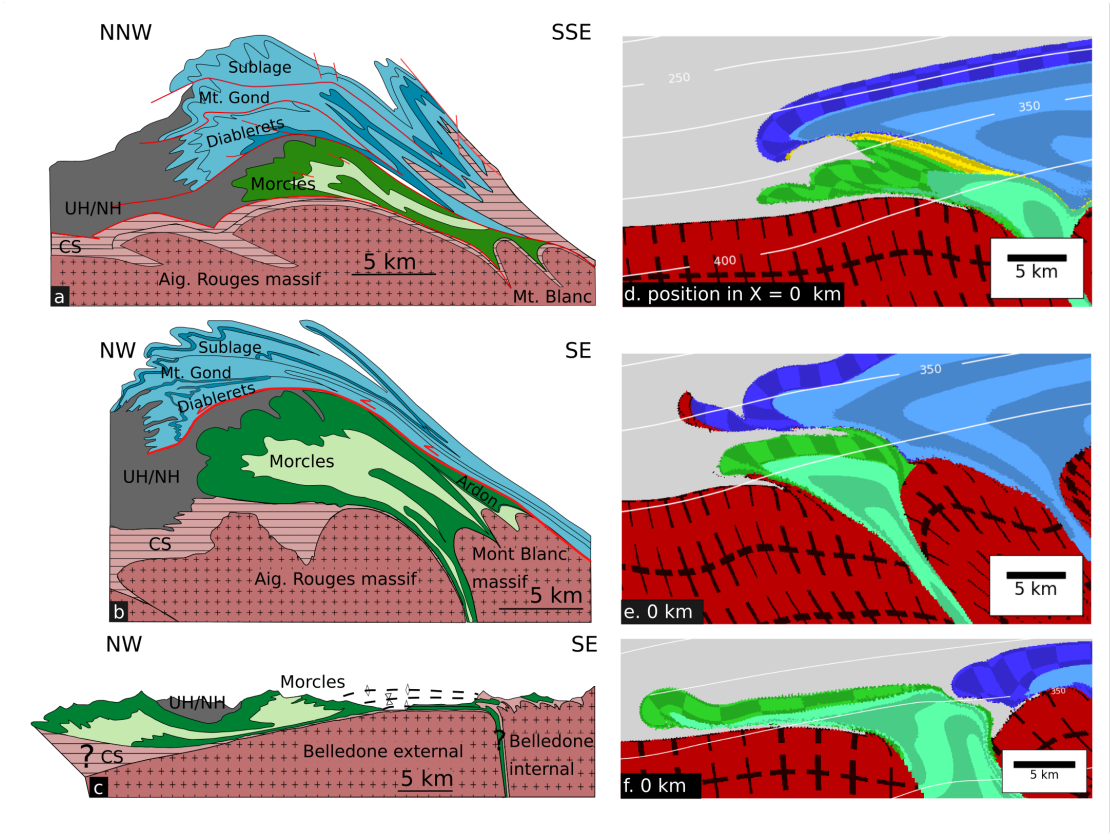

Figure 3.15: Comparison between selected numerical cross-sections and simplified geological cross-sections. Row-wise(top to bottom) a) Simplified Morcles section modified after Pfiffner (2015) (indicated in the map of Figure 3.1 with the dashed profile line) and d) section from model D.G-1. b) Simplified Morcles modified section after Escher et al. (1993) and e) cross-section model F.G-1. c) Simplified section modified after Epard (1990) and f) section from model A.G-2. UH/NH = Ultrahelvetics/North Helvetics. CS = Cover sediments.

The method of cross-sectional balancing and reconstruction is one of the major tools to understand the evolution of fold-and-thrust belts on different structural scales (e.g. Dahlstrom, 1969; Price, 1981; Baby et al., 1992; Massoli et al., 2006; Alavi, 2007). Even though some authors suggest an underlying bias of such techniques due to different simplifications (Butler et al., 2019), geological cross-sections themselves are indispensable. In addition, they are useful for comparisons with numerical models that aim to decipher the mechanical processes and material properties that lead to the formation of geological structures. However, caution is advised when comparing sections of numerical models with geological cross section. The large three-dimensional variability in geological structures and structures generated in numerical models such as in this study should be a warning sign when trying to fit one observation with one model. Hence, in this section we show and compare three different geological cross sections of the Morcles nappe with our numerical results (Figure 3.15). The cross sections are from different locations along strike of the Morcles nappe and highlight, together with our numerical cross section, the complexity of geological reconstruction. We start with a comparison of a geological cross section of the Morcles nappe near the Sanetschpass and a section of model B.G-1 (Figure 3.15a and d). Here, the geological cross section shows a relatively thin Morcles nappe with a sheared lower and upper limb. This observation is similar to our cross section which exhibits an elongated sheared fold nappe with sheared lower and upper limbs. Moreover, in this model we observe a significant deformation of the basement at the contact of the cover sediments which is in agreement with microstructural observations that suggest a brittle-ductile emplacement of the Morcles nappe (Ebert et al., 2007a; Austin et al., 2008). Figure 3.15b shows a Morcles cross section of Escher et al. (1993) from further Southwest in the nappe system. In this case, model D.G-1 (Figure 3.15e) provides a better first order fit than B.G-1. Our fold nappe exhibits a strongly sheared recumbent limb that still reaches into the root zone of the nappe. Furthermore, the strong layer is still connected to the basement horst and is in contact with the thrust nappe where it is sheared, displaying a similar saw-tooth shape as observed in the geological cross section. Also, the overall aspect ratio is closer to the geological cross-section than in model B.G-1. In contrast, both of the previous numerical sections do not match the observations for the Morcles nappe even further Southwest in France near Megève (Figure 3.15c). Here, the sediments are rather squeezed out of the half-graben due to a greater thickness of shales instead of forming a recumbent limb (Epard, 1990). Therefore, we suggest that a cross-section of model A.G-2 Figure (3.15f) shows a closer match to the geological structure. In summary, different cross sections of the Morcles nappe can be compared to different numerical models with different initial conditions regarding the geometry or rheology. Hence, it is a challenge to capture the evolution of 3D geological structures with a single 3D model, because of the geometrical and rheological uncertainties. Further, this also implies that one has to be even more cautious in the application of a single 2D model to the formation of 3D fold-and-thrust belts and geological structures in general.

3.6 Conclusions

The presented 3D numerical simulations show the formation of a fold-and-thrust belt resulting from the wedge-type deformation of the upper crustal region of a passive margin. The deformed crustal region is characterized by a half-graben with laterally varying thickness and a horst separating the half-graben from a laterally homogeneous basin. The numerical simulations show the formation of tectonic nappes with horizontal displacement of several tens of kilometers and with geometries ranging from fold nappe to thrust nappe. The formation of the sedimentary nappes results from the shearing-off and detachment of sedimentary units form the half-graben, horst and basin. Nappe detachment, transport and stacking occur for standard viscoplastic rheological models without any applied rheological, or dynamic, softening mechanisms. Nappe formation and their geometry are controlled by the initial basement geometry and the strength contrast between basement and cover sediments and the strength contrast within the sediments. The results indicate the fundamental importance of tectonically inherited structures on the evolution of fold-and-thrust belts. Consequently, the results emphasize the importance of geological field work and reconstructions of the initial geological situation before fold-and-thrust belt formation.

Modelled nappe-like structures generated from sediments from the half-graben with laterally varying depth show that the nappe geometry strongly depends on the amount of sediments available for nappe formation. The calculation of 3D finite strain shows that the deformation during the formation of nappes originating from the half-graben largely deviates from a 2D plane strain deformation. Nappes originating from the laterally homogeneous basin show a more or less laterally straight displacement front indicating that the laterally heterogeneous deformation during nappe formation in the half-graben region does not considerably affect the overthrusting nappe.

The applied strength of the basement has a strong control on the resulting nappe geometry. A relatively stronger basement favors the formation of nappes resembling a thrust nappe while reduced basement strength (due to a stress cut-off at 40 MPa) favors the formation of fold nappes.

The initial model configuration was based on geological reconstructions of the Helvetic nappe system. The modelled 3D structures show several first-order similarities with this nappe system: (1) Formation of a nappe resulting from the closure of a half-graben. Depending on the model configuration, this nappe can be more similar to a fold or a thrust nappe. The modelled nappes are applicable to the Morcles and Doldenhorn nappes of the Helvetic nappe system. (2) Formation of a laterally homogeneous thrust nappe which overthrusts and is stacked above the underlying nappe resulting from half-graben closure. This nappe is applicable to the Wildhorn and Glarus nappe. (3) The detachment of minor sediment units originally located on the horst and their emplacement between the upper thrust nappe and the underlying nappe from the half-graben. These minor nappes are applicable to the

Ardon, Jägerchrütz and Gellihorn nappes. (4) The entrapment of weak sediments, which were originally situated structurally above the sediments eventually forming nappes, between the two major nappes. These entrapped sediments are applicable to the Ultrahelvetic units. (5) The modelled temperatures, temperature gradients and finite strain gradients are in overall agreement with data from the Helvetic nappe system.

Acknowledgements

This work was supported by SNF grant No. 200020-149380 and the University of Lausanne. Moreover, this work was supported by a grant from the Swiss National Supercomputing Centre (CSCS) under project ID s785. In addition we thank Ludovic Räss and Philippe Logean for supporting us in the utilization of the Octopus Super Computing Cluster at the University of Lausanne.

Bibliography

Alavi, M., 2007. Structures of the Zagros fold-thrust belt in Iran. American Journal of science 307 (9), 1064–1095.

Austin, N., Evans, B., Herwegh, M., Ebert, A., 2008. Strain localization in the Morcles nappe (Helvetic Alps, switzerland). swiss Journal of Geosciences 101 (2), 341–360.

Baby, P., Hérail, G., Salinas, R., Sempere, T., 1992. Geometry and kinematic evolution of passive roof duplexes deduced from cross section balancing: Example from the foreland thrust system of the southern Bolivian Subandean Zone. Tectonics 11 (3), 523–536.

Badertscher, N. P., Abart, R., Burkhard, M., McCaig, A., 2002. Fluid flow pathways along the Glarus overthrust derived from stable and Sr-isotope patterns. American Journal of Science 302 (6), 517–547.

Badertscher, N. P., Burkhard, M., 2000. Brittle–ductile deformation in the Glarus thrust Lochseiten (LK) calc-mylonite. Terra Nova 12 (6), 281–288.

Bastida, F., Aller, J., Fernandez, F. J., Lisle, R. J., Bobillo Ares, N. C., Menendez, O., 2014. Recumbent folds: key structural elements in orogenic belts. Earth-science reviews 135, 162–183.

Bauville, A., Schmalholz, S. M., 2013. Thermo-mechanical model for the finite strain gradient in kilometer-scale shear zones. Geology 41 (5), 567–570.

Bauville, A., Schmalholz, S. M., 2015. Transition from thin-to thick-skinned tectonics and consequences for nappe formation: Numerical simulations and applications to the Helvetic nappe system, Switzerland. Tectonophysics 665, 101–117.

Bauville, A., Schmalholz, S. M., 2017. Tectonic inheritance and kinematic strain localization as trigger for the formation of the Helvetic nappes, Switzerland. Swiss Journal of Geosciences 110 (2), 523–534.

Bell, T., 1978. Progressive deformation and reorientation of fold axes in a ductile mylonite zone: the Woodroffe thrust. Tectonophysics 44 (1-4), 285–320.

Bellahsen, N., Jolivet, L., Lacombe, O., Bellanger, M., Boutoux, A., Garcia, S., Mouthereau, F., Le Pourhiet, L., Gumiaux, C., 2012. Mechanisms of margin inversion in the external Western Alps: Implications for crustal rheology. Tectonophysics 560, 62–83.

Bercovici, D., Ricard, Y., 2003. Energetics of a two-phase model of lithospheric damage, shear localization and plate-boundary formation. Geophysical Journal International 152 (3), 581–596.

Berger, A., Wehrens, P., Lanari, P., Zwingmann, H., Herwegh, M., 2017. Microstructures, mineral chemistry and geochronology of white micas along a retrograde evolution: An example from the Aar massif (Central Alps, Switzerland). Tectonophysics 721, 179–195.

Beutner, E. C., 1977. Causes and consequences of curvature in the Sevier orogenic belt, Utah to Montana.

Boutoux, A., Bellahsen, N., Nanni, U., Pik, R., Verlaguet, A., Rolland, Y., Lacombe, O., 2016. Thermal and structural evolution of the external Western Alps: Insights from (U–Th–Sm)/He thermochronology and RSCM thermometry in the Aiguilles Rouges/Mont Blanc massifs. Tectonophysics 683, 109–123.

Boyer, S. E., Elliott, D., 1982. Thrust systems. Aapg Bulletin 66 (9), 1196–1230.

Buchanan, J. G., Buchanan, P. G., 1995. Basin inversion. Vol. 88. Geological Society London.

Bucher, W. H., 1956. Role of gravity in orogenesis. Geological Society of America Bulletin 67 (10), 1295–1318.

Burkhard, M., 1988. L'Helvétique de la bordure occidentale du massif de l'Aar (évolution tectonique et métamorphique). Eclogae Geologicae Helvetiae 81 (1), 63–114.

Burkhard, M., Kerrich, R., Maas, R., Fyfe, W., 1992. Stable and Sr-isotope evidence for fluid advection during thrusting of the Glarus nappe (Swiss Alps). Contributions to Mineralogy and Petrology 112 (2-3), 293–311.

Butler, R., 1989. The influence of pre-existing basin structure on thrust system evolution in the Western Alps. Geological Society, London, Special Publications 44 (1), 105–122.

Butler, R. W., Bond, C. E., Cooper, M. A., Watkins, H., 2019. Fold–thrust structures–where have all the buckles gone? Geological Society, London, Special Publications 487, SP487–7.

Carreras, J., Czeck, D. M., Druguet, E., Hudleston, P. J., 2010. Structure and development of an anastomosing network of ductile shear zones. Journal of Structural Geology 32 (5), 656–666.

Casey, M., Dietrich, D., 1997. Overthrust shear in mountain building. In: Evolution of Geological Structures in Micro-to Macro-scales. Springer, pp. 119–142.

Dahlen, F. A., nov 1984. Noncohesive critical Coulomb wedges: An exact solution. Journal of Geophysical Research: Solid Earth 89 (B12), 10125–10133.

Dahlen, F. A., Suppe, J., 1988. Mechanics, growth, and erosion of mountain belts. Processes in continental lithospheric deformation: Geological Society of America Special Paper 218, 161–178.

Dahlstrom, C., 1969. Balanced cross sections. Canadian Journal of Earth Sciences 6 (4), 743–757.

Davis, D., Suppe, J., Dahlen, F. A., feb 1983. Mechanics of fold-and-thrust belts and accretionary wedges. Journal of Geophysical Research 88 (B2), 1153.

Dietrich, D., Casey, M., 1989. A new tectonic model for the Helvetic nappes. Geological Society, London, Special Publications 45 (1), 47–63.

Dunn, J. F., Hartshorn, K. G., Hartshorn, P. W., 1995. Structural styles and hydrocarbon potential of the sub-Andean thrust belt of southern Bolivia.

Ebert, A., Herwegh, M., Berger, A., Pfiffner, A., 2008. Grain coarsening maps for polymineralic carbonate mylonites: a calibration based on data from different Helvetic nappes (Switzerland). Tectonophysics 457 (3-4), 128–142.

Ebert, A., Herwegh, M., Evans, B., Pfiffner, A., Austin, N., Vennemann, T., 2007a. Microfabrics in carbonate mylonites along a large-scale shear zone (Helvetic Alps). Tectonophysics 444 (1-4), 1–26.

Ebert, A., Herwegh, M., Pfiffner, A., 2007b. Cooling induced strain localization in carbonate mylonites within a large-scale shear zone (Glarus thrust, Switzerland). Journal of Structural Geology 29 (7), 1164–1184.

Epard, J. L., 1990. La nappe de Morcles au sud-ouest du Mont-Blanc. Ph.D. thesis.

Epard, J.-L., Escher, A., 1996. Transition from basement to cover: a geometric model. Journal of Structural Geology 18 (5), 533–548.

Epard, J.-L., Groshong Jr, R. H., 1993. Excess area and depth to detachment. AAPG bulletin 77 (8), 1291–1302.

Escher, A., Masson, H., Steck, A., 1993. Nappe geometry in the western Swiss Alps. Journal of structural Geology 15 (3-5), 501–509.

Fernandez, N., Kaus, B. J., 2014. Fold interaction and wavelength selection in 3D models of multilayer detachment folding. Tectonophysics 632, 199–217.

Fitz Diaz, E., Hudleston, P., Tolson, G., 2011. Comparison of tectonic styles in the Mexican and Canadian Rocky Mountain fold-thrust belt. Geological Society, London, Special Publications 349 (1), 149–167.

Gillcrist, R., Coward, M., Mugnier, J.-L., 1987. Structural inversion and its controls: examples from the Alpine foreland and the French Alps. Geodinamica acta 1 (1), 5–34.

Granado, P., Ruh, J. B., 2019. Numerical modelling of inversion tectonics in fold-and-thrust belts. Tectonophysics 763, 14–29.

Hamilton, W. B., 1988. Laramide crustal shortening. Interaction of the Rocky Mountain foreland and the Cordilleran thrust belt: Geological Society of America Memoir 171, 27–39.

Hansen, F., Carter, N., et al., 1983. Semibrittle creep of dry and wet Westerly granite at 1000 MPa. In: The 24th US Symposium on Rock Mechanics (USRMS). American Rock Mechanics Association.

Herwegh, M., Berger, A., Baumberger, R., Wehrens, P., Kissling, E., 2017. Large-scale crustal-block-extrusion during late Alpine collision. Scientific reports 7 (1), 413.

Herwegh, M., Hürzeler, J.-P., Pfiffner, O. A., Schmid, S. M., Abart, R., Ebert, A., 2008. the Glarus thrust: excursion guide and report of a field trip of the swiss tectonic studies Group (swiss Geological society, 14.–16. 09. 2006). swiss Journal of Geosciences 101 (2), 323–340.

Herwegh, M., Pfiffner, O.-A., 2005. Tectono-metamorphic evolution of a nappe stack: A case study of the Swiss Alps. Tectonophysics 404 (1-2), 55–76.

Hürzeler, J.-P., Abart, R., 2008. Fluid flow and rock alteration along the Glarus thrust. swiss Journal of Geosciences 101 (2), 251–268.

Jaquet, Y., Bauville, A., Schmalholz, S. M., 2014. Viscous overthrusting versus folding: 2-D quantitative modeling and its application to the Helvetic and Jura fold and thrust belts. Journal of Structural Geology 62, 25–37.

Jaquet, Y., Duretz, T., Grujic, D., Masson, H., Schmalholz, S. M., 2018. Formation of orogenic wedges and crustal shear zones by thermal softening, associated topographic evolution and application to natural orogens. Tectonophysics 746, 512–529.

Jaquet, Y., Duretz, T., Schmalholz, S. M., 2015. Dramatic effect of elasticity on thermal softening and strain localization during lithospheric shortening. Geophysical Journal International 204 (2), 780–784.

Kaus, B., Popov, A. A., Baumann, T., Pusok, A., Bauville, A., Fernandez, N., Collignon, M., 2016. Forward and inverse modelling of lithospheric deformation on geological timescales. In: Proceedings of NIC Symposium.

King Hubbert, M., Rubey, W. W., 1959. Role of fluid pressure in mechanics of overthrust faulting: I. Mechanics of fluid-filled porous solids and its application to overthrust faulting. Geological Society of America Bulletin 70 (2), 115–166.

Kirschner, D., Masson, H., Sharp, Z., 1999. Fluid migration through thrust faults in the Helvetic nappes (Western Swiss Alps). Contributions to Mineralogy and Petrology 136 (1-2), 169–183.

Kirschner, D. L., Cosca, M. A., Masson, H., Hunziker, J. C., 1996. Staircase 40/Ar39Ar spectra of fine-grained white mica: Timing and duration of deformation and empirical constraints on argon diffusion. Geology 24 (8), 747–750.

Kirschner, D. L., Sharp, Z. D., Masson, H., 1995. Oxygen isotope thermometry of quartz-calcite veins: Unraveling the thermal-tectonic history of the subgreenschist facies Morcles nappe (Swiss Alps). Geological society of America bulletin 107 (10), 1145–1156.

Kiss, D., Podladchikov, Y., Duretz, T., Schmalholz, S. M., 2019. Spontaneous generation of ductile shear zones by thermal softening: Localization criterion, 1D to 3D modelling and application to the lithosphere. Earth and Planetary Science Letters 519, 284–296.

Kronenberg, A. K., Kirby, S. H., Pinkston, J., 1990. Basal slip and mechanical anisotropy of biotite. Journal of Geophysical Research: Solid Earth 95 (B12), 19257–19278.

Lacombe, O., Bellahsen, N., 2016. Thick-skinned tectonics and basement-involved fold–thrust belts: insights from selected Cenozoic orogens. Geological Magazine 153 (5-6), 763–810.

Lacombe, O., Mouthereau, F., 2002. Basement-involved shortening and deep detachment tectonics in forelands of orogens: Insights from recent collision belts (Taiwan, Western Alps, Pyrenees). Tectonics 21 (4), 12–1.

Laubscher, H., 1972. Some overall aspects of Jura dynamics. American Journal of Science 272 (4), 293–304.

Leloup, P.-H., Arnaud, N., Sobel, E. R., Lacassin, R., 2005. Alpine thermal and structural evolution of the highest external crystalline massif: The Mont Blanc. Tectonics 24 (4).

Lode, W., 1926. Versuche über den Einfluß der mittleren Hauptspannung auf das Fließen der Metalle Eisen, Kupfer und Nickel. Zeitschrift für Physik 36 (11-12), 913–939.

Lymer, G., Cresswell, D. J., Reston, T. J., Bull, J. M., Sawyer, D. S., Morgan, J. K., Stevenson, C., Causer, A., Minshull, T. A., Shillington, D. J., 2019. 3D development of detachment faulting during continental breakup. Earth and Planetary Science Letters 515, 90–99.

Macedo, J., Marshak, S., 1999. Controls on the geometry of fold-thrust belt salients. Geological Society of America Bulletin 111 (12), 1808–1822.

Mair, D., Lechmann, A., Herwegh, M., Nibourel, L., Schlunegger, F., 2018. Linking Alpine deformation in the Aar Massif basement and its cover units–the case of the Jungfrau–Eiger mountains (Central Alps, Switzerland). Solid Earth 9, 1099–1122.

Marshak, S., Wilkerson, M., Hsui, A., 1992. Generation of curved fold-thrust belts: Insight from simple physical and analytical models. In: Thrust tectonics. Springer, pp. 83–92.

Mase, G. E., 1970. Continuum mechanics. Vol. 970. McGraw-Hill New York.

Massoli, D., Koyi, H. A., Barchi, M. R., 2006. Structural evolution of a fold and thrust belt generated by multiple décollements: analogue models and natural examples from the Northern Apennines (Italy). Journal of Structural Geology 28 (2), 185–199.

Masson, H., Baud, A., Escher, A., Gabus, J., Marthaler, M., 1980. Paléokarsts crétacés et tertiaires dans la nappe de Morcles. Compte rendu de lâĂŹexcursion de la Société géologique Suisse du 1, 331–349.

Merle, O., 1989. Strain models within spreading nappes. Tectonophysics 165 (1-4), 57–71.

Milnes, A. G., Pfiffner, O.-A., 1980. Tectonic evolution of the Central Alps in the cross section St. Gallen-Como. Eclogae Geologicae Helvetiae 73 (2), 619–633.

Mitra, G., 1997. Evolution of salients in a fold-and-thrust belt: the effects of sedimentary basin geometry, strain distribution and critical taper. In: Evolution of geological structures in micro-to macro-scales. Springer, pp. 59–90.

Mitra, S., Fisher, G. W., 1992. Structural geology of fold and thrust belts. Johns Hopkins University Press.

Mouthereau, F., Deffontaines, B., Lacombe, O., Angelier, J., Byrne, T., Liu, C., 2002. Variations along the strike of the Taiwan thrust belt: Basement control on structural style, wedge geometry, and kinematics. Sspecial Papers-Geological Society of Aamerica, 31–54.

Nádai, A., Hodge, P., 1963. Theory of Flow and Fracture of Solids, vol. II. Journal of Applied Mechanics 30, 640.

Nemčok, M., Mora, A., Cosgrove, J., 2013. Thick-skin-dominated orogens; from initial inversion to full accretion: an introduction. Geological Society, London, Special Publications 377 (1), 1–17.

Nibourel, L., Berger, A., Egli, D., Luensdorf, N. K., Herwegh, M., 2018. Large vertical displacements of a crystalline massif recorded by Raman thermometry. Geology 46 (10), 879–882.

Peña, J. M. V., Catalán, J. R. M., 2004. A computer program for the simulation of folds of different sizes under the influence of gravity. Computers & geosciences 30 (1), 33–43.

Pfiffner, O. A., 1993. The structure of the Helvetic nappes and its relation to the mechanical stratigraphy. Journal of structural Geology 15 (3-5), 511–521.

Pfiffner, O. A., 2006. Thick-skinned and thin-skinned styles of continental contraction. Sspecial Papers-Geological Society of Aamerica 414, 153.

Pfiffner, O. A., 2015. Geologie der Alpen. Vol. 8416. UTB.

Pfiffner, O.-A., Burkhard, M., Hänni, R., Kammer, A., Kligfield, R., Mancktelow, N., Menkveld, J., Ramsay, J., Schmid, S., Zurbriggen, R., 2011. Structural map of the Helvetic zone of the Swiss Alps, including Vorarlberg (Austria) and Haute Savoie (France).

Poulet, T., Veveakis, M., Herwegh, M., Buckingham, T., Regenauer Lieb, K., 2014. Modeling episodic fluid-release events in the ductile carbonates of the Glarus thrust. Geophysical Research Letters 41 (20), 7121–7128.

Price, N. J., McClay, K. R., 1981. Thrust and nappe tectonics. Geological Society of London.

Price, R., 1981. The Cordilleran foreland thrust and fold belt in the southern Canadian Rocky Mountains. Geological Society, London, Special Publications 9 (1), 427–448.

Ramsay, J., 1981. Tectonics of the Helvetic nappes. Geological Society, London, Special Publications 9 (1), 293–309.

Ramsay, J., 1989. Fold and fault geometry in the western Helvetic nappes of Switzerland and France and its implication for the evolution of the arc of the western Alps. Geological Society, London, Special Publications 45 (1), 33–45.

Ramsay, J. G., Casey, M., Kligfield, R., 1983. Role of shear in development of the Helvetic fold-thrust belt of Switzerland. Geology 11 (8), 439–442.

Ramsay, J. G., Huber, M. I., 1987. The techniques of modern structural geology: Folds and fractures. Vol. 2. Academic press.

Ries, A., 1976. A Discussion on natural strain and geological structure-Patterns of strain variation in arcuate fold bets. Philosophical Transactions of the Royal Society of London. Series A, Mathematical and Physical Sciences 283 (1312), 281–288.

Rodgers, J., 1949. Evolution of thought on structure of middle and southern Appalachians. AAPG Bulletin 33 (10), 1643–1654.

Ruh, J. B., Gerya, T., Burg, J.-P., 2014. 3D effects of strain vs. velocity weakening on deformation patterns in accretionary wedges. Tectonophysics 615, 122–141.

Ruh, J. B., Kaus, B. J., Burg, J.-P., 2012. Numerical investigation of deformation mechanics in fold-and-thrust belts: Influence of rheology of single and multiple décollements. Tectonics 31 (3).

Schmalholz, S., Podladchikov, Y., Burg, J.-P., 2002. Control of folding by gravity and matrix thickness: Implications for large-scale folding. Journal of Geophysical Research: Solid Earth 107 (B1), ETG–1.

Schmid, S., Boland, J., Paterson, M., 1977. Superplastic flow in finegrained limestone. Tectonophysics 43 (3-4), 257–291.

Schmid, S. M., 1975. The Glarus overthrust: Field evidence and mechanical model. Ecologae Geol. Helvetia 68, 247–280.

Simpson, G., 2011. Mechanics of non-critical fold-thrust belts based on finite element models. Tectonophysics 499 (1-4), 142–155.

Steck, A., 1999. Carte tectonique des Alpes de Suisse occidentale et des régions avoisinantes. Office fédéral des eaux et de la géologie.

Stockmal, G. S., oct 1983. Modeling of large-scale accretionary wedge deformation. Journal of Geophysical Research 88 (B10), 8271.

Termier, P., 1906. La synthèse géologique des Alpes.

Thomas, W. A., 1977. Evolution of Appalachian-Ouachita salients and recesses from reentrants and promontories in the continental margin. American Journal of Science 277 (10), 1233–1278.

Trümpy, R., Aubert, D., Bernoulli, D., 1980. Geology of Switzerland: Geological excursions. Vol. 10. Wepf.

Von Tscharner, M., Schmalholz, S., Epard, J.-L., 2016. 3-D numerical models of viscous flow applied to fold nappes and the Rawil depression in the Helvetic nappe system (western Switzerland). Journal of Structural Geology 86, 32–46.

Wehrens, P., Baumberger, R., Berger, A., Herwegh, M., 2017. How is strain localized in a meta-granitoid, mid-crustal basement section? Spatial distribution of deformation in the central Aar massif (Switzerland). Journal of structural geology 94, 47–67.

Wissing, S., Pfiffner, O.-A., 2003. Numerical models for the control of inherited basin geometries on structures and emplacement of the Klippen nappe (Swiss Prealps). Journal of structural geology 25 (8), 1213–1227.

Yamato, P., Kaus, B. J., Mouthereau, F., Castelltort, S., 2011. Dynamic constraints on the crustal-scale rheology of the Zagros fold belt, Iran. Geology 39 (9), 815–818.

CHAPTER 4

Conclusions

4.1 Summary

Chapter 2

We presented the 3D numerical models of viscous folding and over-thrusting of a strong layer that is embedded inside a weak matrix is initiated along a lateral pre-existing weak zone under pure shear shortening. All simulations indicate that folding transitions to over-thrusting, or vice-versa, depending on the detachment horizon thickness below the strong layer. Hence, our models support and extend the previous results of 2D numerical models by Jaquet et al. (2014). Furthermore, our results support the hypothesis by Pfiffner (1993) who used the ratio between incompetent and competent layers in the mechanical stratigraphy to infer the mode of deformation along-strike of the Helvetic nappe system of the Western Swiss Alps. Thus, we are able to relate our simple viscous model to geological field observations, which likely occurred under more complex brittle-ductile conditions (Pfiffner, 1993). Our results show that the transition between viscous folding and over-thrusting culminates in a smooth cusp in the transition between folding and thrusting. In case of a orthogonal weak zone in regards to the compressional direction we do not observe significant strike slip movement between the two domains of the models. Strike-slip in the range of $2-6\%$ occurs only in simulations with an oblique weak zone, suggesting that the orientation to the velocity boundary is of major importance. The implementation of 3D finite strain computation and tracing allows us to quantify several aspects of the transition between the two deformation modes. Here, we employ the Nádai strain ϵ_S and the Lode's ratio ν. Both values are used to characterize the the strain pattern along the limbs of the fold and the thrust inside a Hsu diagram. The Hsu diagram shows overall smaller strains in the folding domain that increase towards the thrusting domain. In particular ν values show that the transition zone is marked by a strain ellipsoid that is in the flattening regime. Cross-sections along the fold limbs also display an increase of strain magnitude in the direction of the thrusting domain. Henceforth, the lateral ϵ_S gradient reflects gradients in the detachment horizon thickness of the model configuration. Higher detachment horizon thickness gradients culminate a higher ϵ_S gradient. Additionally, strong gradients in the detachment horizon generate higher peak strain values at the end of the flat-ramp geometry towards the thrusting domain. Similarly ν shows a drop from positive ,flattening, values to approximately values of zero when transitioning from folding to thrusting. Hence both values could theoretically be used to locate mechanical discontinuities in the stratigraphy or basement structure by finite strain analysis of cover-sequences. Furthermore we show that statistical analysis with the aid of rosediagrams is a useful tool to determine the bulk values for the 3D orientation of finite strain in complex structures such as folds. The dip angle of the principal axis gradually changes from the folding end to the thrusting. These results could also potentially be used to help in the interpretation of field measurements.

Chapter 3

Lateral and vertical variations in the three-dimensional geometry of inherited structures of passive margins, such as basins and half-grabens, present a significant mechanical heterogeneity that exerts a strong control on the structural evolution during compressional tectonics. Basement highs or graben horsts have a significant impact on plastic strain localization. Our models show that thrust nappe formation is initiated at the contact between the relatively strong sedimentary layer and basement unit. The underlying weak units aid in the detachment and sub-horizontal transport of a coherent thrust sheet across the basement and on top of the half-graben. This half-graben undergoes ductile closer with progressive bulk shortening. Moreover, the closure of the half-graben results in the extrusion of the half-graben infill which exhibits a structure similar to a fold nappe. The dimensions of this fold nappe change in lateral direction of the model depending on the half-graben structure (depth). Hence, we are able simulate 3D nappe stacking of a thrust nappe on top of a fold nappe. The structure of the fold nappe changes laterally, but has no significant effect on the horizontal propagation of the thrust sheet/nappe. Therefore, it is likely that differences in horizontal displacement orthogonal to the transport direction of thrust nappes is largely controlled by the initial geometry, for example, the basin structure, or basin orientation in regards to the velocity boundary. Several of our simulations show a first order agreement with natural observations from the Helvetic nappe system. We are able to reproduce different fold nappes in lateral direction of the model similar to the structures observed along-strike of the Helvetic nappe system. Depending on the depth and length of the half-graben we either observe a structure resembling the Morcles nappe or the Doldenhorn nappe. In the domain without half-graben we observe the emplacement of a thrust nappe analogues to the Glarus nappe complex of the Eastern Swiss Alps. In general, our nappe stack is formed during approximately 10 Ma of convergence which is in good agreement with natural data. Furthermore, our thermal structure is also close to conditions during the emplacement of the Helvetic nappes. There are some key features that we do not capture with our standard rheology, such as the strongly overturned limb of the Morcles nappe. Here our configuration employing a pressure-insensitive von Mises yield strength that mimicks a semi-brittle deformation, or a low temperature plasticity aids in the development of a overturned limb that is closer to the natural observations of the Morcles nappe. Altogether our results point therefore to a brittle-ductile deformation mechanism which is agreement with macro and micro structural observations.

4.2 Conclusion and Outlook

Inherited structures exert a strong control on the structural evolution of geological systems. In Chapter 2 we presented the impact of lateral variations in the mechanical stratigraphy on the interaction between folding and thrusting. One further step in this direction would be the use

self consistent shear zone formation instead of a pre-existing weak zone. In order to achieve self-consistency future work should ideally apply a visco-elasto-plastic rheology together with a temperature dependent rheology. A model like this might generate increased torque or strike slip between the two modes of deformation resulting in plastic failure. Here, it would also be of interest how the shear zone is formed. For example, in our models the shear zone was initially symmetric, however, in case of a more complex model the shear zone might not be initiated everywhere at the same time or place. Furthermore, this kind of model could also be used to investigate the formation of fractures across the fold. Additionally, similar configurations could be applied to the modelling of basement thrusts via underlying basement ramps. Such ramps are often proposed but seldom modeled (e.g. Burkhard, 1988; Allerton, 1994; Zerlauth et al., 2014). Continuing, the presented model in Chapter 3 brings some additional insight into three dimensional nappe formation. In perspective of the Helvetic nappe systems next steps could be taken to gain additional knowledge on the differential displacement (e.g. up to 50 km Schmid, 1975) between the southwest and the northeast of the system. This would require a significant altered structure of the basin from which the thrusts originate, or altogether a different model boundary condition. This new boundary condition could, for example, comprise a fixed oblique indenter, similar to sandbox models. Additionally, high resolution 2D numerical models should be used to investigate the effect of a brittle-ductile deformation regime on the fold nappe formation. In this context our results show that a combination of brittle deformation in the basement and ductile flow of the sediments produces the closest match to the observed nappe structures. High resolution 2D numerical models would also allow for additional rheological layering and the implementation of mechanical anisotropies inside the basement. Hence, one other step could also be the implementation of mechanical anisotropies in the basement, such as folds, foliations or pre-existing faults, which also played a crucial role during the uplift of the basement massifs (e.g. Herwegh et al., 2017).

Bibliography

Allerton, S., 1994. Vertical-axis rotation associated with folding and thrusting: An example from the eastern Subbetic zone of southern Spain. Geology 22 (11), 1039–1042.

Burkhard, M., 1988. L'Helvétique de la bordure occidentale du massif de l'Aar (évolution tectonique et métamorphique). Eclogae Geologicae Helvetiae 81 (1), 63–114.

Herwegh, M., Berger, A., Baumberger, R., Wehrens, P., Kissling, E., 2017. Large-scale crustal-block-extrusion during late Alpine collision. Scientific reports 7 (1), 413.

Jaquet, Y., Bauville, A., Schmalholz, S. M., 2014. Viscous overthrusting versus folding: 2-D quantitative modeling and its application to the Helvetic and Jura fold and thrust belts. Journal of Structural Geology 62, 25–37.

Pfiffner, O. A., 1993. The structure of the Helvetic nappes and its relation to the mechanical stratigraphy. Journal of structural Geology 15 (3-5), 511–521.

Schmid, S. M., 1975. The Glarus overthrust: Field evidence and mechanical model. Ecologae Geol. Helvetia 68, 247–280.

Zerlauth, M., Ortner, H., Pomella, H., Pfiffner, O. A., Fügenschuh, B., 2014. Inherited tectonic structures controlling the deformation style: an example from the Helvetic nappes of the Eastern Alps. Swiss Journal of Geosciences 107 (2-3), 157–175.

CHAPTER 5

Appendix

Supplementary A: 2D and 3D finite strain Matlab code

Following section contains two supplementary Matlab codes for 2D finite strain (Listing 5.1) and 3D finite strain calculation (Listing 5.2) under pure and simple shear deformation. The codes were created to demonstrate and exemplify the finite strain computation in Chapter 2. Additionally we also provide two figures displaying the result of a 2D (Figure 5.1) and 3D calculation (Figure 5.2).

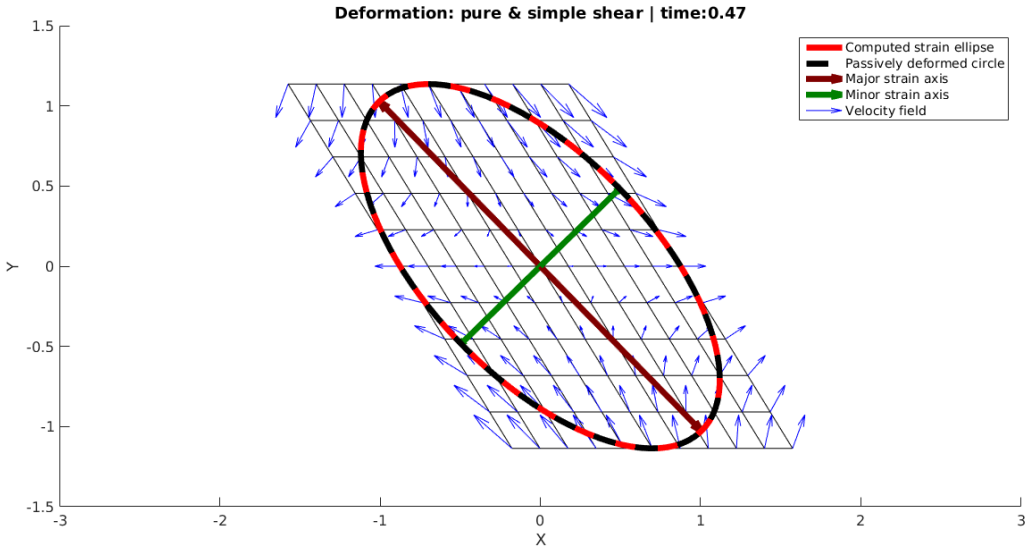

Figure 5.1: Final state of the deformation of a unit circle under a combination of pure and simple shear resulting in the pictured 2D finite strain ellipse . The result was obtained with the 2D finite strain matlab code below.

Listing 5.1: Matlab code for 2D finite strain calculation

```
% Plot 2D finite strain ellipse: plane strain, simple shear
% for a homogeneous deformation
clear all, close all
%% Input
% ================================
ps_rate          =    -2;                % Pure shear strain rate
ss_rate          =    0;                 % Simple shear strain rate
nt               =    1000;           % Number of time steps
dt               =    0.01;              % Time increment
%% Pre-Processing
% ================================
% initialize grid
X                =        [-1:0.2:1];      % Specify coordinate range X
Y                =        X;               % Specify coordinate range Y
[X2D, Y2D]       =        meshgrid(X, Y); % Create 2D coordinate system
X2D_ini          =    X2D;             % Store X2D matrix
Y2D_ini          =    Y2D;             % Store Y2D matrix
% Initialize marker circle
theta            =    linspace(0,2*pi,100);   % Initalize theta angle
Xc               =    cos(theta);             % Initalize X coordinates
Yc               =    sin(theta);             % Initalize Y coordinates
XYc_ini          =    [Xc; Yc];               % Relate X to Y
XYc              =    XYc_ini;                % Store XY coordinates
F                =    [1 0; 0 1];             % Initial deformation gradient tensor
time             =    0;                      % Initial time
```

```
26
27
28  %% Time loop
29  % ================================
30  for tstep       =   1:1
31      time        =   time+dt;
32
33     if     tstep > 10 && tstep < 40, ss_rate = -2; ps_rate  =   0; % Change deformation
34     elseif tstep > 40,               ss_rate =  1; ps_rate  =   1; end
35      %% Calculate Velocity Field and Update Coordinates
36      % Get Deformation matrices
37      PSmat           =   repmat(ps_rate, size(XYc));   % matrix to apply pure shear
38      PSmat(2,:)      =   -PSmat(2,:);
39      SSmat           =   repmat(ss_rate, size(XYc));   % matrix to apply simple shear
40      SSmat(2,:)      =   0;
41      % Deform grid
42      VX_ps           =   X2D.*ps_rate;           % Velocity due to pure shear deformation for X
43      VY_ps           =  -Y2D.*ps_rate;               % Velocity due to pure shear deformation for Y
                            "
44      VX_ss           =   Y2D.*ss_rate;               % Velocity due to simple shear deformation for X
45      VY_ss           =   zeros(size(VX_ss));         % Velocity due to simple shear deformation for Y
46      VX_tot          =   VX_ss+VX_ps;                % Total velocity for X
47      VY_tot          =   VY_ss+VY_ps;                % Total velocity for Y
48      X2D             =   X2D + VX_tot*dt;            % Add deformation to grid for X
49      Y2D             =   Y2D + VY_tot*dt;            % Add deformation to grid for Y
50
51      % Deform the marker circle
52      VXYc_ps         =   XYc.*PSmat;             % Velocity matrix for pure shear deformation
53      VXYc_ss         =   flipud(XYc).*SSmat;     % Velocity matrix for simple shear deformation
54      VXYc_tot        =   VXYc_ps + VXYc_ss;      % Total velocity matrix
55      XYc             =   XYc + VXYc_tot.*dt;     % Add deformation to XY
56
57      %% Calculate the Principial Strain Axes
58      % ================================
59      % Calculate finite strain ellipse
60      D               =   [1+dt*ps_rate dt*ss_rate;dt*0 1-dt*ps_rate];    % incremental transformation
            tensor
61      F               =   D*F;                                            % update finite transformation
            tensor
62      XY_strain_el =   F * XYc_ini;
63      B               = F*F';                 % Left Cauchy-Green tensor
64      [BV,BE]         = eigs(B);              % Spectral decomposition
65      VE              = diag(sqrt(diag(BE))); % Square roots of eigenvalues
66      FS              = BV*VE;                % Scale eigenvectors with eigenvalues
67      psax            = FS(:,2);                 % Finite strain axis 1
68      psay            = FS(:,1);                 % Finite strain axis 2
69      %% Post-processing
70      % ================================
71      clf; hold on
72      h = plot(X2D, Y2D,'-k',X2D', Y2D','-k'); % Plot grid
73      set(gca,'Color',[1 1 1])
74      set(gca,'Fontsize',12)
75
76      vel = quiver(X2D,Y2D,VX_tot,VY_tot,'b');                                    % Plot velocity
            vector field
77
78      a1 =    quiver(0,0, psax(1), psax(2),'color',[0.5 0   0],'linewidth',5,'AutoScale','off');
79      a2 =    quiver(0,0, psay(1), psay(2),'color',[0   0.5 0],'linewidth',5,'AutoScale','off');
80              quiver(0,0,-psax(1),-psax(2),'color',[0.5 0   0],'linewidth',5,'AutoScale','off');
81              quiver(0,0,-psay(1),-psay(2),'color',[0   0.5 0],'linewidth',5,'AutoScale','off');
82
83      comp_el = plot(XY_strain_el(1,:),XY_strain_el(2,:),'r-','linewidth',5);    % Plot calculated
            strain ellipse                          % plot imposed ellipse
84      pass_el = plot(XYc(1,:), XYc(2,:),'--k','linewidth',5);                    % Plot passive marker
             strain ellipse
85      if ps_rate == 0 && ss_rate == 0
86          a = 'no deformation';
87      elseif ps_rate ~= 0 && ss_rate == 0
88          a = 'pure shear';
89      elseif ps_rate == 0 && ss_rate ~= 0
90          a = 'simple shear';
91      elseif ps_rate ~= 0 && ss_rate ~= 0
92          a = 'pure & simple shear';
93      end
```

```
94      title(['Deformation: ',a,' | time:',num2str(time)])
95      axis equal
96      axis([-3 3 -1.5 1.5]);
97      axis on
98      ylabel('Y'),xlabel('X')
99      if sum(abs(psax)) < sum(abs(psay)) % find major and minor axis to update legend
100         s  = a2; a2 = a1; a1 = s;
101     end
102     legend([comp_el, pass_el, a1, a2, vel],'Computed strain ellipse','Passively deformed circle','
            Major strain axis','Minor strain axis','Velocity field','location','northeast')
103
104     drawnow
105     pause(0.1)
106     end
```

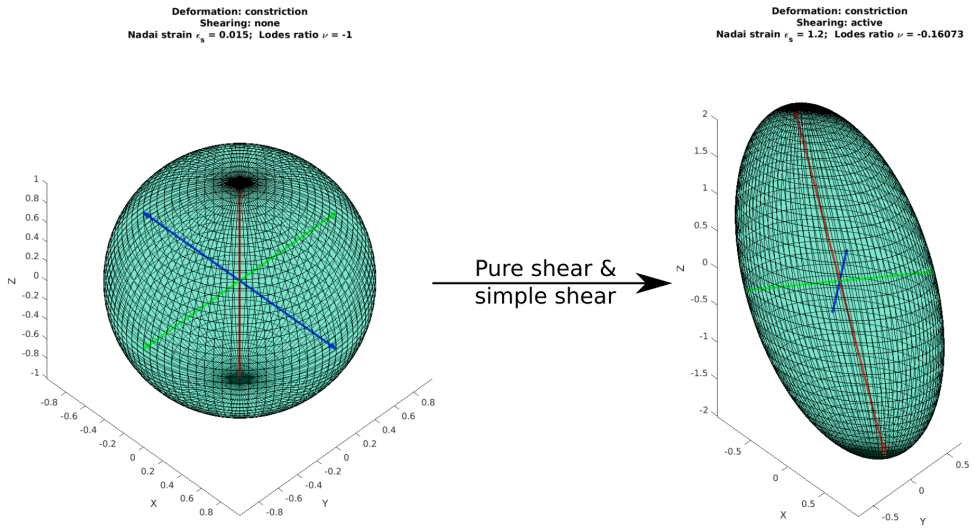

Figure 5.2: Deformation of a unit sphere (left, after first time step) to a ellipsoid (right) under combination of pure and simple shear. The ellipsoid inside shows the three principal strain axis. Both deformation states were produced with the matlab code below. The figure heading displays the current values of ε_s and ν.

Listing 5.2: Matlab code for 3D finite strain calculation

```
1  % Plot 3D finite strain ellipsoid: plane strain, simple shear xy, xz, yz
2  % for a homogeneous deformation
3  clear all, close all
4  %% Input
5  % ===================================
6  % Primary deformation mode, set one variable to 1 rest to 0
7  plane_strain     = 0;
8  constriction     = 1;
9  flattening       = 0;
10 % Specify pure shear
11 ps_rate          = 1;
12 % Add shear deformation
13 xy_rate          = 0;
14 xz_rate          = 0;
15 yz_rate          = 0;
16 % Time
17 dt       = 0.01; % time step
18 nt       =   70; % number of time steps
19 tsxy     =   20;
20 tsxz     =   40;
21
22 %% Pre-Processing
```

```
% ================================
% Initiate sphere coordinates
r            = pi*(-24:0.5:24)/24;
s            = pi*(0:0.5:24)/24;
[theta,phi] = meshgrid(r,s);
X            = sin(phi).*cos(theta);
Y            = sin(phi).*sin(theta);
Z            = cos(phi);
% Save initial coordinates
XYZ_ini      = [X(:)';Y(:)';Z(:)'];

% Initiate deformation gradient tensor
Fxx = 1; Fxy = 0; Fxz = 0;
Fyx = 0; Fyy = 1; Fyz = 0;
Fzx = 0; Fzy = 0; Fzz = 1;

F    = [Fxx Fxy Fxz;...
        Fyx Fyy Fyz;...
        Fzx Fzy Fzz];
% Initiate additional parameters
nadai_strain = 0;
lodes_ratio  = 0;
time         = 0;


%% Time loop
% ================================
for it  = 1:nt
            %% add shear deformation after certain time limit
            if it > tsxy, xy_rate         =  3.0;                        end
            if it > tsxz, xz_rate         = -1.0; xy_rate         = 0; end
            %% Check deformation mode
            if sum(abs([xy_rate, xz_rate, yz_rate])) ~= 0, shear = 'active';
            else shear = 'none';end
            if plane_strain == 1
            ps_rateX = ps_rate;
            ps_rateY = ps_rate;
            ps_rateZ = 0;
            def = 'plane strain';
            elseif constriction == 1
            ps_rateX = -0.5*ps_rate;
            ps_rateY =  0.5*ps_rate;
            ps_rateZ = ps_rate;
            def = 'constriction';
            elseif flattening == 1
            ps_rateX = 0.5*ps_rate;
            ps_rateY = ps_rate;
            ps_rateZ = 0.5*ps_rate;
            def = 'flattening';
            else disp('plase define deformation mode'), break;
            end
            %% Calculate Velocity Field and Update Coordinates of Ellipsoid
            VXr_ps       =   X.*ps_rateX;                % Velocity due to pure shear deformation
            VYr_ps       =  -Y.*ps_rateY;                % Velocity due to pure shear deformation
            VZr_ps       =   Z.*ps_rateZ;            % Velocity due to pure shear deformation

            VXr_xy       =   Y.*xy_rate;             % Velocity due to simple shear deformation
            VXr_xz       =   Z.*xz_rate;             % Velocity due to simple shear deformation

            VYr_xy       =   zeros(size(VXr_xy));        % Velocity due to simple shear deformation
            VYr_yz       =   Z.*yz_rate;             % Velocity due to simple shear deformation

            VZr_xz       =   zeros(size(VXr_xy));    % Velocity due to simple shear deformation
            VZr_yz       =   zeros(size(VXr_xy));    % Velocity due to simple shear deformation

            VXr_tot      =   VXr_ps + VXr_xy + VXr_xz;  % Total velocity in X
            VYr_tot      =   VYr_xy + VYr_ps + VYr_yz;  % Total velocity in Y
            VZr_tot      =   VZr_xz + VZr_yz + VZr_ps;  % Total velocity in Z

            X            =   X + VXr_tot*dt;             % Add deformation to ellipsoid
            Y            =   Y + VYr_tot*dt;             % Add deformation to ellipsoid
            Z            =   Z + VZr_tot*dt;             % Add deformation to ellipsoid

            %% calculate deformation gradient tensor
```

```
97              D                =   [1+dt*ps_rateX   dt*xy_rate      dt*xz_rate;...
98                                     0            1-dt*ps_rateY     dt*yz_rate;...
99                                     0              0             1+dt*ps_rateZ    ]; % Incremental
                                        transformation tensor
100             F                =   D*F;                                              % Update deformation
                tensor
101
102             % Apply deformation gradient to initial sphere
103             XYZ_strain_el     = F * XYZ_ini;
104             XFS               = reshape(XYZ_strain_el(1,:),size(X,1),size(X,2));
105             YFS               = reshape(XYZ_strain_el(2,:),size(X,1),size(X,2));
106             ZFS               = reshape(XYZ_strain_el(3,:),size(X,1),size(X,2));
107             % Safety check for discrepancy between deformation by velocity field
108             % and deformation gradient tensor calculation
109             errVF = [max(max(max(abs((X(:)-XFS(:))))), max(abs((Y(:)-YFS(:))))), max(abs((Z(:)-ZFS(:)
                    ))))];
110
111             % Calculate principal axis length and direction via polar
112             % decomposition
113             B            = F*F';                  % Left Cauchy-Green tensor
114             [BV,BE]      = eigs(B);               % Spectral decomposition
115             VE           = diag(sqrt(diag(BE))); % Square roots of eigenvalues
116             FS           = BV*VE;                 % Scale eigenvectors with eigenvalues
117             % Compute lode's ratio, nadai strain
118             e                 = sort(diag(VE),'descend'); % principal strains
119             nadai_strain      = (1/sqrt(3)) * sqrt( (log(e(1)) - log(e(2)))^2 ...
120                                 +                   (log(e(1)) - log(e(3)))^2 +...
121                                                     (log(e(3)) - log(e(1)))^2 );
122
123             lodes_ratio       = (2*log(e(2)) - log(e(1)) - log(e(3)))...
124                                  /(log(e(1)) - log(e(3)));
125
126             %% Post-processing
127              clf, hold on
128              view([45 45])
129              % Plot ellipsoid
130              h  = surf(X,Y,Z);
131              set(h,'FaceColor',[0 0.8 0.6],'FaceAlpha',0.3)
132              set(gca,'Fontsize',12)
133              set(gca,'visible','on');
134
135               % Principal strain axes vector
136              [~,idx]       = sort(max(abs(FS))); FSsorted = FS(:,idx); % sort matrix to keep colors
                    fixed
137              psa_major     = FSsorted(:,3);
138              psa_imed      = FSsorted(:,2);
139              psa_minor     = FSsorted(:,1);
140              % Plot prinipal strain axes
141              quiver3(0,0,0,-psa_major(1),-psa_major(2),-psa_major(3),'color', [1 0 0],'linewidth',3,
                    'AutoScale','off')
142              quiver3(0,0,0,-psa_minor(1),-psa_minor(2),-psa_minor(3),'color', [0 0 1],'linewidth',3,
                    'AutoScale','off')
143              quiver3(0,0,0,-psa_imed(1) ,-psa_imed(2) ,-psa_imed(3) ,'color', [0 1 0],'linewidth',3,
                    'AutoScale','off')
144              quiver3(0,0,0, psa_major(1), psa_major(2), psa_major(3),'color', [1 0 0],'linewidth',3,
                    'AutoScale','off')
145              quiver3(0,0,0, psa_minor(1), psa_minor(2), psa_minor(3),'color', [0 0 1],'linewidth',3,
                    'AutoScale','off')
146              quiver3(0,0,0, psa_imed(1) , psa_imed(2) , psa_imed(3) ,'color', [0 1 0],'linewidth',3,
                    'AutoScale','off')
147
148              %Velocity Field
149 %            quiver3(X(1:10:end),Y(1:10:end),Z(1:10:end),VXr_tot(1:10:end),VYr_tot(1:10:end),VZr_tot
        (1:10:end),'color', [ 0 0 0],'linewidth',1,'AutoScale','on')
150
151              axis equal
152              ylabel('Y'), xlabel('X'), zlabel('Z');
153              title({['Deformation: ',def]; ['Shearing: ',shear]; ['Nadai strain \epsilon_{s} = ',
                    num2str(nadai_strain,2),';  Lodes ratio \nu = ',num2str(lodes_ratio)]})
154              drawnow
155              pause(0.01)
156
157 end
```

Supplementary B: Benchmark

This section comprises the results of some parallel computing benchmarks with the LaMEM code. The benchmarks were conducted in context of an successful application for computing hours at the CSCS Swiss National Supercomputing Center in the framework of this project. First we display the results for a strong scaling test for a 3D wedge configuration (temperature-dependent visco-plastic rheology) similar to the one shown in Chapter 3 (Figure 5.3; Table 5.1). Here we use a fixed numerical resolution of 512x256x128 grid points. Additionally we include a figure deciphering the relation between required resources (node hours) and real time days to solve the model used for the strong scaling(Table 5.4). Afterwards we present a weak scaling benchmark for a configuration of viscous falling spheres in a viscous matrix (Figure 5.5; Table 5.2). The spheres have a 1000 times higher viscosity than the matrix.
Strong scaling benchmarks are used to test and evaluate the behavior of an application by fixing the total size of the problem and increasing the number of processors. In this case the number of processors is given by the amount of cores/nodes that we use. In order to evaluate the efficiency of the code we calculate the speed-up S_p:

$$S_p = \frac{t_1}{t_p} \tag{5.1}$$

Where t_1 is the time needed to solve the problem for the least amount of required cores/nodes (processors) and t_p is time for an increased amount of cores/nodes for the same problem size. Ideally the speed-up would double with double the amount of cores/nodes. However such a scenario is unrealistic and the performance degrades at one point due to, for example, communication overhead.
Weak scaling investigates the behavior of an application by fixing the size of the problem per processor and increasing the number of processors, in our case cores/nodes. Weak scaling provides a measurement of parallel efficiency E_p given by:

$$E_p = \frac{S_p}{p} \tag{5.2}$$

Where S_p is th speed-up and p the number of processors (cores/nodes). In an ideal case E_p should be 1. However, in general for most applications E_p decreases with increasing number of processors. In the scientifc computing a $E_p > 0.5$ is acceptable, which we reach for most of our tests.

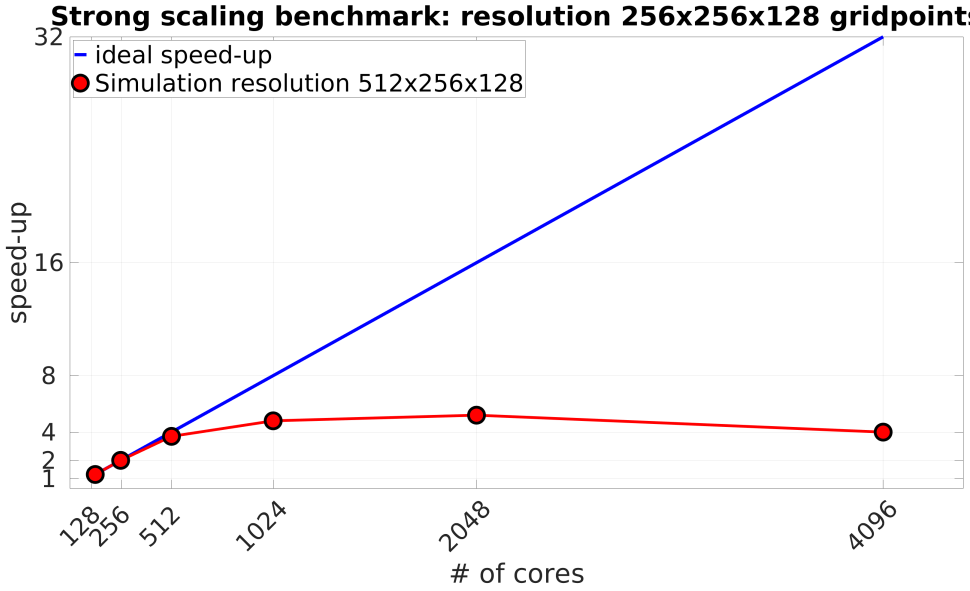

Figure 5.3: Strong scaling for a 3D wedge configuration employing a resolution of 512x256x128 grid points using 12 CPU cores per node.

Table 5.1: Number of cores and nodes, wall time and speed-up for a 3D wedge configuration employing a resolution of 512x256x128 gridpoints using 12 CPU cores per node.

Cores	Nodes	Wall time [s]	Speed-up
128	11	720	1.0
256	22	368	2.0
512	43	196	3.7
1024	86	150	4.8
2048	171	139	5.2
4096	342	182	4.0

Table 5.2: Cores, nodes, resolution in gridpoints, multigrid levels, coarse grid size per core, KSP iteration count, solution time for one timestep, parallel efficiency of the weak scaling benchmark using a viscous falling sphere configuration using 12 CPU cores per node.

Cores	Nodes	Resolution	MG levels	Coarse level per core	KSP Iterations	Solution time [s]	Parallel efficiency
64	6	128x128x128	5	4x4x4	71	46.9582	1.00
128	11	256x128x128	6	1x1x1	77	57.1306	0.89
256	22	256x256x128	6	2x2x2	64	48.1605	0.87
512	43	256x256x256	6	2x2x2	76	56.6713	0.88
1024	86	512x256x256	6	1x1x1	74	65.0811	0.75
2048	171	512x512x256	6	1x1x1	78	77.3255	0.66
4096	342	512x512x512	6	1x1x1	75	121.865	0.41

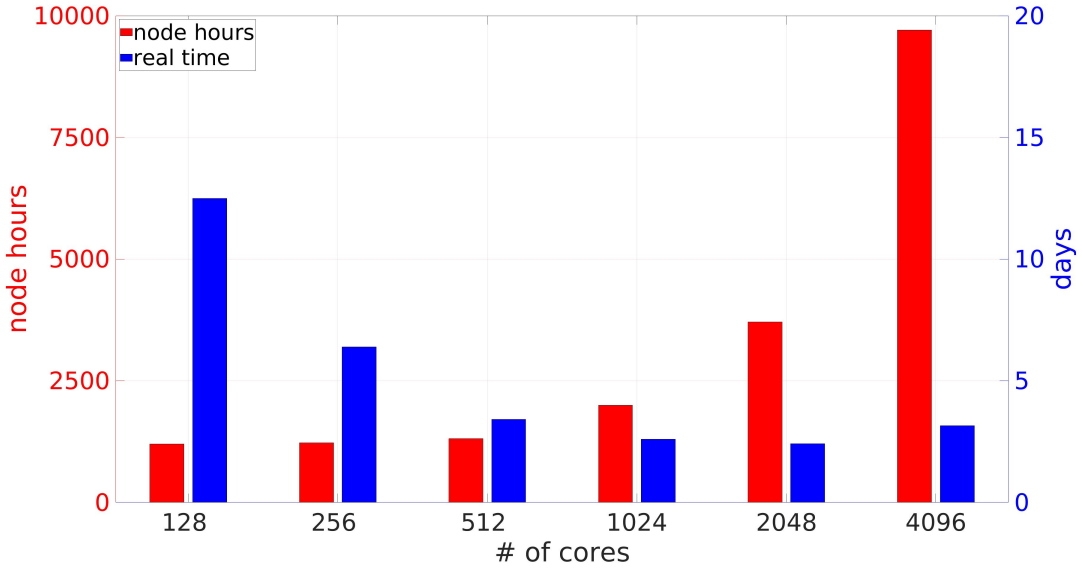

Figure 5.4: Comparison of real time hours and computing node hours for the strong scaling test. The graph indicates that even though 1024(86) and 2048(171) cores(nodes) show a higher total speed up the usage of 512(43) cores(nodes) provides the best ratio between resources (node hours) spent and time needed to solve the problem.

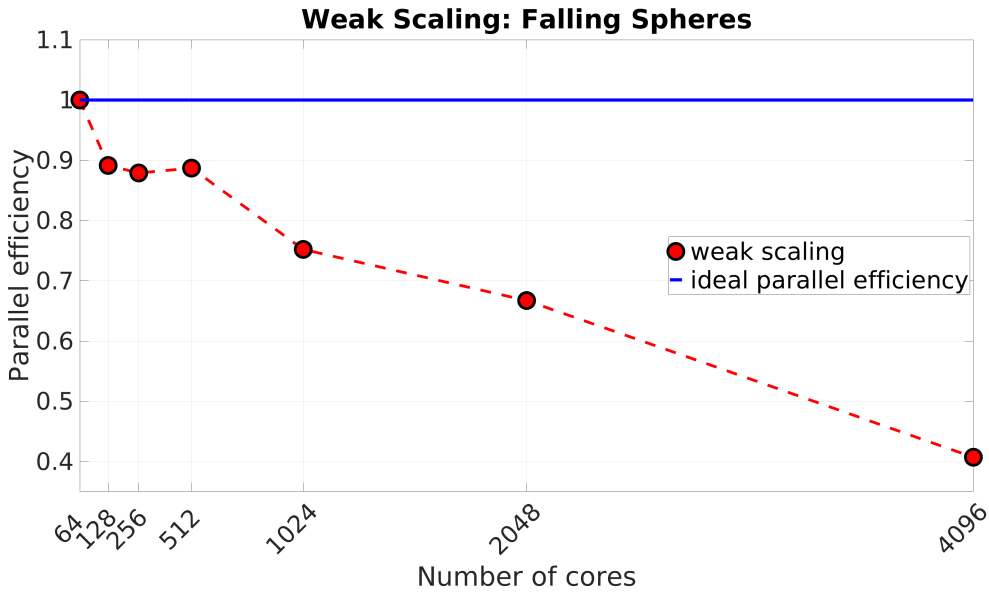

Figure 5.5: Weak scaling for a problem size of 32^3 grid points per core with 12 cores per node employing the inbuilt viscous falling spheres test of LaMEM. The configuration consists of multiple falling spheres that have a viscosity that is 1000 times larger than the surrounding matrix.

Curriculum vitae

Education

— Ph.D., University of Lausanne, 2019 (defended on November 12th, 2019).
  — *Thesis title* Three-dimensional thermo-mechanical numerical modelling of fold and thrust nappe stacking with application to the Helvetic Nappe system (W Switzerland).
  — *Committee* Prof. Dr. Frédéric Herman, Prof. Dr. Stefan M. Schmalholz
  Prof. Dr. Yury Y. Podladchikov, Prof. Dr. Jean-Luc Epard
  Prof. Dr. Philippe Yamato
— Master in geoscience and environment, Johannes-Gutenberg University Mainz, 2016.
— Bachelor in geoscience and environment, Johannes-Gutenberg University Mainz, 2014.
— Secondary school graduation, Maria von Linden Gymnasium Stammheim, 2006.

Fields of Research Interest

Geodynamics, Mechanical heterogeneities, Orogenic wedge formation, fold and thrust belts, Numerical modelling, High-Performance Computing.

Memberships and awards

— Member of the Swiss Geocomputing Centre SGC
— Member of the European Geoscience Union (EGU)

Teaching Experience

— BSc, Numerical Modelling, Unil since 2017.
— MSc, Advanced MATLAB as a language of scientific computation, Unil since 2017.
— MSc, MATLAB as a language of scientific computing, Unil since 2017.

— MSc, Quantitative Tectonics, Unil since 2017.
— Doctoral school, CUSO – Introduction to HPC in Earth sciences, Unil since 2017.

Publication list

Publications in peer-reviewed scientific journals

— Spitz R, Bauville A., Schmalholz S.M., Kaus B.J.P Control of 3D architecture on the structure of fold-and-thrust belts: numerical simulations with application to the Helvetic nappes, Solid Earth, in review November 2019.

— Spitz R, Schmalholz S.M., Kaus B.J.P and Popov A.A., Quantification and visualization of finite strain in 3D viscous numerical models of folding and overthrusting, Journal of Structural Geology, accepted 27 November 2019.

Contributions to conferences

— Spitz R., Schmalholz S. 3D numerical modeling of nappe formation applied to the Western Helvetic nappe system, 14th Emile Argand Conference 2019, Sion, Switzerland. Talk.

— Spitz R, Schmalholz S, Kaus B. 3D numerical modeling of nappe stacking applied to the Helvetic nappe system European Geosciences Union 2019, Vienna, Austria. Poster.

— Spitz R, Schmalholz S, Kaus B. 3D finite strain quantification and numerical modelling. of the transition between viscous folding and thrusting. Swiss Geoscience Meeting 2018, Bern, Switzerland. Talk.

— Spitz R, Schmalholz S, Kaus B. 3D numerical modeling of basement-cover deformation during accretionary wedge formation. European Geosciences Union 2018, Vienna, Austria. Poster.

— Spitz R, Schmalholz S, Kaus B. 3D numerical modelling and finite strain analysis of the transition between viscous overthrusting and folding Swiss Geoscience Meeting 2017, Davos, Switzerland. Poster.

— Spitz R, Schmalholz S, Kaus B. 3D numerical modeling with application to the Helvetic nappe system: Transition of viscous overthrusting to folding and oblique basal overthrusting. Swiss Geosciences Meeting 2016. Geneva, Switzerland. Poster.

— Spitz R, Schmalholz S, Kaus B. 3D numerical modeling of the lateral transition between viscous overthrusting and folding with application to the Helvetic nappe system. European Geosciences Union 2016, Vienna, Austria. Poster.

Acknowledgements

Before anything else I would like to express my thanks and deep gratitude to Stefan M. Schmalholz, my supervisor, for always being available and open to discuss scientific and non-scientific matters, for giving me vast amount of trust and freedom to work on my project independently, and for creating a work environment that rightfully resulted in the so-called 'happy group'.
In a similar vein I want to extend my thanks and praises to Yury Podladchikov for all his patience in the seminars, the great lunchtime and coffee discussions, for giving me the opportunity to experience and learn (partly) his way of thinking.
Both of them largely contributed to a most enjoyable PhD experience during my four years of study. Thank you for having as at your places for special and non-special occasions.
Moreover, I want to thank Ludovic who helped me tremendously with all numerical and computing related problems, while also inspiring me to take up road cycling. In general, he was always there to quickly help out or go for a drink or two.
Here, I want to also mention Thibault who in similar manner helped me out in the earlier days of programming. I will never forget the great times we had at your and Cindy's place, thank you two so much for hosting all of us on countless evenings with homemade pizza and whiskey.
Special thanks and gratitude also to Arthur, who gave me the opportunity to visit, work and babysit Cécile with him in Japan. Even though Japan was quite too humid for my taste, I enjoyed every minute of my stay. Thank for your hard work on the visualization for our study and introducing me to Python.
Next I also want to acknowledge Boris, my former supervisor, for recommending me for this PhD position. His boundless enthusiasm and energy to get things going and done is truly inspiring.

Following I would also like to thank my fantastic work group comprising, Dani, Lorenzo, Annelore, Josh, Evangelos, Lyudmilla, Emilie and Yoann.
Here, above all, my deepest appreciation to Dani and Lorenzo with whom I not only shared the office but also the flat for almost 4 years. It is both astounding and amazing that we managed to get along so well despite all our differences. The time with you was truly remarkable.
Special thanks also to Annelore for helping me out with everything french related and organizational problems that I encountered along my way.
Many thanks also to the people of ISTE for all good times and conversations, Yury, Vjeran, Luca, Marco, Matthia, Katja, Gino, Alexandra, Florian, Guillaume, Martin and Manu.
Furthermore I want to thank my Jury consisting of Stefan Schmalholz, Yury Podladchikov, Jean-Luc Epard and Philippe Yamato. In particular, my gratitude to Jean-Luc Epard who contributed to our second study and helped me to improve my understanding on the Helvetic nappes.
Last but not least, I want to express my gratitude to my family, especially my parents who supported me all the way through my studies and who were so understanding of my long periods of absences from home.